Colored PV modules based on Interference Filters

Simona Villa

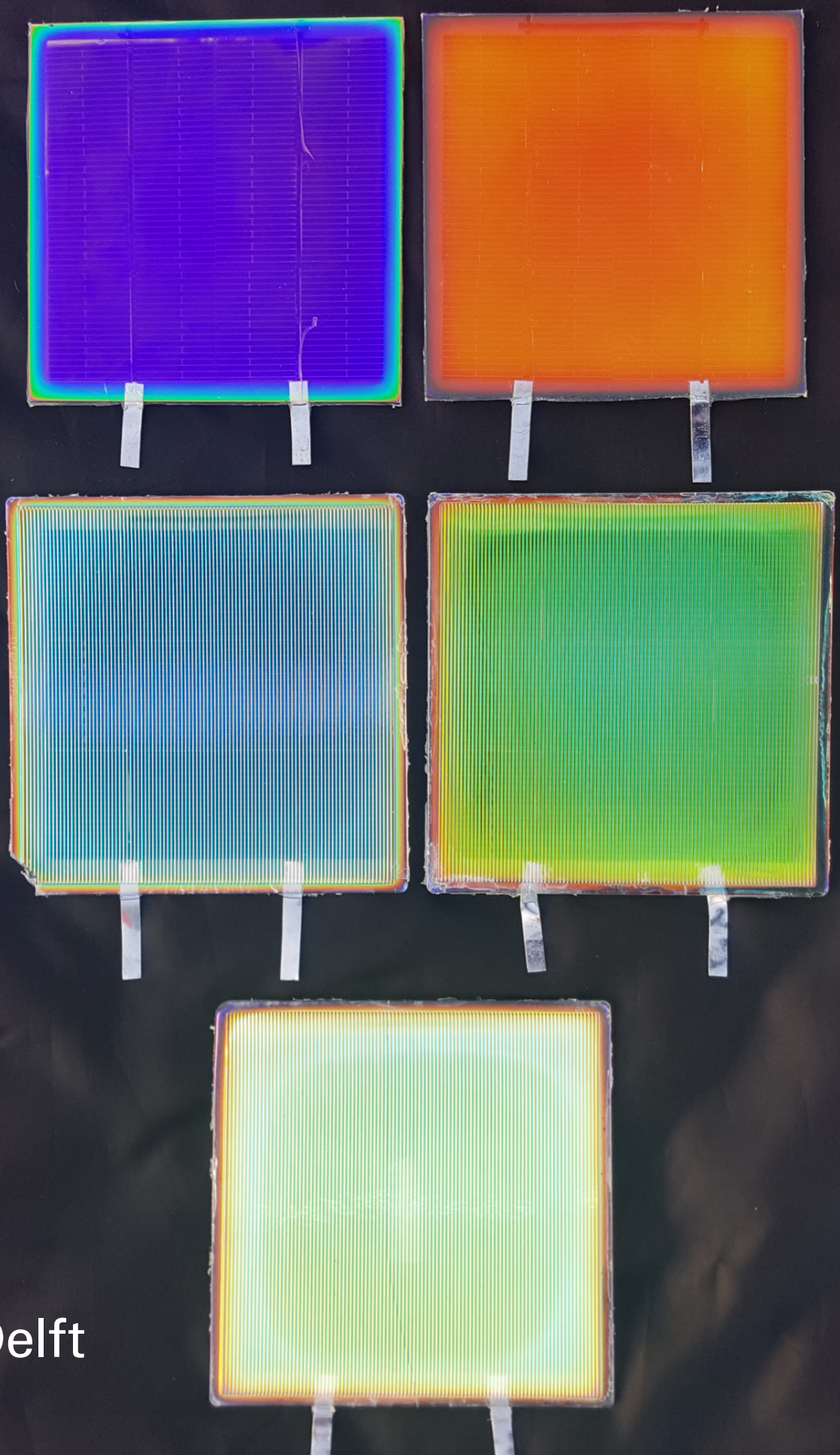

Delft University of Technology

TU Delft

Colored PV modules based on Interference Filters

by

Simona Villa

to obtain the degree of Master of Science in

Sustainable Energy Technology

at the Delft University of Technology,
to be defended publicly on Friday November 16, 2018 at 10:00 AM.

Student number:	4579550	
Project duration:	January 2018 – November 2018	
Thesis committee:	Dr. ir. O. Isabella,	TU Delft, Supervisor
	Ir. J. C. Ortiz Lizcano,	TU Delft, Daily Supervisor
	Prof. dr. ir. M. Zeman,	TU Delft, Head of the ESE Department
	Prof. dr. ir. T. Klein,	TU Delft, External committee member

This thesis is confidential and cannot be made public until Novemeber 16, 2018.

TU Delft

Abstract

Building Integrated Photovoltaics (BIPV) has the potential to play a major role in the ongoing transition towards nearly zero energy buildings. However, the BIPV market is still a niche market, representing only 1% of the global PV share. One of the main barriers that hinder the deployment of BIPV is the lack of aesthetic flexibility. Architects and designers are often reluctant to embed PV systems in buildings due to their unsuitable color.

In this thesis, the use of interference filters (IFs) as color coating solution for PV modules is proposed. IFs are optical devices designed to selectively reflect a narrow portion of the visible solar spectrum while transmitting the remaining part. The structural coloration provided by the filter is highly dependent on the angle of incidence of the light. This angular dependence could be an issue for BIPV applications, since color homogeneity is often an important requirement. The objective of this work is to model, fabricate and assess the opto-electrical performance of colored crystalline silicon (c-Si) PV modules based on interference filters, with the final goal of increasing the aesthetics of this technology.

First, the angular resilience challenge is addressed. Simulation results show that texturing the glass surface significantly improves the color stability, thanks to diffuse reflection of light. Very high angular resilience up to 80° can be achieved with a double-side texture profile made of hemispherical grooves. Secondly, five interference filters deposited on different glass substrates are used to fabricate 10 x 10 cm^2 c-Si colored mini-modules. The optical characterization of the demonstrators allows to partially validate the optical model and confirm the good angular resilience of the textured surfaces. Finally, the electrical performance of the mini-modules is evaluated. I-V measurements show that IFs only affect the short-circuit current of the mini-modules due to optical losses. Depending on the color and the topology of the surface, absolute efficiency losses range from 0,95% to 4,6%.

Contents

List of Figures

List of Tables

Preface

This thesis is the product of ten months of work in the PVMD group of TU Delft and it represents the culmination of my studies. This achievement would not have been possible without the help and support of many people.

First of all, I would like to thank my supervisor, Olindo Isabella, for giving me the possibility to work on this project and take part in many other stimulating activities. But mostly for being a motivating and enthusiastic professor. A huge thanks goes to Juan Camilo, my daily supervisor, for guiding me through this work and for doing it always with an encouraging attitude. With your knowledge, and your nice irony, you helped me in the best possible way. I am also thankful to prof. dr. ir. Miro Zeman, for giving me the chance to carry out my research in the PVMD group, and to dr. ir. Tillmann Klein, for your willingness of being part of my thesis committee.

Thanks to the rest of PhDs, post-docs and professors of the PVMD group. Particularly, thanks to Rudi and Robin for the useful technical discussions, Guangtao for the help with the filter depositions, and Gianluca for being always ready and willing to help, with a friendly smile. I am grateful also to Martijn and Stefaan that with their kindness and patience helped me with the equipment every time I needed it.

A big thanks goes then to the people with whom I shared this experience more closely. Thanks for being friends, before being colleagues. Thanks for the countless coffee breaks, the lunches and all the laughs that made the working days less hard to face. A special thanks goes to the the guys of the Basque-Italian house, thanks for all the moments spent together inside and outside the walls of the university. To Thomas, for being an amazing teammate in these two years. And to Andres, for your incredible kindness and generosity, and for the support you gave me until the end.

A special thanks goes to Silvia, Letizia and Alice, my beautiful Roman friends. Thank you girls for your true friendship, and for being always there, despite the distance.

My deepest gratitude goes to my family. *Mamma, papà, Paolo, grazie per tutto ciò che mi avete insegnato, per il vostro immenso sostegno e il supporto incondizionato che mi date. Grazie per avermi sempre incoraggiata a seguire quello in cui credo. Questo lavoro lo dedico a voi.*

E a te, Simone. Che sei stato al mio fianco dal primo momento che i nostri sguardi si sono incrociati. Voglio ringraziarti per il tuo supporto infinito durante questi mesi, ed in tutti quelli prima. E per essere la mia forza e la mia più grande fonte di ispirazione. Ma sopratutto, grazie per il tuo amore.

Simona Villa
Delft, November 2018

1 Introduction

1.1. Background

Today, the energy consumption of residential and commercial buildings covers about 40% of the global energy demand [1]. Therefore, the building sector is one of the main targets of European and global policies on mitigating climate change. In the recent years, the impressive technological developments and the increased awareness of the danger caused by climate issue drove the price of renewable energy sources down. In particular, the solar photovoltaic (PV) technology is playing a major role in the energy market and it is considered nowadays one of the fastest growing industries in the world [2].

In this context, Building Integrated Photovoltaic (BIPV) has attracted increasing attention in the last years and it is seen as a promising solution for meeting the requirements on energy performance of buildings. BIPV is intended to be a photovoltaic material that can replace conventional building elements in parts of the building envelope, such us facades or roof tiles [1]. A BIPV system, therefore, has the double functionality of providing electrical energy to the building and being physical part of its protective skin.

Despite its great potential, the BIPV market is still a niche market. The present size of its share is approximately 1% of the global PV industry [3]. The BIPV spread is limited by various technical and social barriers. Among these, the most relevant is the social acceptance of a technological non-appealing device on a building, which is intrinsically conceived also as an aesthetic object. While for a standard BAPV (building added PV) system, that can be hidden on top of a roof, the focus is primarily on cost and efficiency, for BIPV the aesthetic component becomes extremely important.

Motivation

"Acceptance of solar technology in construction by the general public can only be achieved by means of convincing visual ideas and examples"

Thomas Herzog, 2001 [4].

According to the architect Thomas Herzog, considered as a BIPV pioneer, the aesthetical appeal of the PV technology as building element plays a crucial role in its social acceptance. A survey conducted a few years ago showed that he is not the only one to think this: around 85% of architects believes that aesthetic concerns would increase PV system installations and they would prefer other colors besides black even at the expenses of lower efficiency [5]. Since architect, designers and building owners are the main decision makers in the building sector, and since they give great value to visual and aesthetic aspects, it is clear that for BIPV systems the focus should be shifted towards increasing the aesthetic options of the PV modules. In this respect, rather than a problematic challenge, photovoltaics would be seen more as an opportunity to achieve an high level of architectural

design [6].

Today, there are essentially two approaches for incorporating solar panels in the building: either make them invisible and inconspicuous, or make them a visible architectural feature that adds value to the building [7]. In either case, architects have to be provided with more choices than the traditional dark blue/black framed module. When we talk about aesthetic and visual appearance of an object, the first aspect we think of is its color. In fact, both scientific studies and empirical observations have proven that human reaction in the architectural environment is to a large extent based on the sensory perception of color [8]. In recent years, several technologies started to be investigated with the goal of providing color to PV modules. The option that will be treated in this thesis is the use of interference filters (IF) as color tuning coating applied on the frontal surface of the PV glass.

Interference filters as color tuning solution

Colored interference filters are optical devices designed to selectively reflect a narrow portion of the visible sunlight spectrum while transmitting the remaining part. They are made of pairs of thin-film dielectric materials with high (n_H) and low (n_L) refractive indices which are alternated to form a multilayer structure [9]. As the name recalls, IFs work by exploiting the *interference effect*, which takes place between the incident and reflected waves at the layers boundaries. Depending on the phase difference between the interacting waves, constructive or destructive interference is achieved. If, for a specific wavelength, the reflected waves interact constructively, reflectance will be bolstered. On the other hand, the remaining spectrum will undergo destructive interference and light will be transmitted through the filter structure. When an interference filter is applied on the top surface of a PV module, the module will be perceived with the color corresponding to the reflected wavelength. The remaining wavelengths, for which the filter is transparent, will be then transmitted to the absorber layer of the solar cell and effectively used for current production. The working principle of an interference filter made of n layers is shown in figure 1.1. By accurately designing the filter structure in terms of number and thickness of layers, a wide range of colors with variable brightness and hue can be obtained.

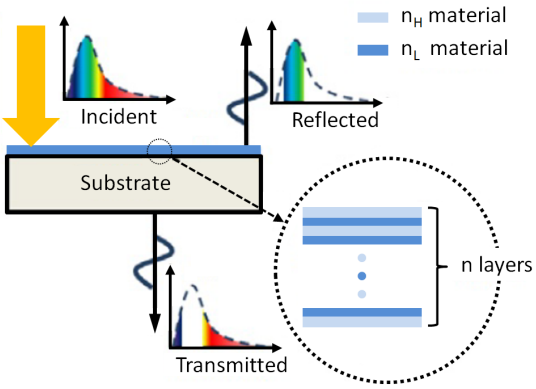

Figure 1.1: Schematic showing the working principle of a thin-film interference filter made of n layers of interspersed high (n_H) and low (n_L) refractive indices materials. Adapted from [10].

The intrinsic nature of this optical technology makes it extremely flexible, but at the same time introduces a limitation: the angular dependence. The condition for destructive and constructive interference depends upon the optical path difference of the reflected waves. When light comes from oblique angles, the optical path, i.e. the distance the light has to travel within the layer, will change. This means that constructive interference between the reflected waves will not take place anymore at the design wavelength but at a different one, thus the perceived color will change.

1.2. Aim and outline of the work

Interference filters can provide PV modules with aesthetic flexibility at the price of low performance impact, but their color angular dependence could be an issue for the development of this technology in the BIPV sector. Usually, BIPV systems are designed to cover quite large oblique or vertical areas of roofs or facades, and color homogeneity is often an important requirement for architects. The angular resilience challenge will be addressed in this work, as well as the fabrication and characterization of several crystalline silicon (c-si) colored mini-module demonstrators.

The goal of this master thesis can be summarized by the following statement:

To model, fabricate and assess the opto-electrical performance of colored c-si PV modules based on interference filters with the final goal of increasing the aesthetics of this technology.

This objective will be achieved by answering to the following research questions, that will also define the structure of this document.

1. How can the angular resilience of interference filters be improved?
2. Is it possible to fabricate colored mini-modules based on interference filters? If so, does the optical behaviour of the colored demonstrators validate the optical model?
3. What is the electrical performance of colored mini-modules made with interference filters?

The outline of this thesis is as follow. In chapter 2, the state-of-the-art of the colored PV technology will be presented. Alternative color tuning solutions carried out by PV companies and researchers will be described, with the goal of providing a wider picture of the context in which this work is set. Some examples of realized BIPV projects in which colored PV modules have been used will also be presented. Chapter 3 will provide fundamental theoretical knowledge on the optics that governs the interference filters theory. How an IF can be used as color tuning coating will be explained, as well as its working principle and basic design rules. Chapter 4 contains the angular resilience study, aiming to answer to the first research question. First, the optical model will be presented and some basic notions on human color perception will be provided. Then, the main simulation results will be described and analyzed. Chapter 5 will deal with the second research question. The fabricated colored mini-modules will be shown and the steps needed to manufacture them will be explained. The chapter will end with their optical performance characterization, meant to validate the model. In chapter 6, the electrical performance of the built mini-modules will be analyzed, thus answering to the last research question. The chapter will end with the analysis of cell-to-module losses related to the in-house PV module fabrication process. To conclude, chapter 7 will briefly summarize the main findings of the work and collect recommendations for future work.

2

State-of-the-art of colored PV technology

In the past few years, several different technologies to make colored PV modules started to be explored. These techniques can be categorized in two main approaches: give color on a cell level and on a module level. The two approaches will be discussed in this chapter and some of the current state-of-the-art methods currently used by companies or investigated by research institutes will be here presented. Additionally, some recently realized BIPV projects in which colored PV modules have been used will be mentioned. The chapter will end with conclusions containing a comparison between the different technologies and final remarks.

2.1. Color on cell level

With this approach, the coloration process is performed directly on the solar cells, while a normal transparent glass will be used to cover the colored solar cells. In this way, the PV module will not have a uniform color and it will be possible to distinguish the different cells as well as their interconnections. Some of the possible ways to tune the color of solar cells are described below.

2.1.1. Anti-reflective coating (ARC) modulation

In commercial multicrystalline silicon solar cells, the front surface is usually covered by a single layer of hydrogenated silicon nitrate SiN_x:H, which is meant for both passivation and antireflection purposes [11].

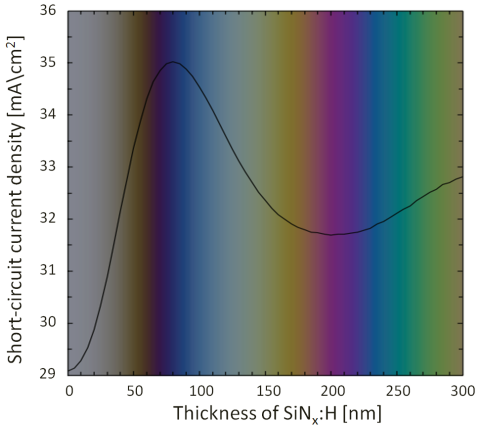

Figure 2.1: Perceived color and short circuit current density for different ARC (SiN_x:H) thicknesses on a textured solar cell. Adapted from [11].

If the refractive index (n) and the thickness (d) of the ARC are optimized for minimum reflection under AM1.5 spectrum, i.e. when their values are respectively around n=2 and d=80 nm, the cell assumes the typical dark blue color [12]. The simplest approach to modify the color of solar cells is by changing the thickness of the ARC, as shown in figure 2.1. The figure also displays the short circuit current density (J_{sc}) trend, showing that when the ARC thickness is changed to obtained different colors, the reduction of J_{sc} is significant. Examples of fabricated colored solar cells are visible in figure 2.2.

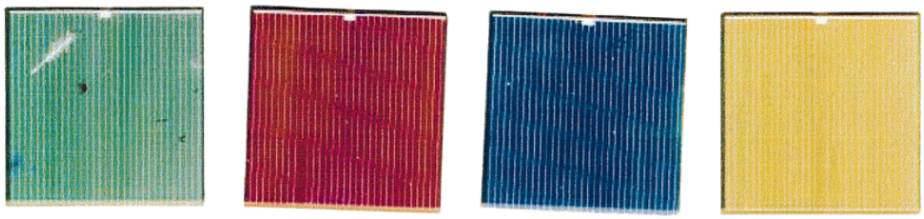

Figure 2.2: Colored solar cells with ARC thicknesses of 204 (green), 148 (red), 191 (dark blue) and 102 (yellow) nm. Adapted from [13].

Another approach, meant to limit the J_{sc} losses, is to deposit an additional layer of dielectric material, such as SiO_2, on top of the standard SiN_x:H in order to create a double layer ARC. Li et al. [11] showed that simply by varying the thickness of the top layer, while maintaining the SiN_x:H at the optimal thickness of around 80 nm, it is possible to obtain a wide range of colors and avoid extremely high optical losses.

2.1.2. Metallic nano-particles coating

An alternative way to modify the color of solar cells is by exploiting plasmonic effects. Plasmonic effects, such as colors, can be realized by sub-wavelength metallic structures which are embedded or surrounded in a dielectric material [14]. At the interface between metal and dielectric, free electron oscillations can be generated, which are called surface plasmons. At the resonance wavelength, determined by the types of materials, size, shape and arrangement of the structures, scattering and/or absorption is increased. It must be noticed that the increased absorption causes unwanted optical losses, but, on the other hand, the increased scattering, which take place also at off-resonance wavelengths, can improve the light trapping within the cell [14].

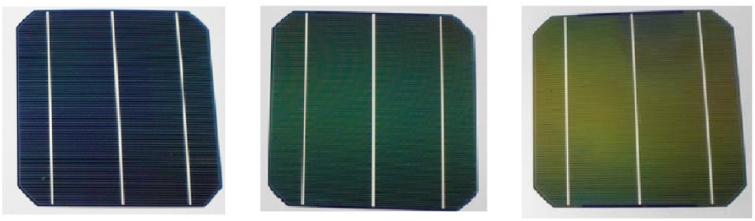

Figure 2.3: Monoscrystalline c-Si solar cells coated with different types (sizes and shapes) of Ag nano-particles. Adapted from [14].

Peharz et al. [14] used this approach and tuned the color of c-Si solar cells by applying a layer of metallic nanoparticles on top of the cells [14]. Figure 2.3 shows monocrystalline Si solar cells coated with different types of Ag nanoparticles deposited by sputtering and consequently thermally annealed. The amount of sputtered Ag, determined by the sputtering time, is the reason of the different colors. As visible, with this approach it is possible to tune the color from blue to green and brownish. Additionally, the position of the reflection peak was found to be almost independent

from the angle of incidence [14].

2.2. Color on module level

Giving coloration on a module level implies leaving the solar cell manufacturing process unaltered. In this case, standard solar cells, with their typical blue-black color, will be used and the coloration process will be performed on the encapsulating glass or on an extra intermediate layer. This approach allows to have a more homogeneous visual impression of the PV module, given that the colored glass will hide, to a certain extent, the solar cells placed underneath. Some of the possible ways to tune the color of PV modules are described below.

2.2.1. Printed dots of ceramic ink

A widely used approach to color the module glass is by using colored inks. For example, the Dutch company Kamaleon Solar deposits ceramic inks on the external side of the glass and hardens them in hexagonal patterns, creating the illusion of a homogeneous image [15]. With this technology, almost every color can be obtained, as well as any design, pattern or logo.

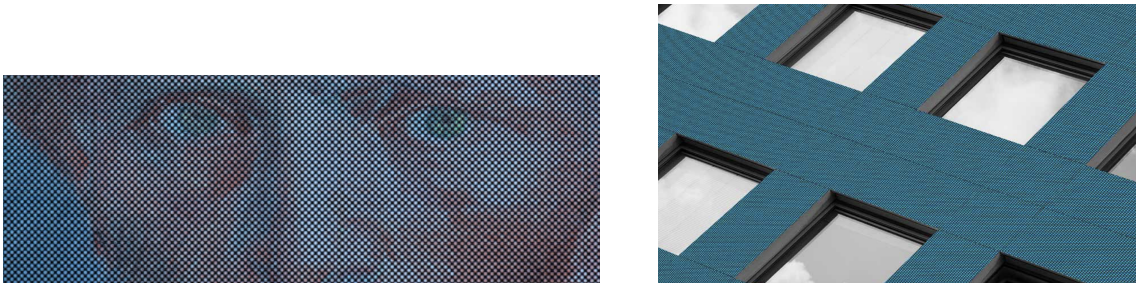

(a) **(b)**

Figure 2.4: Examples of PV modules using printed dots of ceramic ink.**(a)** Customized PV module with printed image of Van Gogh painting. **(b)** Blue PV modules covering a building façades. Adapted from [15].

In order to create an optical illusion, the background has to be homogeneous; this can be achieved for example using black rear-glass and hiding the silver interconnections [15]. Then, the desired color or image is printed on the glass. However, printing a whole image on the entire surface of the glass would block the light to reach the solar cells. This can be avoided by printing only part of the image and creating dots of a certain shape and pattern; in this way, the light can pass though the gaps and the printed dots, acting as pixels, create the illusion of a homogeneous image. As final step, usually the colors are digitally enhanced to contrast the darkening effect caused by the black background [15]. Examples of customized and colored PV modules produced with this technology are shown in figure 2.4.

2.2.2. 3D photonic structure on glass (*Morpho* butterfly effect)

The Fraunhofer Institute for Solar Energy Systems (ISE) realized colored PV modules by exploiting the *Morpho* butterfly effect, a bionic concept based on 3D photonic structures. They reproduced the microscopic structure of the *Morpho* butterfly's wings, consisting of vertical ridges with horizontal lamellae attached to them [16]. As shown in figure 2.5a, the lamellae are almost equidistant, while the vertical ridges are places with a defined disorder. In this 3D structure, three effects take place: multilayer interference, diffraction and scattering. The interference effect is caused by the alternation between lamellae and air gaps and it is the cause of the reflectance peak; diffraction is due to the periodic ridge arrays, leading to angular spread, while scattering is present due to the irregularity of the height of the structure, and it leads to a more uniform color over different viewing

angles [16] [17].

This type of structure is extremely challenging to produce, especially at industrial scale. At the Fraunhofer ISE research centre, this functional layer has been implemented at the rear side of the external glass, hence between the glass and the laminate (e.g. EVA) [16]. Different colored PV modules have been produced, as the ones shown in figure 2.5b, with a good angular color stability up until 50°.

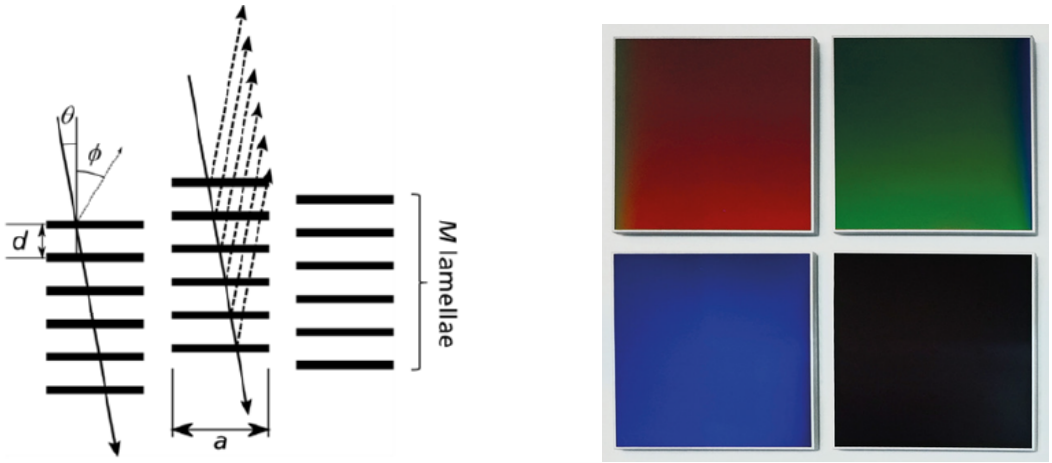

(a) **(b)**

Figure 2.5: (a) Morpho effect basic principle: interference from Bragg stack, diffraction from ridges and disorder due to lamellae height variation. **(b)** Photographs of colored PV modules coated with *morpho* glass: red, green, blue and uncoated module (bottom right). Adapted from [16].

2.2.3. Intermediate color foil

This approach implies the use of an additional foil with the desired color appearance to be laminated inside the module. The evident advantage of this technique lays in the logistics: the foil can be easily made of the most suitable size and shape without any challenge, and the production lines of both the solar cells and the encapsulating glass do not need to be altered [1]. This also means lower costs and more flexibility. However, these advantages are compensated by a significant drawback: adding an extra layer of material on top of the absorbing layer will decrease the amount of light absorbed by the active layer, hence substantially decreasing the overall performance.

2.3. Realized colored BIPV projects

Copenhagen International School

The Copenhagen International School's building (Copenhagen, Denmark) is one of the biggest building integrated solar power plants in the world. The building is covered by approximately 12,000 solar panels, covering an area of 6,048 m^2 with an installed capacity of 720 kWp [18]. The solar panels are characterized by a blue-green color given by the Kromatix™ solar glass, developed by the Swiss company Swissinso in partnership with the EPFL (Swiss Polytechnic Institute). The color of the glass is due to a nanoscale multilayered coating deposited on the inner surface, while a satinated treatment is applied on the outer surface of the glass [18]. Due to this coloring technology, with varying angle of observation the modules appear slightly different. The architect decided to take advantage of this effect and, by mounting the panels with a tilted angle of around 4° in different orientations, he managed to animate the building, giving the idea of an undulating movement and allowing a suggestive integration between the building and the surrounding ocean [19].

(a) **(b)**

Figure 2.6: (a) Copenhagen International School building. **(b)** Detail of the façades with blue Kromatix modules. Adapted from [18].

Coal silo factory of Basel

Another colored BIPV project that has been realized using the Kromatix™ solar glass of Swissinso is the redevelopment of the former coal silo in Basel, Switzerland. The building, shown in figure 2.7, has been modernized in a sustainable multipurpose edifice. PV modules with four different colors, grey, blue, gold and blue-green, have been used to cover the north- and south-facing façades as well as the roof area. They cover a total area of 159 m^2 and generate around 16,400 kWh annually, approximately 40% of the building's energy needs [18].

Figure 2.7: Coal silo building in Basil. Façades and roof covered by PV modules encapsulated with colored Kromatix™ glass. Adapted from [18].

London Kingsgate House

The Kingsgate House (London, UK) BIPV project, realized in 2014, is an example of colored BIPV system that follows the approach of coloring the solar cells while using transparent glass. Double glass PV modules made of colored polycrystalline solar cells run vertically down the front of the building and are used as louvers to provide shading and prevent overheating during summertime. Gold and green solar cells were used to blend in with the surrounding streetscape; the colors match with the tree-lined environment and the modules are designed to look like a living wall [20]. The

electricity load met by the solar system is approximately 20% of the total demand, with an estimated power generation of 13,145 kWh/year [20]. Thanks to the color and the sparkling effect due to the polycristalline cells, this modern apartment building, shown in figure 2.8, is considered a stunning piece of architecture. This project is the the proof that PV modules do not have to be necessarily camouflaged, but they can actively contribute to increase the aesthetic of a building, rather that impoverish it.

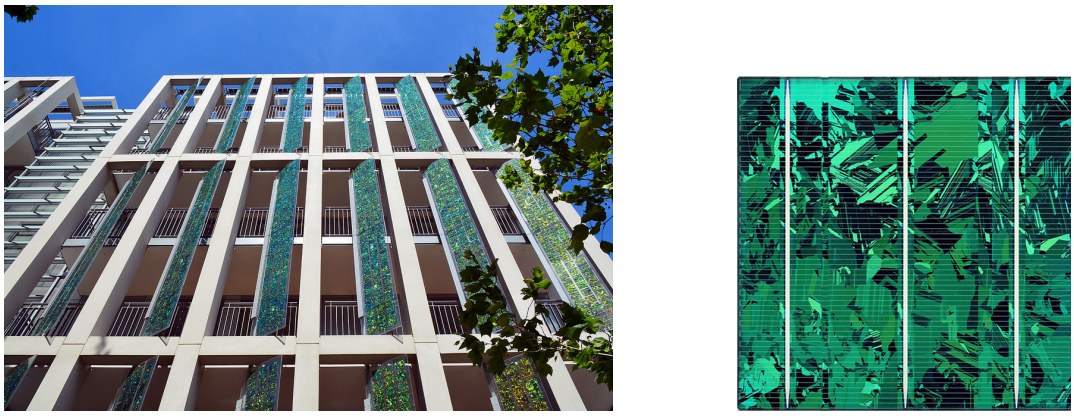

(a) **(b)**

Figure 2.8: (a) Kingsgate House (London, UK): green-gold solar cells laminated into glass louvers on the frontal façade of the building. **(b)** Detail of green solar cell (Marble series) produced by the solar company Lof. Adapted from [21].

Energy Building for Union Eiendomsutvikling

The energy building for Union Eiendomsutvikling, located in Oslo (Norway) and realized in 2015, is the first BIPV project in the world that makes use of screen printed technology on the external side of the PV glass [22]. According to the wishes of the architects, green PV modules as shown in figure 2.9 have been used to cover the façades of the building.

PV glasses with different shapes were used in order to allow the best possible rendering of a green wall while minimizing the yield lost due to the green image printed on the front glass [22]. The R&D department of the Belgian company ISSOL, which realized the project, reached a final yield of 83% in comparison with non-printed PV glasses, with a total installed capacity of 127,5 kWp [22].

(a) **(b)**

Figure 2.9: (a) Union Eiendomsutvikling Energy Building (Oslo, Norway). **(b)** Detail of the screen printed colored layer on the PV glass. Adapted from [22].

2.4. Limitations of existing approaches

It has been shown that several different technologies can be used to tune the color of PV modules according to architects and designers' requirements. Coloring the solar cells allows to use normal transparent glass and to avoid the lamination of extra layers that create additional reflectance. However, this approach has several disadvantages. For instance, the colors that can be obtained simply by varying the ARC thickness are limited and they often lead to high current losses. In general, the main problem with this approach is the difficult logistics due to the fact that the production line of the PV cells has to be modified. Solar cells producers are not used and might be reluctant to product diversification; moreover, producing small quantities of a specific product at an acceptable price is not easily achievable [1].

The additional cost is also strongly related to an increase in the complexity of the manufacturing process. As shown, the main technologies used to make colored solar cells exploit optical effect, such as nanoscattering or plasmonic effects. Being wavelength-dependent, these mechanisms also imply an additional challenge: the angular resilience of the color. When looking at the cells from different angles their color might change: this aspect can be used as an additional value in some architectural projects, but for most of urban designers, it is considered as a drawback. When coloring the cells, the non-uniformity of the color is not only due to the scarce angular stability, but it is also attributed to the metallic interconnections and the spaces between the cells, that in this case will remain visible.

Some of these problems can be overcame if the second approach is used: coloring the external glass while using standard solar cells. In this way, the manufacturing process of PV cells will remain unaltered and only the encapsulating glass will be modified, allowing a much greater flexibility. When colored glass is used, the solar module will appear homogeneous and in some cases it will not be possible, especially at a certain distance, to distinguish the cells and the metallic elements. This is particularly desirable when the goal of the architect is to camouflage the solar panels with the passive building elements.

Among the most used methods to color the solar glass there are, respectively, the use of printed dyes or the deposition of nano- and micro-structures on the glass surface. Printing inks and applying ceramic pastes are certainly easier and cheaper techniques, but they have the disadvantages of color fading and very high losses due to the reduction of light that can reach the solar cells. On the other hand, when photonic structures or thin-film layers are deposited on the glass surface, the glass is said to have a structural coloration rather than a pigment-based coloration, meaning that it is the interaction with the light itself to cause the color. As for the cell-level case, also colored glass that exploits reflection of sunlight and other optical principles is often characterized by a poor color angular consistency. Angular resilience and performance of the module can be partially increased at the expense of complexity and higher costs.

Alternatively, it has been shown that a cheaper approach consists in laminating a colored polymer foil underneath the glass. In this way, the logistic issues are considerably reduced, but a substantial decrease in performance due to the additional layer will take place.

It can be concluded that, without exception, all PV coloring techniques have the disadvantage of reducing the efficiency and the power production of the solar modules; therefore, a compromise must be found between electrical performance and aesthetical quality.

The alternative color tuning solution discussed in this thesis is the use of interference filters (IFs), optical devices that, thanks to selective reflection of light, will give the modules a structural coloration. This technology can be applied on both cell and module level, but because of its higher flexibility here we will focus on the second approach. In the next chapters it will be shown how can IFs can partially overcome some of the problems discussed above, offering the possibility to obtain bright structural colors or mat colors with high angular stability.

3

Interference filters

To understand the working principle and the performance of optical filters, it is important to recall some quantities, definitions and concepts of the optical physics that describes these devices. Throughout the chapter, the fundamentals of thin-film coatings theory will be described, starting from single-layer interference and extending the digression on multilayer stacks. It will be explained how interference filters can be used as color tuning coatings, which is their working principle and the main design rules. Finally, the filter design chosen for this thesis work will be presented.

3.1. Fundamentals

3.1.1. Basic theory of thin-film coatings

The theory of thin-film optical coatings is rather vast and complex. An extensive treatise of this topic is out of the scope of this thesis, therefore only the most relevant concepts, useful for the understanding of the working principle of interference filters, will be presented here. The following theoretical information is mainly based on the comprehensive textbook *thin-film Optical Filters*, authored by *Macleod* [9] and considered as a one of the major references in the field.

The first step in the study of the optical physics is the resolution of Maxwell's equations. Electricity and magnetism are proven to be the two sides of the same coin. In optics, light is treated as an electromagnetic wave, therefore electromagnetic theory is used to describe its behaviour [23]. To analyze how light propagates through a medium, the *refractive index* must be introduced. This dimensionless quantity is defined as the ratio between the speed of light in vacuum, c, and the speed of light in a specified medium, v:

$$N = \frac{c}{v} = n - ik. \tag{3.1}$$

From equation 3.1, it can be seen that the refractive index N is a complex number and it is composed by a real part n, indicating the phase velocity, and an imaginary part k, called extinction coefficient. k indicates the attenuation of the wave when it propagates in the material and it is related to the absorption coefficient through the following expression:

$$\alpha = 4\pi k/\lambda. \tag{3.2}$$

Equation 3.2 shows that α and consequently the refractive index N are wavelength-dependent quantities. This dependency is called *dispersion* and it is the phenomenon that causes rainbows and prisms to spatially separate the incoming white light into components of different wavelengths, perceived as different colors. Figure 3.1 shows how shorter wavelengths, i.e. violet-blue, undergo a larger deviation than longer wavelengths, i.e. red, where the refractive index is smaller.

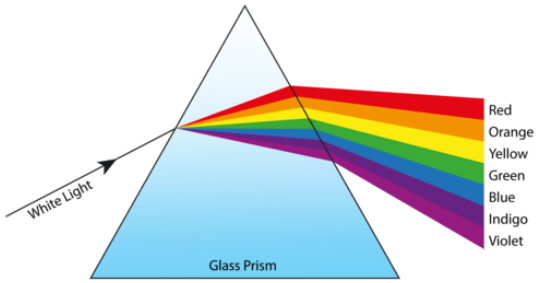

Figure 3.1: Dispersion of white light beam into different wavelengths when passing through a prism. Adapted from [24].

Another important quantity in the optical theory is the *characteristic optical admittance*, a property that describes how easy or hard it is for light to pass through a specific material. It is given by the ratio of the magnetic and electric field amplitudes, respectively H and E:

$$y = \frac{H}{E}. \tag{3.3}$$

Usually y is a complex number, but in free space it becomes real and assumes the value of

$$y_{free} = \sqrt{\frac{\epsilon_0}{\mu_0}} = \frac{1}{377} \quad [S] \tag{3.4}$$

where ϵ_0 and μ_0 are respectively the permittivity and the permeability of vacuum.

The optical admittance of a generic medium y and its complex refractive index N are directly proportional according to:

$$y = y_{free} \times N. \tag{3.5}$$

At this point, we can consider the interface between two non-absorptive media, where the incident medium is characterized by suffix 0 and the exit one by suffix 1. As shown in figure 3.2, the incident ray is split into a reflected ray and a transmitted (or refracted) ray.

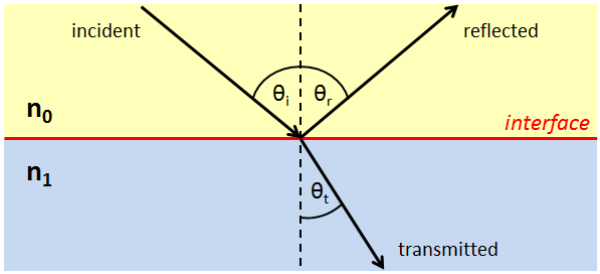

Figure 3.2: Incident ray of light partially reflected and partially transmitted at the interface of two media.

In the most generic case, the incident light beam will reach the surface with an angle θ_i. As a consequence of Fermat's principle, stating that the light follows the path of least time, it can be proven that the reflected ray will leave the interface with an angle θ_r equal to θ_i [25]:

$$\theta_r = \theta_i. \tag{3.6}$$

On the other hand, the transmitted ray will propagate through medium 1 with an angle θ_t which is different to θ_i. This is due to the different refractive indices of the materials. As already mentioned,

when light passes from a medium to another one its propagating speed changes. The higher the refractive index, the slower the light traverses the medium, the more the light will bend towards the normal surface (lower θ_t). The relationship between the angle of incidence and the angle of refraction is given by Snell's law:

$$n_0 \sin\theta_i = n_1 \sin\theta_t \tag{3.7}$$

In equation 3.7, n should be replaced by the complex refractive index N for the case of absorptive media.

Now, let us consider the case of light reaching an interface between two materials at normal incidence (θ_i=0). Part of the light will be reflected and part transmitted. The amplitude ratio of the reflected electric field to the incident electric field is called *amplitude reflection coefficient* ρ, while the ratio of the amplitude of transmitted to incident electic fields is called *amplitude transmission coefficient* τ. They are expressed, respectively, by

$$\rho = \frac{y_0 - y_1}{y_0 + y_1} \tag{3.8}$$

and

$$\tau = \frac{2y_0}{y_0 - y_1}, \tag{3.9}$$

where y_0 and y_1 are the optical admittances of the incident and exit medium, respectively.

Considering an absorption-free incident medium (e.g. real N_0 and y_0), *reflectance* R and *transmittance* T can be defined as follow:

$$R = \rho\rho^* = \left(\frac{y_0 - y_1}{y_0 + y_1}\right)\left(\frac{y_0 - y_1}{y_0 + y_1}\right)^* \tag{3.10}$$

and

$$T = \frac{4y_0 Re(y_1)}{(y_0 + y_1)(y_0 + y_1)^*}, \tag{3.11}$$

where * represents the complex conjugate and Re indicates the real part of the complex number.

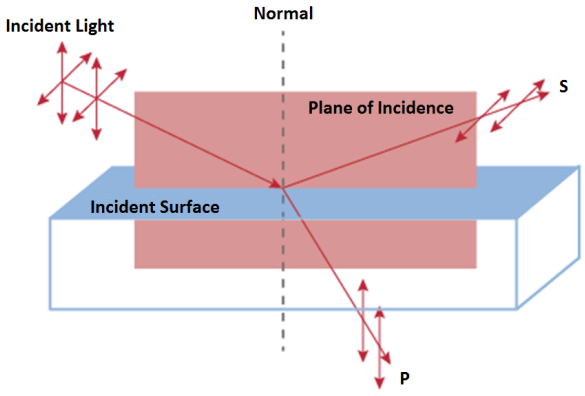

Figure 3.3: s and p polarization of light. Adapted from [26].

For oblique angles of incidence we consider two polarized components of the incident wave: one with the electric vector in the plane of incidence, known as p-polarized, and one with electric vector normal to the plane of incidence, known as s-polarized, as shown in figure 3.3 The orientation of the corresponding magnetic vectors follow the rule of the right-handed set, being H and E perpendicular and both normal to the propagating direction. The propagation of these two wave components can be treated independently.

We can define the *tilted optical admittances* η for the p- and s-polarized waves respectively as:

$$\eta_p = \frac{Ny_{free}}{\cos\theta} \qquad \text{(p polarization)} \tag{3.12}$$

and

$$\eta_s = Ny_{free}\cos\theta \qquad \text{(s polarization)}. \tag{3.13}$$

For any polarization, using the optical admittances from equations 3.12 and 3.13, the reflectance at a single interface is given by

$$R = \left(\frac{\eta_0 - \eta_1}{\eta_0 + \eta_1}\right)\left(\frac{\eta_0 - \eta_1}{\eta_0 + \eta_1}\right)^* \tag{3.14}$$

and the transmittance by

$$T = \frac{4\eta_0 Re(\eta_1)}{(\eta_0 + \eta_1)(\eta_0 + \eta_1)^*}. \tag{3.15}$$

Note that direct sunlight can be considered unpolarized, i.e. containing equal amounts of p- and s-polarized rays [27]. Therefore, from now on we will not distinguish anymore between different polarizations.

3.1.2. Interference on single-layer coating

Let us now consider the addition of a layer in-between the incident medium and the substrate. If the thickness of this layer is smaller than the coherence length of the incident light, i.e. if it ranges from fractions of nanometers up to micrometers, the layer is said to be a *thin-film*. As already mentioned, at the interface between two media part of the light will be transmitted and part reflected (neglecting absorption). That part of light that is transmitted and reaches the bottom surface of the thin-film, may once again be transmitted or reflected, as shown in figure 3.4.

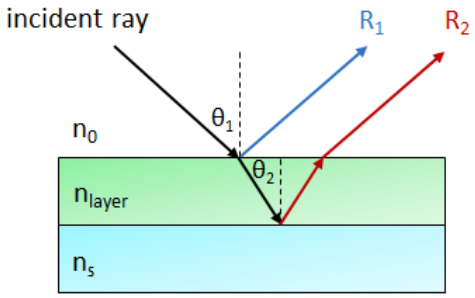

Figure 3.4: Light reflection from upper and bottom interfaces of a thin-film layer.

The physical phenomenon in which the light waves that are reflected by the upper and lower boundaries of a thin-film interfere with each other is known as *thin-film interference*. For each specific wavelength, two waves can interfere either constructively or destructively. In the first case, the reflected light is enhanced, while in the second case it is reduced.

Constructive interference is achieved when the crest of a wave meets the crest of another wave of the same frequency at the same point; the waves are completely in phase and the amplitude of the resulting wave is the sum of the individual amplitudes. On the other hand, *destructive interference* occurs when the crest of a wave meets the trough of another one; the two waves are completely out of phase (shifted of 180°) and the amplitude of the resulting wave is equal to the difference of the individual amplitudes. Figure 3.5 shows a schematics of these two interacting conditions. In the most generic case of an interaction between two arbitrarily shifted waves, both constructive and destructive interference are involved, resulting in a mixed wave.

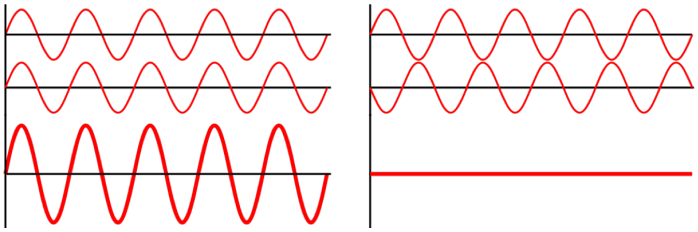

Figure 3.5: Constructive (left) and destructive (right) waves interference.

Additionally, phase change can take place also according to the refractive indices of the media at the two sides of the interface. When light travels from a medium with lower refractive index to another one with a higher refractive index ($n_1 < n_2$), the phase of the reflected wave will experience a shift of 180°. Conversely, when a light wave goes from a higher to a lower refractive index medium ($n_1 > n_2$), there will be no phase shift in the reflected wave.

In the schematic shown in figure 3.6 we are assuming a thin-film layer of thickness d with a refractive index n_l, such that $n_0 < n_l < n_s$. When an incident light wave hits the layer interface in point A, the reflected wave will suffer a phase shift of 180°. At the same way, when the transmitted wave reaches the bottom interface in point B another phase shift of 180° will take place for the reflected wave. However, when the light arrives in point C no phase shift occurs, since the wave is travelling from a medium with higher to one with lower refractive index.

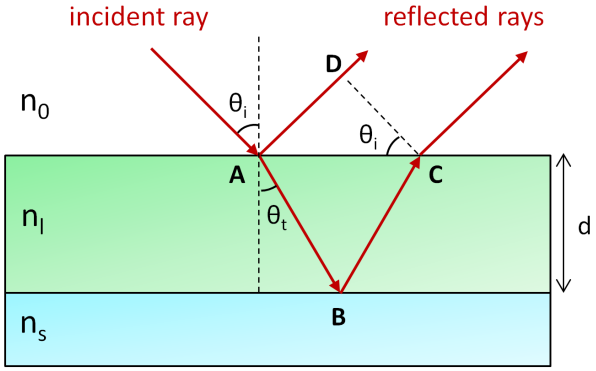

Figure 3.6: Optical path difference for light reflected from upper (A) and lower (B) interfaces of a single layer thin-film coating.

To determine the condition for interference between the two reflected waves, the optical path difference (OPD) must be calculated. In thin-film optics, generally one is more interested in optical distances and thicknesses rather than geometrical ones. Thus, the optical path (OP) of a wave in a medium is defined as the product of the actual geometrical distance d and the refractive index n of the material:

$$OP = n \times d \tag{3.16}$$

meaning that a wave that travels a path of given geometrical length arrives with the same phase shift as if it had traveled a path of that optical path length in a vacuum.

Referring to the schematics in figure 3.6, it is possible to express the optical path difference OPD between the two reflected rays as:

$$OPD = n_l(\overline{AB} + \overline{BC}) - n_0\overline{AD}, \tag{3.17}$$

where

$$\overline{AB} = \overline{BC} = \frac{d}{\cos(\theta_t)} \tag{3.18}$$

and

$$\overline{AD} = 2d\tan(\theta_t)\sin(\theta_i). \tag{3.19}$$

Using Snell's law, $n_0 \sin\theta_i = n_1 \sin\theta_t$, equation 3.17 can be rewritten as:

$$OPD = 2d n_l \cos(\theta_t). \tag{3.20}$$

The interference between the two rays will be constructive only if the optical path difference is equal to an integer m of the light wavelength λ. Equation 3.21 shows the conditions for interference for both the constructive and destructive cases

$$OPD = 2d n_l \cos(\theta_t) = \begin{cases} m\lambda & \text{for constructive interference,} \\ (m-\frac{1}{2})\lambda & \text{for destructive interference.} \end{cases} \tag{3.21}$$

From equation 3.21 it can be noticed that the degree of constructive and destructive interference depends on the difference in the phase of the waves, which is in turn dependent on the thickness of the layer, the angle of incidence of the incoming light and the refractive indices of the media surrounding the interface.

It can be noticed that, when $m = 1$ and $\theta_i = 0$ (normal incidence), the thickness required to suppress reflection and maximize transmission is equal to:

$$d = \frac{\lambda}{4n_l}. \tag{3.22}$$

In this case, the reflected rays undergo destructive interference, while the transmitted ones experience constructive interference. A coating layer designed in this way is said to have *Quarter Wavelength Optical Thickness* (QWOT). It must be noticed, however, that this relation is strongly dependent on the wavelength of light, meaning that the desired minimum/maximum reflection condition will be guaranteed only for the designed wavelength; for all other wavelengths the coating is said to be suboptimal.

3.1.3. Interference on multilayer coating

Let us now consider a multilayer configuration of several thin-film layers deposited on a substrate, as shown in the simplified diagram of figure 3.7.

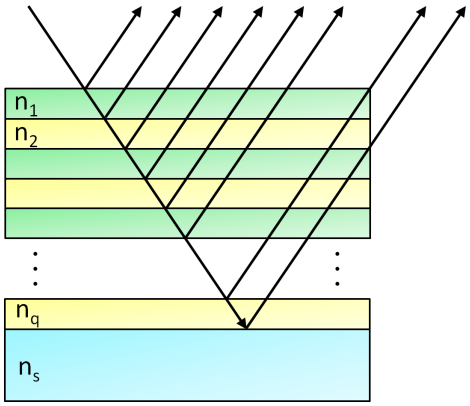

Figure 3.7: Multilayer thin-film stack. Refraction has been omitted for simplicity.

In order to describe the interference effect over an assembly of multiple thin-film layers and determine the total reflectance and transmittance, we have to come back to the concept of optical admittance. Indeed, the stack of multiple layers can be seen as a single surface having an admittance Y equal to:

$$Y = \frac{C}{B}, \tag{3.23}$$

where C and B are, respectively, the total tangential magnetic and electric field. These two parameters constitute the so-called *characteristic matrix of a thin-film assembly*, expressed by:

$$\begin{bmatrix} B \\ C \end{bmatrix} = \left\{ \prod_{r=1}^{q} \begin{bmatrix} \cos\delta_r & (i\sin\delta_r)/\eta_r) \\ i\eta_r \sin\delta_r & \cos\delta_r \end{bmatrix} \right\} \begin{bmatrix} 1 \\ \eta_s \end{bmatrix} \tag{3.24}$$

where η_s is the substrate admittance and δ is the phase shift experienced by the wave as it travels a distance d normal to the boundary within the layer, given by:

$$\delta = \frac{2\pi N d \cos(\theta_i)}{\lambda}. \tag{3.25}$$

The characteristic matrix of the whole assembly is nothing but the multiplication of the matrices associated with each individual layer, M_1, M_2 and so on, as expressed by the following equation:

$$\begin{bmatrix} B \\ C \end{bmatrix} = [M_1][M_2]...[M_q] \begin{bmatrix} 1 \\ \eta_s \end{bmatrix} \tag{3.26}$$

The characteristic matrix of a multilayer stack is extremely complex to solve, hence a computer is needed to carry out the extensive calculations involved. Once solved, reflectance and transmittance of the multilayer structure are given by:

$$R = \left(\frac{\eta_0 B - C}{\eta_0 B + C}\right)\left(\frac{\eta_0 B - C}{\eta_0 B + C}\right)^* \tag{3.27}$$

and

$$T = \frac{4\eta_0 Re(\eta_s)}{(\eta_0 B + C)(\eta_0 B + C)^*}. \tag{3.28}$$

3.2. Interference filter as color tuning coating

An interference filter is an optical device that is able to selectively reflect or transmit specific wavelength bands by exploiting the interference effect [9]. Depending on their reflection and transmission patters, interference filters can be classified in: longpass, shortpass, bandpass and bandblock filters. The first two are able to effectively block the transmission of short and long wavelengths respectively, while bandpass and blockpass filters present only fixed wavelength ranges where either transmission or reflection is allowed [28]. Figure 3.8 shows the transmission curves for each of the aforementioned filter.

Since the purpose of this work is to produce color coatings for solar modules, we will focus on bandpass filters, aiming to produce ideally a narrow-band reflection peak in the visible part of the spectrum, while transmitting all other wavelengths to the absorber layer of the solar cells. To accomplish this, some requirements and designing rules must be followed.

The interference filter of our interest is made of alternating layers of two different dielectric materials having high (n_H) and low (n_L) refractive indices, as depicted in figure 3.9. These layer are periodically interspersed, with period $p = d_H + d_L$, where d_H and d_L are the thicknesses of high and low refractive indices media, respectively.

When light hits the filter and propagates through it, constructive and destructive interferences arise. If the thicknesses of the two materials are chosen in such a way that, for a specific wavelength

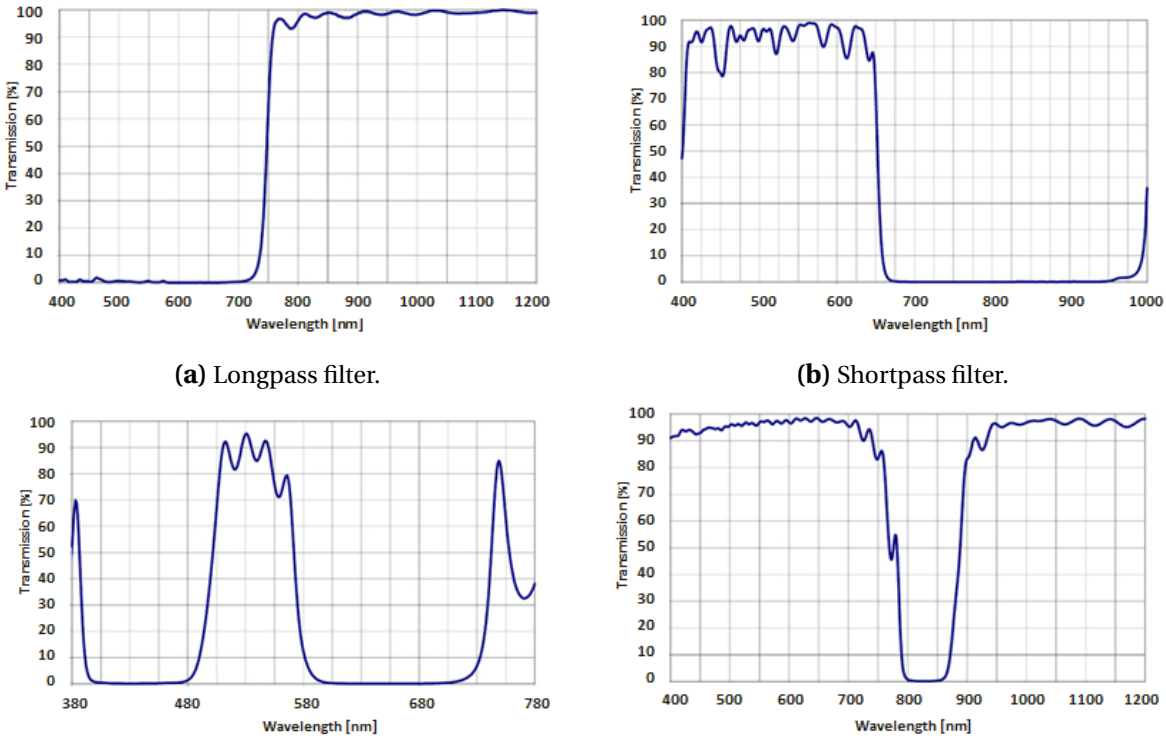

(a) Longpass filter.

(b) Shortpass filter.

(c) Bandpass filter.

(d) Bandblock filter.

Figure 3.8: Transmission curves for different types of interference filters. Adapted from [28]

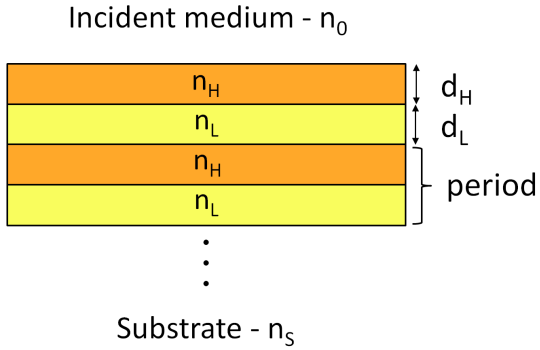

Figure 3.9: Interference filter structure: alternating layers of materials with high (n_H) and low (n_L) refractive indices.

λ_0, the reflected beams are of equal phase when they reach the front surface, then constructive interference will take place and reflectance will be bolstered.

The structure in figure 3.9 can be referred to using the following notation: *air* - $(HL)^p$ - *glass*, where incident medium and substrate are in this case air and glass, respectively. It must be noticed that, in literature, this notation is used when H and L denote the thickness of a quarter-wave layer of high and low refractive index materials, respectively. Such device is also called Distributed Bragg Reflector (DBR). In a DBR, for a given number of layers, the reflectance is maximized when the outermost layer at both sides is H [9]. In this case, the admittance of the stack is given by:

$$Y = \left(\frac{n_H}{n_L}\right)^{2p} \frac{n_H^2}{n_s}. \tag{3.29}$$

The reflectance is then:

$$R = \left(\frac{1 - \left(\frac{n_H}{n_L}\right)^{2p} \frac{n_H^2}{n_s}}{1 + \left(\frac{n_H}{n_L}\right)^{2p} \frac{n_H^2}{n_s}} \right)^2 \tag{3.30}$$

where $(2p+1)$ is the total number of layers.

To increase the reflectance at the design wavelength there are mainly two approaches that can be chosen:

- increase the number of periods p;
- choose the two materials such that the mismatch between their refractive indices ($\Delta_{HL} = n_H - n_L$) is as high as possible.

The first approach is proven by equation 3.30 and is clearly visible in figure 3.10a. From the graph it can be seen that increasing the number of pairs from 3 to 10, the reflectance at the designed wavelength is boosted from around 40% to more than 90%. Figure 3.10b, on the other hand, is related to the second approach: the higher the mismatch Δ_{HL}, the smaller is the number of periods needed to get the maximum reflectance [29].

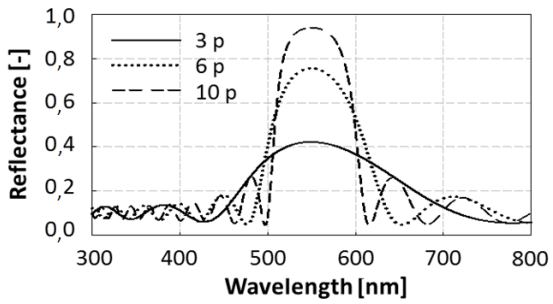

(a) Reflectance curves as function of wavelength for increasing number of periods.

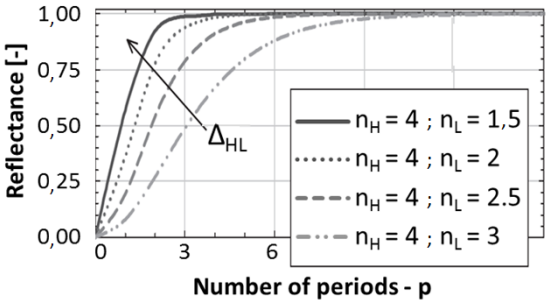

(b) Reflectance curves as a function of number of periods for different n_H/n_L couples.

Figure 3.10: Effect of increasing number of periods (left) and different index mismatches on the reflectance curve of the filter. Adapted from [29].

It must be noticed that the effect of a high mismatch between the refractive indices of the materials is an increase in the width of reflectance, not in the height of the reflection peak. The width of reflectance is shown in figure 3.11 and it is defined by $2\Delta_g$, where Δ_g is expressed by [9]:

$$\Delta_g = \frac{2}{\pi} \sin^{-1}\left(\frac{n_H - n_L}{n_H + n_L}\right). \tag{3.31}$$

When the purpose is, as in our case, to obtain bright colors, the high reflectance zone should as high and narrow as possible. Therefore, in order to have optimal reflectance, a balance should be found between these two designing rules.

Figure 3.11 points out also another important factor to take into account when designing or choosing a filter: the presence of ripples, i.e. the oscillatory smaller reflectance peaks before and after the high peak corresponding to λ_0. These peaks are present because the constructive interference effect for reflection takes place at any wavelength for which the layers are an odd number of quarter wavelengths thick [9]. The ripples, indeed, corresponds to wavelengths equal to $\lambda_0/3$, $\lambda_0/5$, $\lambda_0/7$ and so on, and they increase as the number of periods increases. On the contrary, at wavelengths where the layers have optical thickness equal to an even number of quarter-waves, the

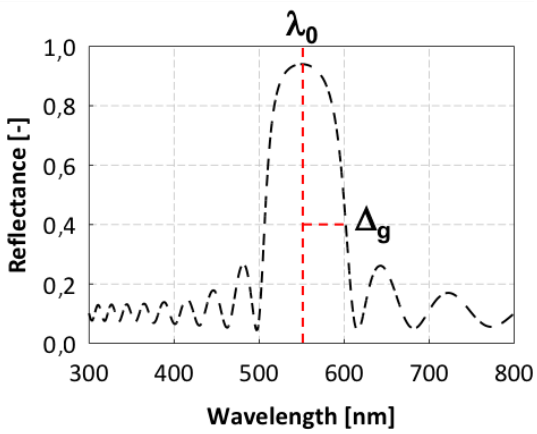

Figure 3.11: Width of high reflectance, $2\Delta_g$, and design wavelength, λ_0.

layers will not cause any effect (they will act as absentee layers) and the reflectance will be the same as the substrate [9].

The design of the optimal interference filter as color coating for PV modules has already been conducted within the PVMD group of TU Delft University by Juan Camilo Ortiz Lizcano [30]; therefore, in this thesis, the same filter design will be used to perform both optical simulations aimed at improving the angular resilience and the fabrication of the filter for the validation.

The optical filter that will be used is made of alternating layers of silicon dioxide (SiO_2), as low refractive index material, and silicon nitride (SiN_x), as high refractive index material. The number of periods was usually set to 10 (i.e. 20 layers) in order to obtain values of reflectance above 80%; however, due to fabrication issues, also an option with 6 pairs was explored. Figure 3.12 shows the structure of the filter deposited on a glass substrate.

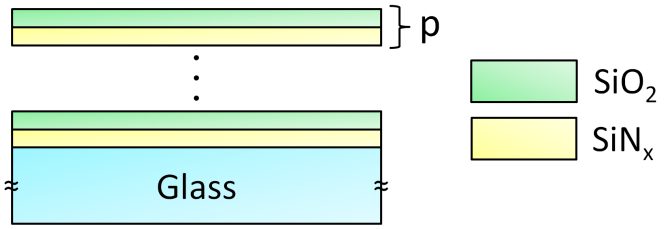

Figure 3.12: Designed filter: alternating SiN_x and SiO_2 layers deposited on glass. The number of periods p is in the range of 6 to 10 in order to assure high reflectance.

These two materials have been chosen because of several reasons. First of all, both silicon dioxide and silicon nitride are dielectric materials that can have an energy bandgap lower than 300 nm, hence they should not cause unwanted parasitic absorption or electrical loss; they have adequate optical properties in the visible spectrum, allowing good color purity and brightness [30]. Furthermore, their availability makes them suitable also for industrial scale applications. Another important and more practical reason behind the choice of these two materials is the fact that they can be deposited with relative ease and velocity through PECVD (Plasma Enhanced Chemical Vapour Deposition) using one single machine in the EKL and Kavli laboratories at TU Delft university.

The n and k values of the two materials are reported in figure 3.13. In the visible part of the spectrum, the refractive index of SiO_2 ranges from 2,21 to 1,97, while for SiN_x it varies from 1,50 to 1,43. Additionally, from the graph it must be noted that the silicon nitride is slightly absorptive in the short wavelengths up until 350 nm. As stated before, silicon nitride with phase Si_3N_4 should

be ideally non-absorptive through all the spectrum (k=0); however, depending on the degrees of nitridation/Si oxidation state, other phases can be obtained. It has been reported that the optical properties of a silicon nitride layer deposited by PECVD depend on the gas flow ratio between the two precursor gases [NH_3]/[SiH_4]: the lower this ratio, the higher the refractive index and the extinction coefficient [31]. The facts that k is higher than 0 for $\lambda < 350$ nm and that the refractive index obtained is rather high show that the silicon nitride produced in our laboratories (which we will express with the general notation SiN_x) is not a stoichiometric non-absorptive Si_3N_4. Nonetheless, as it will be discussed in the following chapters, this will not be a relevant cause of performance decrease in terms of power output when the filter will be applied on a solar module.

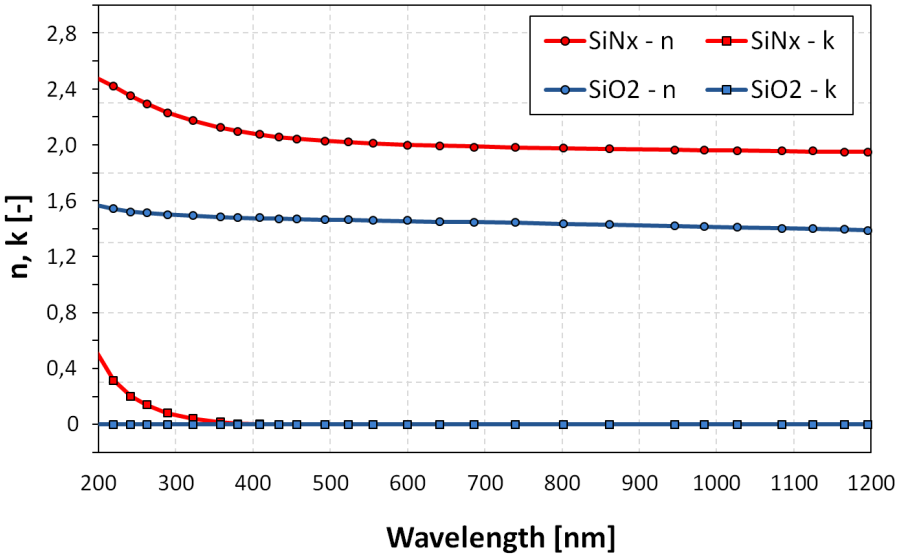

Figure 3.13: n and k values of SiN_x and SiO_2 used for both optical model and filters fabrication.

With respect to the sequence of the layers of our designed filter, it can be noticed from figure 3.12 that the first layer to be deposited (the one in contact with the glass) is SiN_x. The reason for this choice lies in the fact that when the filter will be deposited on the encapsulating glass it would be advisable to flipped it of 180°, having the filter in the inner part of the glass, in order to avoid its exposure to environmental hazards and premature ruin. In this way, light will reach the layers in the sequence: *air-glass-SiN_x-SiO_2-cell*. Since silicon dioxide, which is now the last layer, has a refractive index very close to that of the glass, the reflectance pattern of the whole module stack will not be altered once the filer is installed on top of the cell. However, it has been proven that there is no noticeable difference on the reflectance curve for the case of an optic filter placed below the glass (*air-glass-OF*) or above it (*air-OF-glass*), so color-wise the position of the filter does not affect the result [30].

Since the interference effect depends on path length difference of the reflected waves, to obtain different colors it is sufficient to change the thicknesses of the layers. In view of this, interference filters can be seen as flexible and versatile devices able to bring colors to the encapsulating glass of solar modules or on the solar cells themselves, thus expanding the aesthetic options of the PV technology.

However, it must be recalled that the design of a filter is conducted for a defined angle of incidence of the illuminating rays (typically normal incidence) and that an important feature of interference filters is indeed their angular dependence. The shift of the high reflectance peak with varying angle of incidence, which causes a shift in the perceived color, will be the focus of the following chapter.

4

Angular resilience

One of the most peculiar properties of interference filters is their angular dependence. When the angle of incidence of the light beams hitting a filter is increased there will be a shift in the reflectance peak; in particular, for a flat filter, we can talk about *blue-shift*, since the peak moves towards lower wavelengths. This happens because, as explained in chapter 3, the interference effect which causes the reflectance peak is dependent on the optical path of the light passing through the various layers of the filter. When the incident angle is varied, also the optical path changes, meaning that constructive interference will not take place anymore at the designed wavelength, but at a different one. As a consequence, the color changes considerably already from around 20-30°.

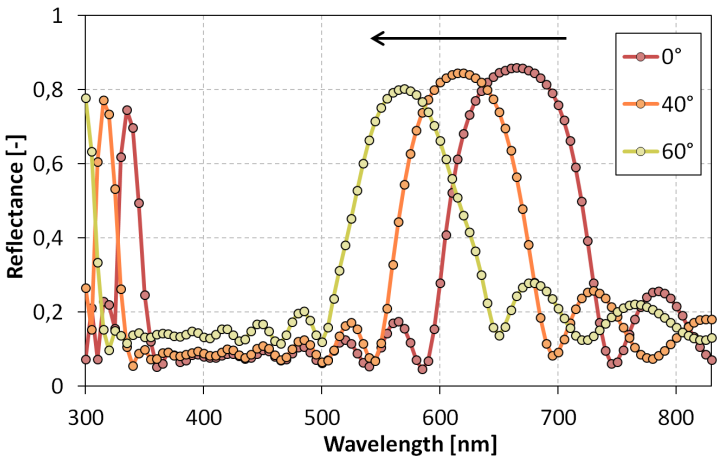

Figure 4.1: Effect of increasing the angle of incidence on a flat optical filter.

As shown in figure 4.1, at 0°, i.e. when the beams arrive perpendicularly with respect to the filter surface, the high peak of reflection is around 670 nm and we will see a red color. However, when the angle of incidence is changed to 40° or 60°, the reflection shifts towards lower wavelength values of 610 nm and 570 nm respectively, and the perceived colors will be an orange and a yellow.
In most cases, for architects involved in BIPV projects, color uniformity is an important requirement. Therefore, the first research question of this work arises:

How can the angular resilience of interference filters be improved?

This chapter aims at answering to this question. In the first section, the optical model will be presented, describing the simulation and characterization tools used. Basic notions on human color

perception will be provided as well for a better understanding of the model. In section 4.2, the main simulation results will be presented, showing how the angular resilience problem can be seen as an optimization study of the glass surface. Finally, the most angular resilient configurations will be presented and analyzed.

4.1. Optical model

The approach that was adopted to simulate the color of an optical filter consists of two main steps: (1) to apply ray-tracing to determine the reflectance spectrum, and (2) to apply a mathematical model of color perception to convert the reflectance pattern in a visible color displayed on a monitor. How these two steps have been implemented will be treated in detailed in the following sections.

4.1.1. Reflectance spectrum: GenPro4

The reflectance patterns of the optical filters have been determined by using the in-house software GenPro4, developed and validated by R. Santbergen [32]. GenPro4 is a simulation software that combines wave and ray-optics in a computationally efficient way. It is able to reproduce multilayer structures and calculate the fraction of incident light absorbed at each layer A_i and the overall transmission T and reflection R, taking into account scattering and trapping of light at the interfaces [32].

The optical model that constitutes the core of the software is based on the extended net-radiation method. Considering optically flat interfaces, reflectances and transmittances can be calculated from the Fresnel and Lambert-Beer law equations, respectively [32]. As shown in figure 4.2(a), a single ray can be reflected multiple times, and each of these reflections must be considered to obtain reliable results. The net-radiation method allows to do so by assuming that at each interface four fluxes q_i^x are defined, as illustrated in figure 4.2(b). In the notation, i is the interface number and the superscript x gives information on whether the light is approaching/leaving the interface from the top/bottom. This flux represents the total intensity due to all possible photon paths and is expressed in W/m^2. All fluxes are related by a set of linear equations; by using numerical methods the equations can be solved and it will be possible to determine R, T and A_i [32].

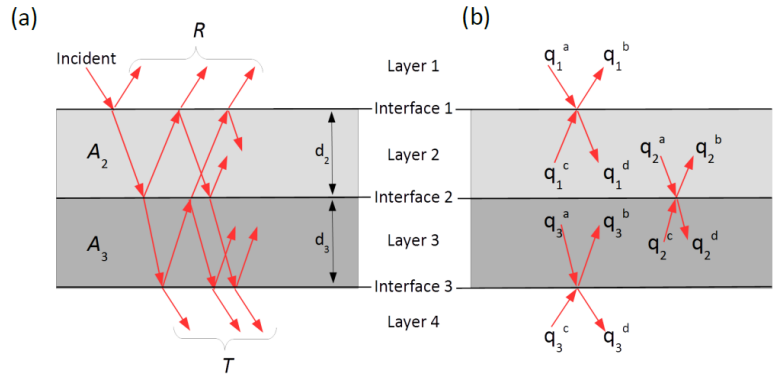

Figure 4.2: Schematic of a multilayer structure showing the numbering convention for layers and interfaces. **(a)** Various optical paths contributing to R, T and A_i. **(b)** Net-radiation fluxes. Adapted from [32].

It must be noticed that this approach provides reliable results only for incoherent layers, i.e. layers that are *thicker* compared to the length of sunlight ($\approx 1\mu m$), for which interference does not play a role. In our case, however, the layers constituting the optical filters have thicknesses comparable to the length of sunlight (coherent layers), hence giving rise to interference effects that must be taken into account. For these layers, GenPro4 uses a different calculation algorithm in which the fluxes represent the complex amplitudes of electromagnetic waves [32].

The method is further refined when considering textured interfaces. In this case, the reflected and transmitted light will not have a defined propagating direction, but they will be scattered and distributed over a range of angles [32]. Therefore, the resolution method is extended by diving the hemisphere in a defined number of angular intervals, each one with its own corresponding sub-flux, as shown in figure 4.3 [33].

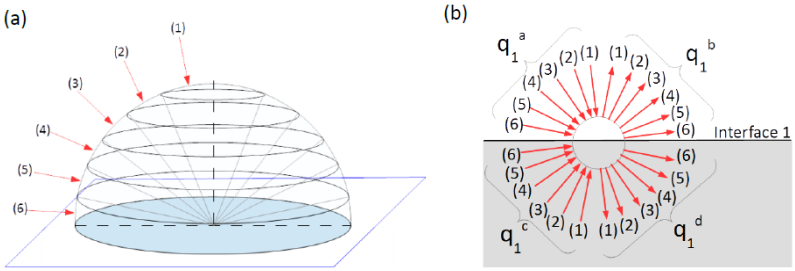

Figure 4.3: (a) Division of every hemispherical direction into angular intervals. **(b)** Net-radiation sub-fluxes at interface 1. Adapted from [32].

The relations between all the sub-fluxes will form again a large set of linear equations. Utilizing a vector notation for the fluxes allows to use matrix multiplication and to express the set of equations in a compact manner. In this way it is possible to express the angular intensity distribution of the scattered light in form of *scatter matrices* [32]. The software calculates the scatter matrices from the morphology of the interfaces, using different models depending on the feature size. The calculated matrices will be then used to obtain the fluxes. The total reflectance R of the multilayer stack will be given by the sum of the intensity of all elements of the vector q_1^b (see figure 4.3(b)), which contains the fluxes leaving the top of the outermost interface [33]. The resulting R, T and A_i are wavelength-dependent, therefore the calculation must be repeated for every wavelength in the relevant range (for the purpose of this work, the visible part of the spectrum: 300-800 nm).

Apart from defining the desired wavelength range, GenPro4 needs the user to specify: the thickness and the optical properties (n and k values) of each layer and the morphology of the interfaces surface in the form of a height matrix. Note that the software is programmed and requires Matlab to run.

4.1.2. From Reflectance to Color

After computing the reflectance spectrum in the relevant wavelength range, the following step is to transform this optical information into color coordinates, then translated into an actual visible color displayed on a screen. To fully understand the mathematical model used, first some basic notions on the human perception of colors will be provided.

Fundamentals on human color perception

The human color vision is a very complex process, which still needs to be fully understood. The first steps of this process are the stimulation of light receptors in our eyes, conversion of the light stimuli into electrical signals, and transmission of these signals containing the visual information to the brain [34]. The human eye has two different types of cells able to detect and respond to light: rods and cones. These photoreceptors react differently depending on the illuminating conditions. Rods are active in dark conditions or when light is very dim; their light sensibility is very high, with a peak at around 500 nm, they allow to distinguish shapes and relative brightness of objects, but not their colors [34]. As the illumination increases, the rods become less responsive and the cones take over. Cones are responsible for our day-vision and allow us to perceive colors. Three different types of cone cells are present in the retina of our eyes, each one with its own spectral sensitivity peak: S (short λ), M (medium λ) and L (long λ) cones. As can be seen in figure 4.4, S, M and L cones

have significant response to blue, green and red light, respectively. Because of this color perception mechanism, the human vision is said to be *trichromatic* and allows us to distinguish between 10 million different colors [34].

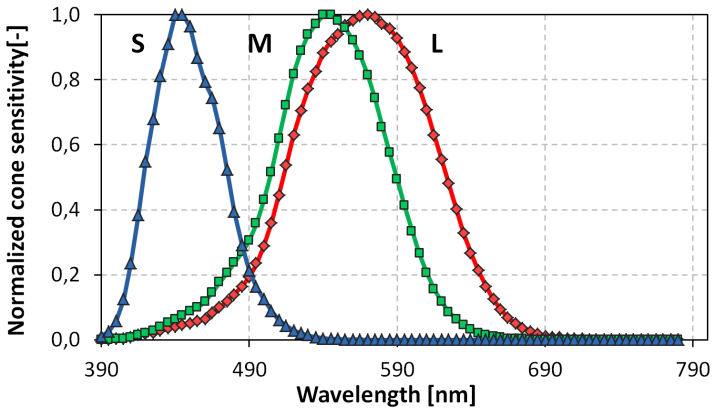

Figure 4.4: Normalized sensitivity response of human eye S, M, and L cones to monochromatic light. Adapted from [35].

In 1931, the International Commission on Illumination (*Commission internationale de l'éclairage* or CIE) started to define the standards in the field of light, lighting and color vision, developing a mathematical color model. It was found that, due to the spectral sensitivity of the human eye, not all wavelengths of light are equally effective at stimulating the human vision. The luminous efficacy of a light source is the product of how well it can convert energy to electromagnetic radiation, and how well the emitted radiation is perceived by the human eye [36]. This parameter can be normalized to the maximum possible luminous efficacy, which falls at around 555 nm (green) for a monochromatic light, thus obtaining a dimensionless quantity called *luminous efficiency*. It was also discovered that the human vision depends on the field of view of the observer, i.e. on the portion of the world that can be seen at a given moment. To elide this variable, the CIE defined a color-mapping function called the *standard observer*. The chromatic response of the standard observer can be numerically described by three *color matching functions*: $\overline{x}(\lambda)$, $\overline{y}(\lambda)$ and $\overline{z}(\lambda)$, which can be seen as the amount of the three primary colors needed to match any other color. Figure 4.5 shows these functions normalized with respect to $\overline{y}(\lambda)$, because it represents the human perception of luminosity (note the peak at 555 nm).

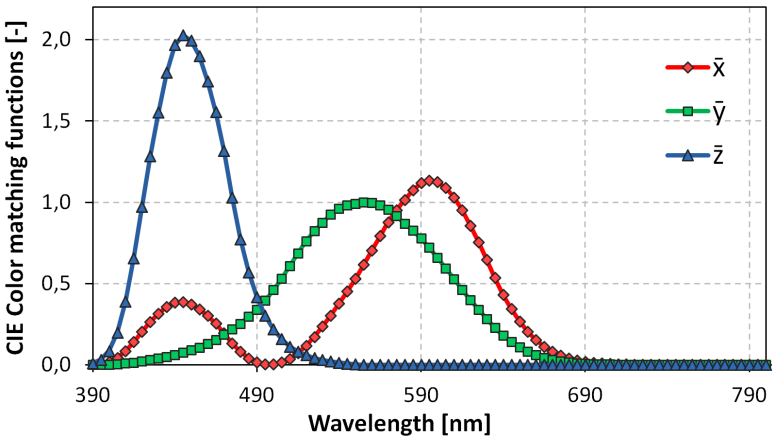

Figure 4.5: CIE Standard Observer color matching functions. Adapted from [35].

From these curves, we can now convert the spectrum into three numerical values X, Y and Z, by

integrating over the visible spectrum (380 - 780 nm) the product of the color matching functions with the spectral power distribution of the illuminant $S(\lambda)$, according to the following expressions:

$$X = \frac{1}{N}\int_{380}^{780} \overline{x}(\lambda) \times S(\lambda) d\lambda, \tag{4.1}$$

$$Y = \frac{1}{N}\int_{380}^{780} \overline{y}(\lambda) \times S(\lambda) d\lambda, \tag{4.2}$$

$$Z = \frac{1}{N}\int_{380}^{780} \overline{z}(\lambda) \times S(\lambda) d\lambda, \tag{4.3}$$

where

$$N = \int_{380}^{780} \overline{y}(\lambda) \times S(\lambda) d\lambda. \tag{4.4}$$

X, Y and Z are called *tri-stimulus values* and they form the so-called CIE XYZ color space, a three-dimensional space in which any color can be represented.

The definition of color involves two main concepts: *luminance*, which can be seen as the brightness of a color, and *chromaticity*, which is the specification of the quality of a color (properties that allows to distinguish between different colors). The XYZ color space is purposely designed in such a way that Y indicates the luminance (or brightness) of the color, Z represents the blue stimulation (S cone response) and X is a mix of the other cone response curves chosen to be non-negative [37]. We can see from the equations above that the values are normalized with respect to the source brightness, contained in the parameter N; in this way, Y will be equal to 1 for an illuminant object. By doing so, it is now possible to convert the 3D space in a 2D color space where the luminance is now fixed and the chromaticity can be defined by re-adjusting the values as follows:

$$x = \frac{X}{X+Y+Z}, \tag{4.5}$$

$$y = \frac{Y}{X+Y+Z}, \tag{4.6}$$

$$z = \frac{Z}{X+Y+Z} = 1-(x+y). \tag{4.7}$$

The derived color space, known as CIE xyY, is then specified by two of the three normalized values (i.e. x and y) and the brightness Y. In this system, the visible chromatic values form a horseshoe shaped region in a 2D plane, where the spectrally pure colors lie on the boundaries and all human perceivable colors lie within them. This graph is called CIE chromaticity diagram. It must be noticed that this diagram is obtained for a given brightness, therefore, by changing it a new set of chromaticity values will be produced. The CIE xyY color space will be then different for each illuminant. In this respect, the CIE decided to standardize the illuminating conditions (e.g. daylight, sunlight, fluerescent light, etc.) and create its own illuminants: theoretical light sources with a defined spectral power distributions.

In colorimetric studies, choosing the right illuminant is important since, for a given illuminant, its white point is uniquely defined. In an additive color model, as the CIE XYZ one, each color is given by the combination of the three primary colors and the neutral light is obtained by adding equal amounts of these three primaries. The only illuminant that can provide equal values of X, Y and Z is that with a flat spectral power distribution $S(\lambda)$, yielding to $X = Y = Z = 1$ and therefore to: $(x, y) = (1/3, 1/3)$.

The theoretical model described so far is based on illuminant sources. However, solar cells, optical filters and the majority of the objects that surround us are non-illuminant sources. The

color perception of a non-illuminant object depends on two factors: how it is illuminated and how it reflects light. In mathematical terms, this is simply translated in adding the reflectance pattern $R(\lambda)$ of the object in equations 4.1, 4.2 and 4.3:

$$X = \frac{1}{N}\int_{380}^{780} \overline{x}(\lambda) \times R(\lambda) \times S(\lambda) d\lambda, \tag{4.8}$$

$$Y = \frac{1}{N}\int_{380}^{780} \overline{y}(\lambda) \times R(\lambda) \times S(\lambda) d\lambda, \tag{4.9}$$

$$Z = \frac{1}{N}\int_{380}^{780} \overline{z}(\lambda) \times R(\lambda) \times S(\lambda) d\lambda, \tag{4.10}$$

The CIE XYZ color space and its modification in CIE xyY are only two of the main existing color spaces used. Other ones have been created in order to fit best different requirements and applications. For example, nowadays, the Internet and almost every electronic device, such as computer screens, cameras and mobile phones, all use the sRGB color space as default working space [38]. This standardization, proposed by HP and Microsoft in 1996, was meant to eliminate the time and effort lost in transformation algorithms when passing from a screen or device to another embedded with a different color space [39]. However, the color rendering of the sRGB color space is much more limited with respect to the XYZ one. Figure 4.6 shows the CIE xyY chromaticity diagram as well as the sRGB one, which is delimited by the dashed triangle. It can be seen that a considerable amount of colors lies outside the sRGB triangle (notice that all colors shown in the figure are anyway sRGB since a monitor is used to display the image).

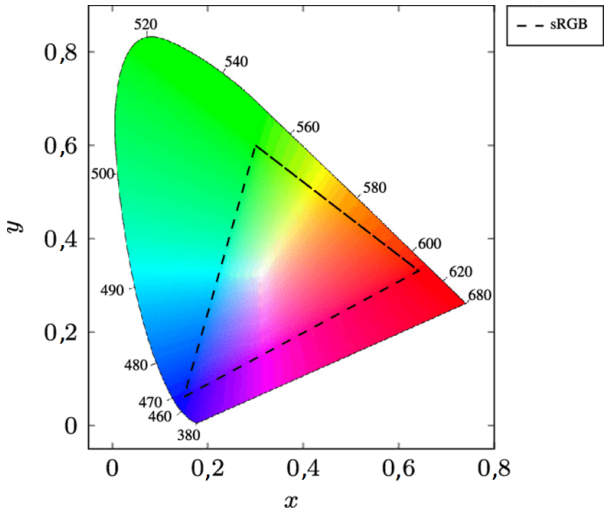

Figure 4.6: CIE xyY color space chromaticity diagram including the sRGB one (used for displays). The white point in the centre is determined by the Standard Illuminant D65. Adapted from [40].

Since the model used to predict the color of the optical filters is computer-based, we need to base it on sRGB color coordinates. Therefore, a transformation method to convert XYZ values to RGB must be used. The conversion is accomplished by multiplying the XYZ vector by a transformation matrix M [38]:

$$\begin{bmatrix} R \\ G \\ B \end{bmatrix} = [M]^{-1} \begin{bmatrix} X \\ Y \\ Z \end{bmatrix} \tag{4.11}$$

The 3x3 transformation matrix is generated using the monitor's phosphor chromaticity coordinates and the reference white of the illuminating source. It must be noticed that the RGB values obtained after the transformation are linear, therefore another step is required to match the non-linear nature of the sensitivity of the human eye: a gamma correction [41]. Implementing a gamma correction to go from linear to non-linear sRGB coordinates is crucial for an efficient color rendering. The interested reader is encouraged to find more information on the transformation matrix and the gamma correction on [38], [41] and [42].

Now that it is clear how humans perceive colors, we can go back to the mathematical model used for the simulations. The model, implemented in Matlab, was developed by J. C. Ortiz Lizcano during his Master thesis project [30]. The operations performed are summarized in the flow chart illustrated in figure 4.7.

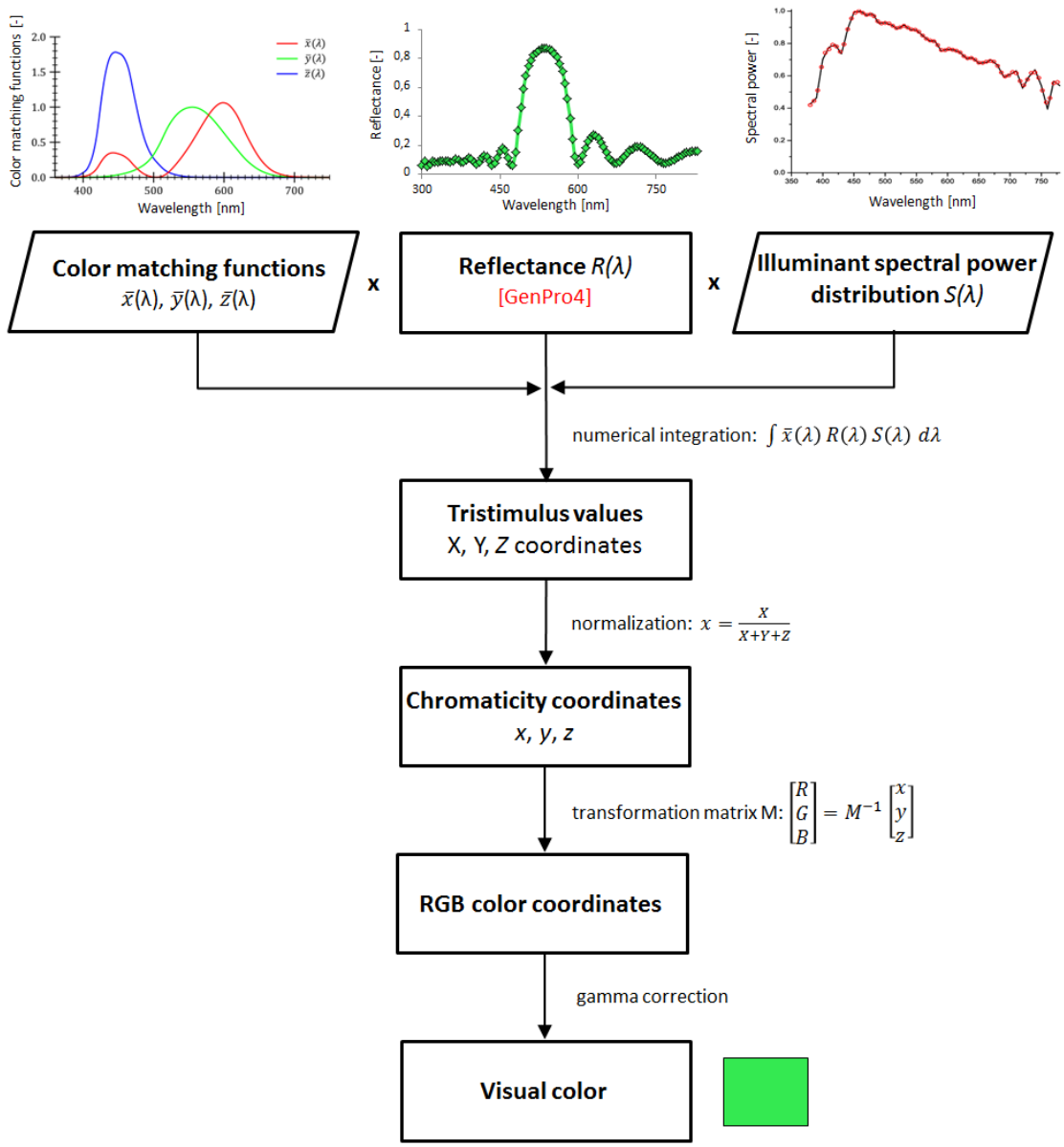

Figure 4.7: Flow chart showing the operations performed in Matlab to transform the reflectance spectrum into RGB values then translated into a visible color.

As mentioned, there are three components necessary for the human perception of colors: a light source, an object to look at and an observer. Each of these components is represented by numerical values or functions that will be used to quantify the color perception in the form of a visible color. The Matlab model will therefore need as inputs: (1) the CIE color matching functions (accounting for the observer), (2) the spectral power distribution of the Standard Illuminant D65 (accounting for the light source), and (3) the reflectance pattern of the optical filter (accounting for the object). Note that, while the first two parameters are known and simply loaded in the code, the reflectance pattern will come out as output from the GenPro4 ray-tracing simulation. It is also worth to mention that the D65 Standard Illuminant has been chosen because it is the most adequate to reproduce a daylight condition, as condition needed for color perception of solar modules and BIPV systems in reality.

As expressed in equations 4.8, 4.9 and 4.10, the three mentioned parameters are multiplied and integrated over the entire visible spectrum. In this way, the tri-stimulus values are obtained. After normalizing X, Y and Z with respect to the illuminant, the transformation from XYZ to RGB coordinates is performed. Adjusting the transformation matrix to the right illuminant source (D65 in our case) and implementing a gamma correction for an efficient rendering, finally the RGB coordinates are obtained and a visible color can be displayed on the screen.

4.1.3. DeltaE 2000 Color difference formula

How can we quantify the difference between two perceived colors?
The need to express a color difference in a quantitative, rather than qualitative, way is crucial when it comes to colorimetric analysis or any study where color consistency is required. The concept of *difference* is in this case associated with the concept of *distance*. Since we are working in a tri-dimensional space where each color occupies a specific point descried by three coordinates, we can simplify this problem by assuming that the difference between two colors is given by the distance between their points in the color space. This also means that the color difference metric will be dependent on the specific color space used.

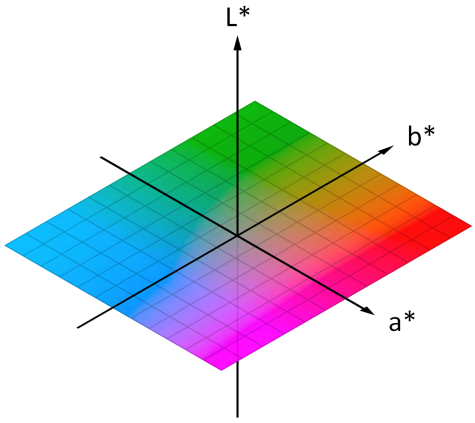

Figure 4.8: CIELAB color space.

In 1976 the CIE established a color difference formula, called CIELAB ΔE^*, which is based on the CIELAB color space. This space is characterized by the coordinates: L^*, a^* and b^*. As can be seen if figure 4.8, L^* represents the lightness (vertical shift: the higher the value of L^* the brighter the color), while a^* and b^* represent, respectively, the green-to-red and the blue–to-yellow color shift [43]. The first formulation of the CIELAB color difference formula was the CIE76. Given two colors (L_1^*, a_1^*, b_1^*) and (L_2^*, a_2^*, b_2^*), the color difference is defined as:

$$\Delta E_{ab}^* = \sqrt{(L_2^* - L_1^*)^2 + (a_2^* - a_1^*)^2 + (b_2^* - b_1^*)^2}. \tag{4.12}$$

It can be noticed that this is nothing but the Eucledian distance between two points in a 3D space. However, this definition does not take into account the non-uniformities inherent to the CIELAB space, for example due to the fact that the human eyes are more sensitive to certain colors. Hence, over the years, the CIE released more complex and complete versions, the 1994 (ΔE^*_{94}) and 2000 (ΔE^*_{00}) formulas. The ΔE^*_{00} is nowadays the most complete and reliable formula, yet the most complicated, as it is equipped with weighting functions for correcting the lack of uniformity of CIELAB and parametric factors to keep into account the influence of experimental viewing conditions. For further information on the mathematical expression and derivation of the formula, the interested reader is referred to [44].

The ΔE^*_{00} metric ranges from 0 to 100, where the lower the value the more similar the colors. The threshold for the human eye to perceive the difference between two colors (also known as *just-noticeable difference* or JND) is commonly set at around 2.3 [45]; the following table can be used as a reference to understand the color perception associated with the respective ΔE^*_{00} range.

Table 4.1: General color perceptions associated with ΔE^*_{00} values. Adapted from [43].

Δ E	Perception
≤ 1.0	Not perceptible by human eyes
1 - 2	Perceptible through close observation
2 - 10	Perceptible at a glance
11 - 49	Colors are more similar than opposite
100	Colors are exact opposite

On the basis of what said before, the ΔE^*_{00} will be the metric used from now on to evaluate the difference between the colors of the filters when varying the angle of incidence, and the goal of the work will be tying to reduce as much as possible its value.

4.2. Simulation results

The first step of this angular resilience study was the creation of the so-called *color matrices*. Using the model described in the previous section and varying the thicknesses of both SiN_x and SiO_2 from 50 to 160 nm (every 10 nm) the sRGB values, i.e. the colors, corresponding to every possible combination of thicknesses were obtained. At first, this was done for the simplest configuration: filter deposited on a glass where both sides are flat.

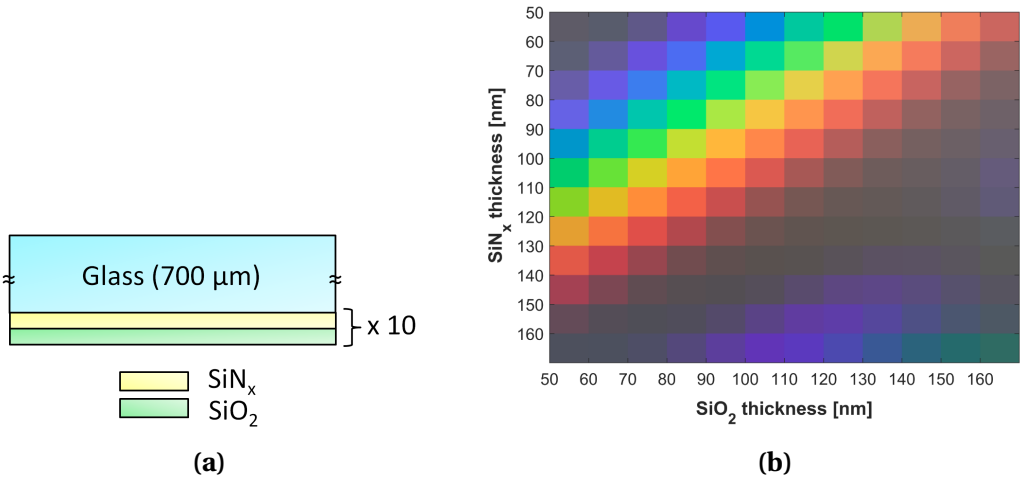

Figure 4.9: (a) Flat glass filter configuration. **(b)** Corresponding color matrix.

Figure 4.9 shows the schematic of the filter and the associated color matrix, from which it can be noticed that a wide range of colors can be obtained simply by varying the layers' thicknesses. It is important to note that the grey colors corresponding to some thickness combinations have to be interpreted as transparent. For those thickness combinations, the interference effect that boosts the reflectance peak takes place at wavelengths outside the visible range, meaning that only a reflection of around 4%, which is typical of a normal untreated glass, is present in the range of interest. This low reflection generates low sRGB values that, being the same amount for each of the three primary components, are perceived by us as a grey color.

It must be noticed that in the ray-tracing simulations done to generate the color matrix the rays are assumed to arrive from normal incidence. Therefore, the next step will be to choose a fixed combination of thicknesses and perform the simulations by varying the angle of incidence of the light. The results of these simulations are shown in figure 4.10, where three colors have been selected from the color matrix: a green (SiO_2=70 nm and SiN_x=90 nm), a red (SiO_2=90 nm and SiN_x=110 nm) and a yellow (SiO_2=100 nm and SiN_x=80 nm).

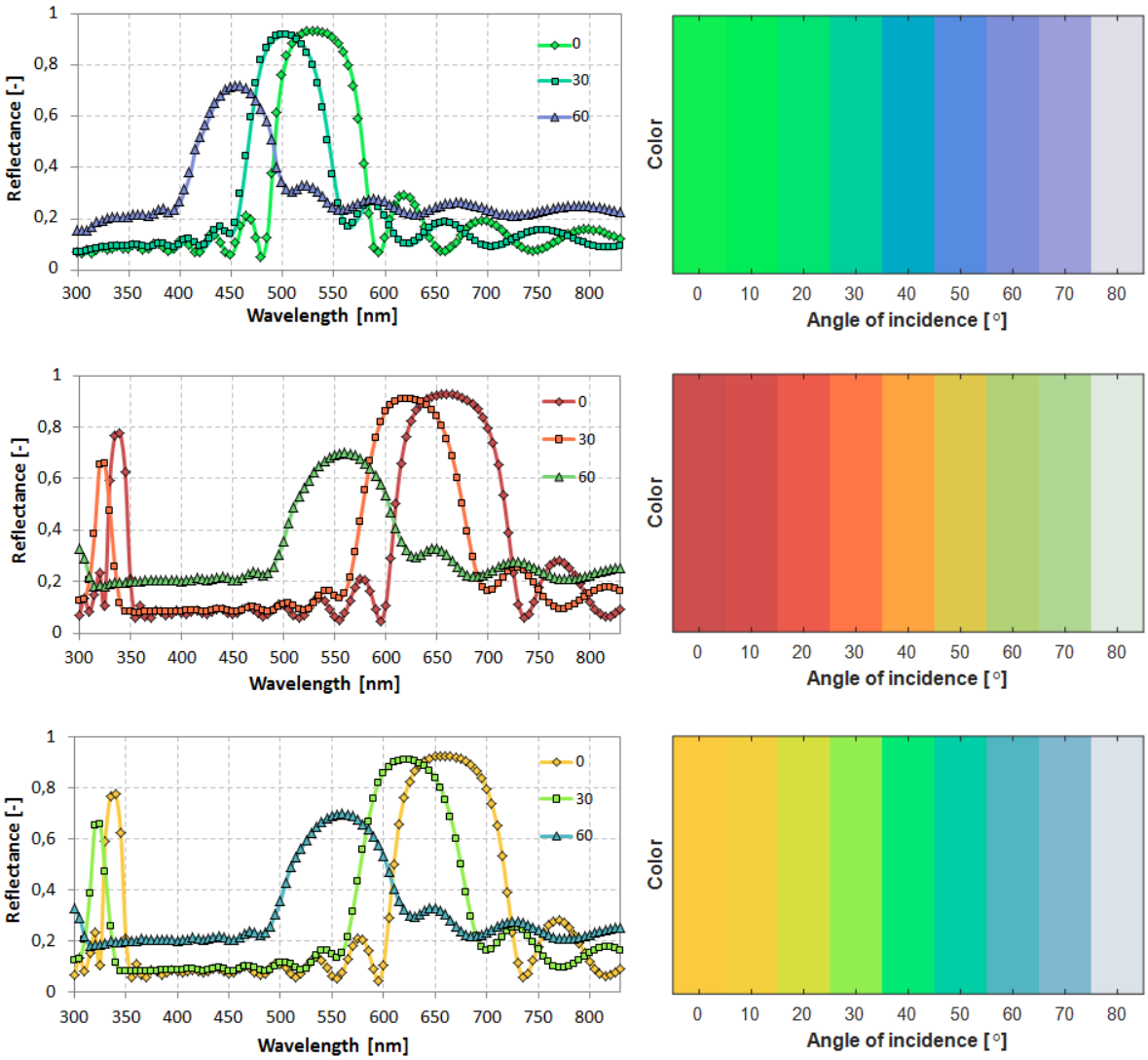

Figure 4.10: Effect of changing angle of incidence on reflectance curves and relative color perception for three different thicknesses combinations. Top: green (SiO_2=70 nm - SiN_x=90 nm); middle: red (SiO_2=90 nm - SiN_x=110 nm); bottom: yellow (SiO_2=100 nm - SiN_x=80 nm).

On the left-hand side of the image the reflectance patterns are plotted; for clarity, only the curves at 0°, 30° and 60° are shown. As expected, when the angle of incidence increases, the reflectance peaks shift towards lower wavelength values. Due to this, the color perception of the filters changes considerably, as shown in the right-hand side of the figure.

At the beginning, the approaches that were investigated to improve the angular resilience of the IF were mainly related to the materials properties, the disposition and the thicknesses of the layers. For example, it was found in literature that when using thicknesses of the high index materials that are at least 3 times higher than the thicknesses of the low index material (i.e. $(\text{L-3H})^p$), better angular stability can be achieved [46]. However, when this approach was applied to our model, the results were not positive: a filter with SiO_2=70 nm - SiN_x=240 nm provided the same color shift of a filter with SiO_2=70 nm - SiN_x=90 nm, as the one showed on the top right of figure 4.10.

Therefore, a different and more successful strategy started to be investigated. It was found out that the change in color has to be attributed not only to the layers thicknesses and material optical properties, but also to the configuration of the interfaces that the light has to traverse. Indeed, the interference effect is dependent on the optical path of the light through the various layers, which will change when the surface geometry is changed. To prove what stated, three different color matrices were generated, as reported in figure 4.11. The first one (left) was already presented in figure 4.9b, as it is obtained with a flat configuration that we will call **flat-flat**; the second one (middle) is obtained with a **textured-flat** configuration, meaning that the outer part of the glass is textured, while the filter is deposited on the flat inner side; the third one (right) is obtained with a **textured-textured** structure, where both sides of the glass, where the light enters and where the filter is deposited, are assumed to be textured. Note that in these configurations the texturing features are random pyramids.

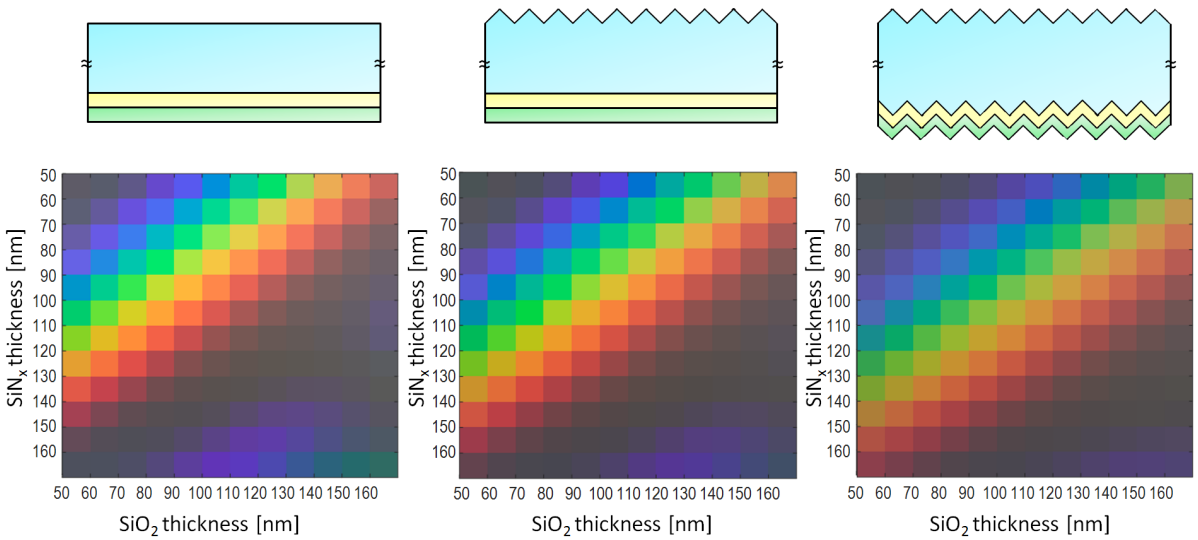

Figure 4.11: Variation of color matrices for interference filters with different surfaces geometries: flat-flat (left), textured-flat (middle) and textured-textured (right).

Although similar, the three color matrices shown in figure 4.11 present some differences. In particular, two important aspects can be noticed: first, we can observe a shift in the position of the colors within the matrix (the colored strip tends towards higher values of both SiO_2 and SiN_x - bottom right); secondly, with increasing texturing the colors lose brightness.

This second aspect is expected since a textured surface reduces the reflection. Texturing is indeed a common technique used for anti-reflecting purposes and for enhancing the light coupling into the absorber layer of solar cells. When a light ray arrives to a textured interface it undergoes

scattering and, according to Fresnel and Snell's laws, part of the reflected ray will hit another part of the textured surface, resulting in additional transmission through the layer and a general reduction in reflection [23]. This is translated in loss of brightness.

The two aspects emerging from the analysis of the color matrices, i.e. different colors and reduced reflection, can be more clearly observed when plotting the reflectance curves of the three filter configurations, as in figure 4.12. For a fixed thicknesses combination, SiO_2=70 nm and SiN_x=90 nm in this case, the colors obtained in the three cases are different, the text-text configuration providing the lowest reflectance peak.

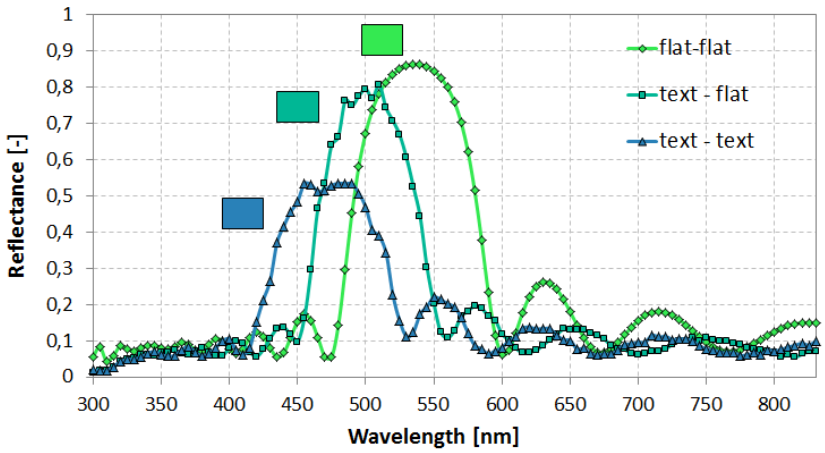

Figure 4.12: Influence of the filter surface geometry on the reflectance curves for the same thicknesses combination SiO_2=70 nm - SiN_x=90 nm. Normal incidence is assumed.

Once verified that the geometry of the interfaces between the materials plays a significant role in the color appearance, we can now check how these different geometries behave when the angle of incidence is varied. Figure 4.13 shows the perceived colors of the three interference filters with the same thicknesses as in the example above (70 and 90 nm) as a function of the angle of incidence. To express quantitatively the difference in colors, the ΔE_{2000} formula introduced in the previous section has been used. It is important to note that the color difference formula is applied comparing the RGB coordinates of the colors at each AOI always with respect to the normal incidence case (0°) which is taken as reference.

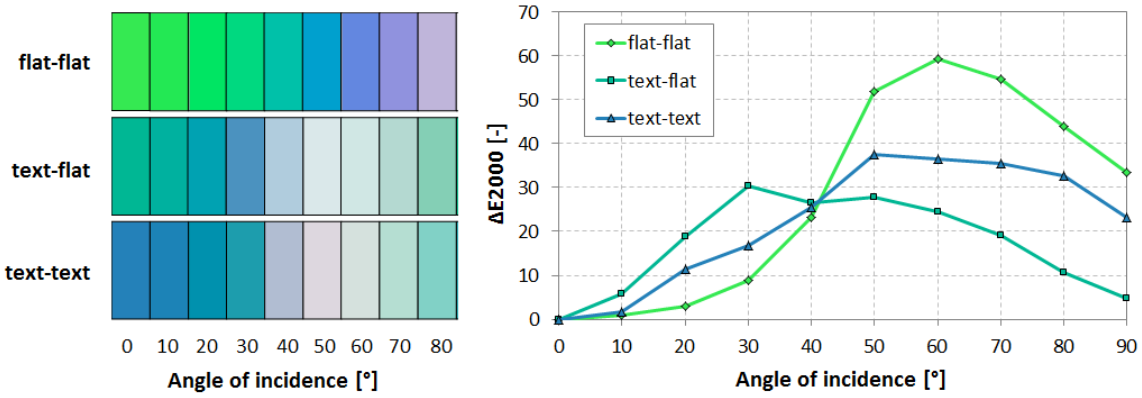

Figure 4.13: Color perception as function of AOI of flat-flat, textured-flat and textured-textured filters (left) and their color difference quantification in terms of ΔE_{2000} values (right).

Looking at the plot on the right-hand side of figure 4.13, it can be concluded that while a flat

geometry provides very high values of ΔE_{2000}, approaching 60 for high AOI, the textured configurations behave better, limiting the ΔE_{2000} to values below 30 or 40 for the text-flat and text-text cases, respectively. Despite of the general improvement, these values are still well above the threshold for distinguishing two different colors; an acceptable value of ΔE would be around 10, hence, the angular resilience of the colored optic filters should be further improved.

4.2.1. Angular resilience: a surface optimization problem

The preliminary results presented so far prove that varying the geometry of the surface on either sides of the glass where an optical filter is deposited helps in increasing the angular resilience of the color. To understand why this happens, it is important to recall that reflection is strongly influenced by the surface roughness.

Reflection of light can be roughly categorized into two types: specular and diffuse reflection. *Specular reflection* is characteristic of smooth surfaces that reflect all light arriving from a given direction at the same angle with respect to the normal, assuming a mirror-like behaviour. On the other hand, *diffuse reflection* takes place when light is scattered away from the surface in a range of directions rather than just one, and it is typical of rough surfaces [47]. This happens because when a surface is roughly textured it presents many different orientations to the incident rays, which are therefore scattered out in every direction. Most of the objects we see every day do not have perfectly smooth or diffusive surfaces, hence, their reflections are often a combination of both diffuse and specular components. One manifestation of this is the *spread reflection*, characterized by a dominant directional component that is partially diffused by the surface irregularities, as visible in figure 4.14.

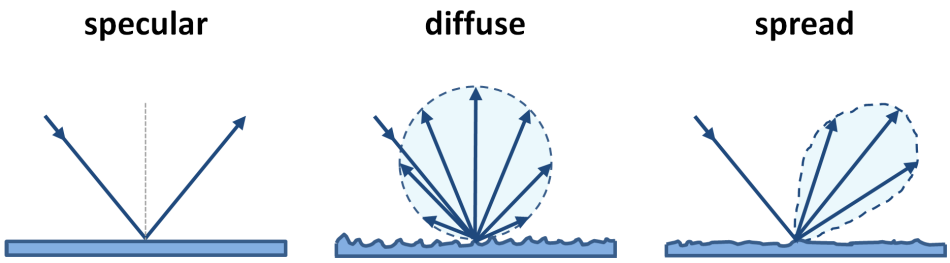

Figure 4.14: Types of reflection: specular, diffuse and spread.

Specular reflection also implies that the observer can see the light only when his eyes are at the same position of the reflected rays. On the contrary, when diffuse reflection occurs, the eyes of an observer can detect the light from any positions, independently of the light source direction.

Keeping this in mind, the main idea behind our IF angular resilience study is trying to obtain diffuse reflection from the outer surface of the glass, so that the angular distribution of the reflected light is as much as possible independent of the illuminating angle. Therefore, the angular resilience analysis turned into an optimization problem aimed at finding the best geometrical shape for the surface texture of the glass.

We will first focus on the so-called *text-flat* configuration, in which the external side of the glass is textured, while the inner side, where the 20-layer filter is deposited, is flat. For now, no solar cell or any other layer is considered. To find the best geometry, the following features of the surface roughness started to be investigated and interchanged:

- **shape**: pyramids, hemispheres (aspect ratio?);
- **orientation**: up, inverted;
- **regularity:** periodic, random;
- **dimension**: 1D (grooves), 2D.

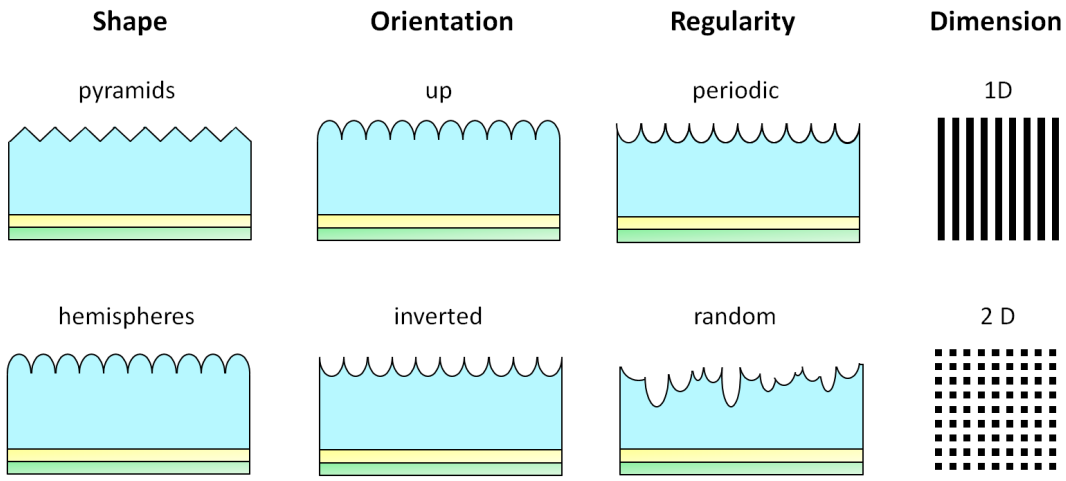

Figure 4.15: Schematics of possible glass geometries when changing the features shape, orientation, regularity and space dimension.

Figure 4.15 shows simplified schematics of these optimization criteria and possible glass geometries. As for the feature shape, the main geometries considered were pyramids and hemispheres; for the latter, simulations were performed also changing the aspect ratio. Another parameter that was kept into account was the size of these features. Simulations were conducted for sizes in the range of 1 to 10 μm, but as expected, as long as the size of the roughness is larger than the wavelength of incident light, ray optics applies and the surface roughness does not influence the interference effect due to the multilayer filter, hence the results are roughly unchanged. As for the orientation, the features were tested in both the upwards and inverted configuration. Also the feature regularity was investigated, testing both periodic structures and random texturing (e.g. random craters). Finally, both 1 dimensional and 2 dimensional (e.g. grooves) geometries were tested.

The most relevant results are shown in figure 4.16, taking as an example a green colored filter with SiO_2 and SiN_x thicknesses of 70 and 100 nm, respectively. As can be noticed, with random pyramids and random craters, in both upwards and inverted configurations, a rather significant color shift can still be perceived. In particular, the pyramids show that starting already from around 40° of AOI the reflection is so high that a whitish color is obtained (white is obtained when light of almost every wavelength is reflected); this is unwanted because it would cause very high losses for PV applications. Random craters, although presenting a more marked color shift, do not show the same behaviour as the random pyramids. This observation already shows that roughness with smoother curvatures, such us hemispherical or elliptic shapes, is more promising.

On the other hand, when periodicity is introduced the results significantly improve. It can be observed that when the features are placed in the upwards direction, i.e. when they have a convex shape, they seem to reflect more light at very high AOI, since the colors become more white. However, when the features are inverted (concave shape), this effect is reduced, and the color remains rather consistent up until 80°. Among the inverted hemispheres (2D) and the inverted hemispherical grooves (1D), the best result is obtained with the latter.

4.2.2. Most angular resilient configurations

From the previous analysis emerged that the hemispherical shape is the most promising and that periodicity seems to be helpful for the angular consistency of the color. It was also found that the 1D configuration in the form of hemispherical grooves shows similar or even better results than the 2D configuration. Since a 1D structure is desirable also from more practical points of view related to fabrication and cleaning purposes, this configuration is the preferred one.

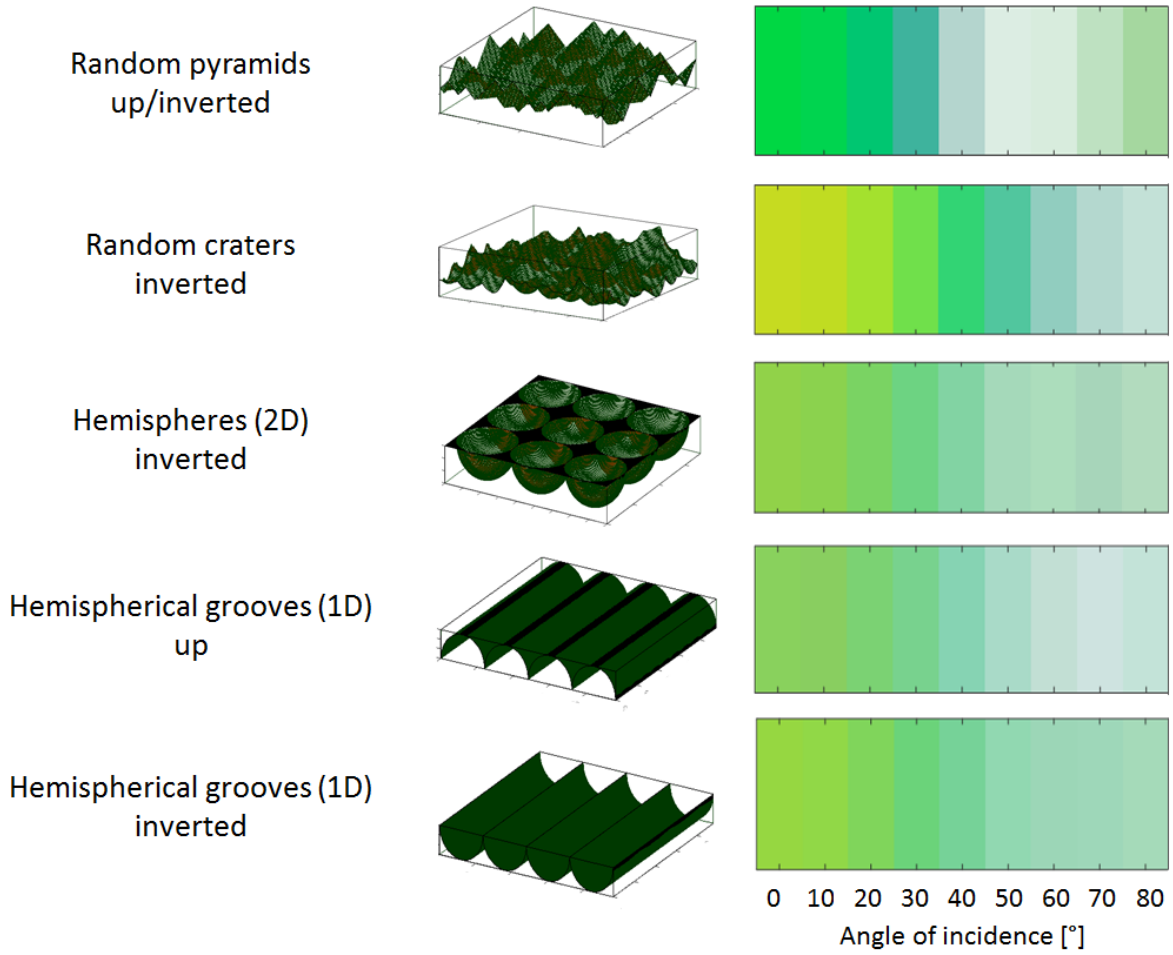

Figure 4.16: Effect of angle of incidence on color perception for five different texturing geometries of the front side of the glass. Results are relative to a 20-layer filter with SiO_2 = 70 nm and SiN_x = 100 nm.

With the aim of increasing even further the color angular resilience, the option of texturing also the inner side of the glass where the filter is deposited (*text-text* configuration) was further investigated. Simulations were performed by using hemispherical grooves in both upwards and inverted direction and it was found that the best configuration is what we will call *concave lens* structure, characterized by inverted hemispherical grooves on the top side and upwards hemispherical grooves on the bottom side, to form indeed a shape that resembles a concave lens. The simulation results for the best angular resilient configurations using both approaches, *text-flat* and *text-text*, are presented first for the case of a single glass substrate, and subsequently for the full module structure (glass on top of a solar cell).

Glass

Figure 4.17 shows the results obtained for the case of a 20-layer interference filter deposited on a 700 μm glass. The results are shown in terms of colored bars and then quantified through the ΔE color-difference formula. Three different combinations of thicknesses of SiO_2 and SiN_x have been chosen to represent three different colors, approximately a green, a blue and an orange. As expected, when the filter side of the glass is flat (results on the left-hand side of the figure) the colors at low AOI appear brighter than for the *textured-textured* case. However, when the AOI increases the colors tend to become whitish, indicating high reflectance values. Translated in quantitative terms, the ΔE

reaches a value of 25 for the green and blue filters, and slightly more than 30 for the orange one.

On the other hand, whit the *concave lens* structure, more homogeneous and consistent colors through all the angles of incidence can be observed. Although some brightness is lost and the colors in general appear more opaque, the angular resilience of the filter is improved to ΔE values below 15 even at 80°, independently of the color considered.

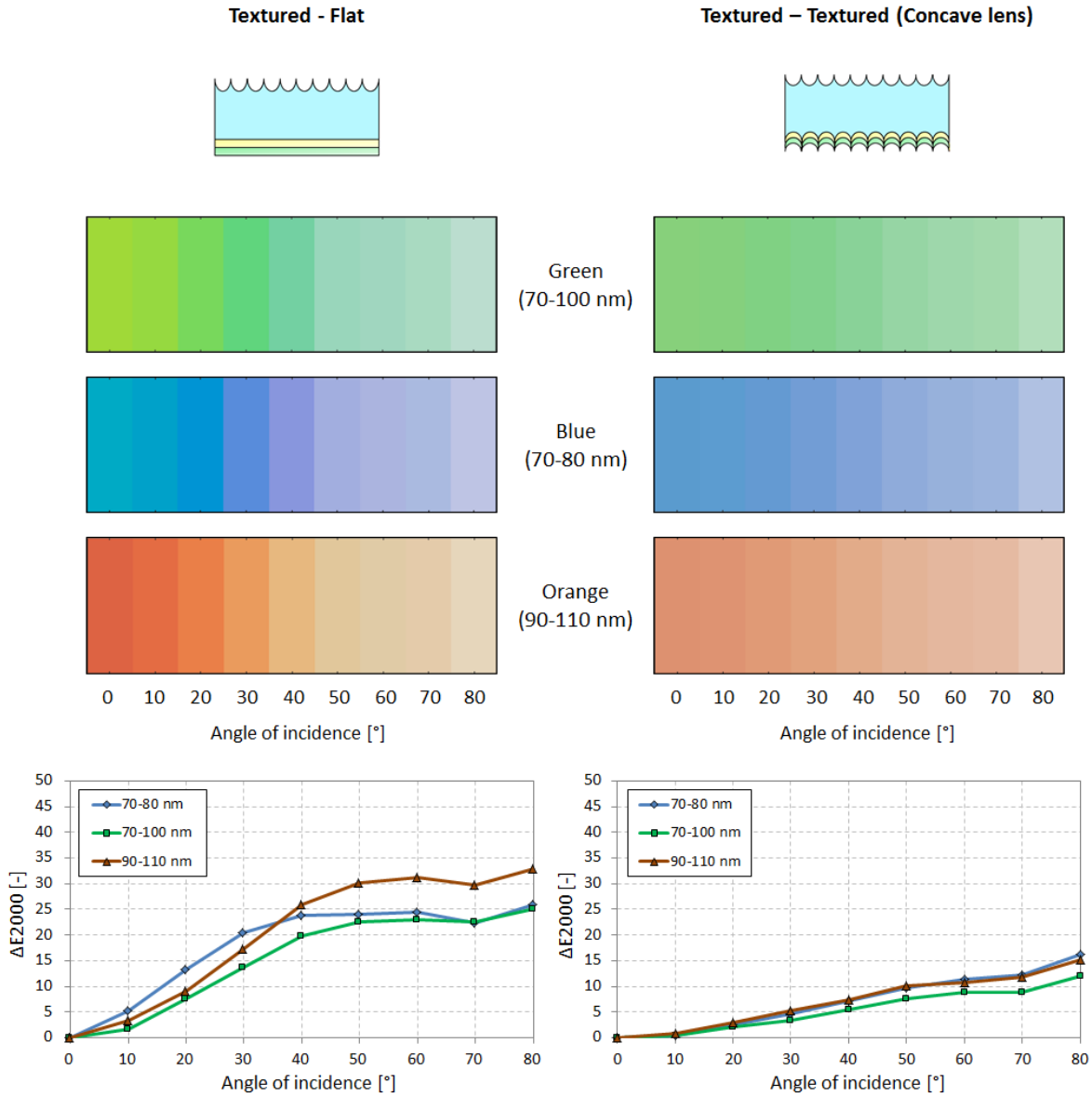

Figure 4.17: GLASS case: comparison in terms of perceived colors and ΔE between the most angular resilient structures. On the left: *text-flat* configuration with hemispherical grooves; on the right: *text-text* configuration with hemispherical grooves on both sides forming a concave lens structure.

It is also interesting to look at how the reflectance curves of the two filter configurations change with the AOI. As an example, the reflectance patterns of the green filter with thicknesses SiO_2 = 70 nm and SiN_x = 100 nm have been considered and they are shown in figure 4.18. From the plots it can be noticed that the typical blue-shift (shift of reflectance peak towards lower wavelengths) is much more evident for the *text-flat* case than for the *text-text* one. Additionally, it can be observed

how the reflectance peaks of the double-textured configuration for high AOI are considerably lower than in the other case, confirming and justifying the more opaque colors.

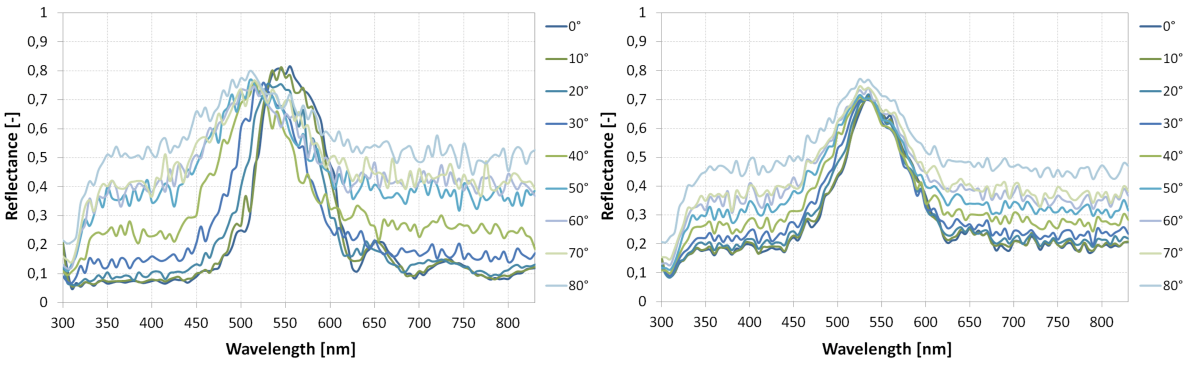

Figure 4.18: GLASS case: effect of angle of incidence on the reflectance curves of *text-flat* **(a)** and *concave lens* **(b)** filter structures.

Module structure

To simulate what would be the outcome in terms of color perception when the filter is applied on a PV module we have to incorporate the presence of the solar cell in the optical model. For accurate results, the complete PV module structure has been simulated, including the EVA layers and the back glass. An Al-BSF (Al Back Surface Field) cell has been considered in the simulations, since this is also the type of cell used for the actual fabrication of the colored mini-modules. The simulated module structure is shown in figure 4.19, where the layers thicknesses are not to scale. For simplicity, in some of the following figures the thinnest layers of the cell, e.g. ARC and back passivation layers, are omitted.

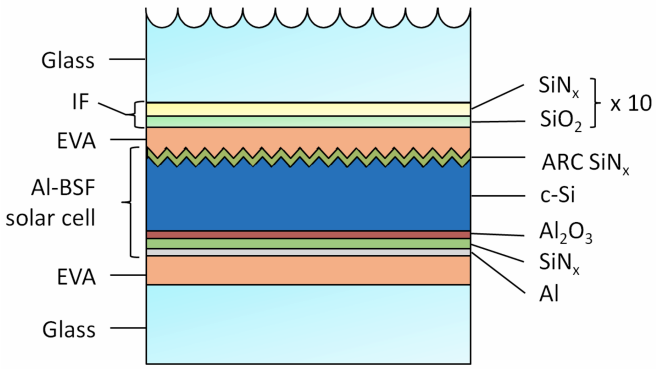

Figure 4.19: Module structure used in the optical model: *glass - filter - EVA - solar cell - EVA - glass.*

With the same top glass configurations and the same filter structure, the simulations have been repeated by adding the additional PV module's layers to the model. The results of the angular resilience analysis are visible in figure 4.20.

When only the glass was considered, it was pointed out that in the *text-flat* configuration the filter became more transparent at high AOI, due to the fact that the high peak of reflection (responsible for the color) was not so pronounced anymore and rather flat reflectance profiles took over. Because of this, when dark objects are placed underneath the filter, we will start to perceive also the color of the background. This is why we see that for high AOI (approximately above 40°), the colors become darker and the hue of each filter adds up with the blue of the cell. Noticeably, this causes a

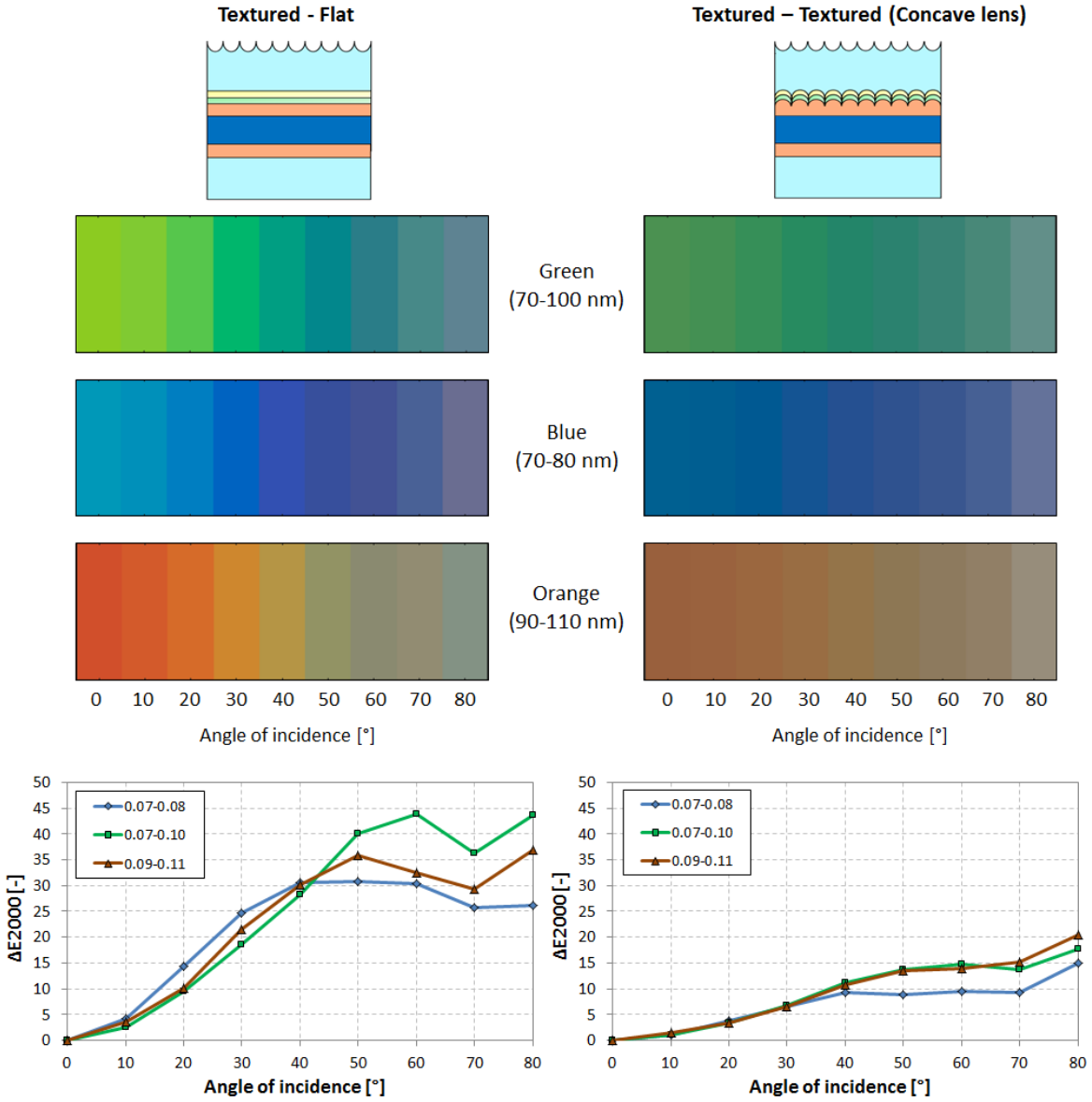

Figure 4.20: MODULE case: comparison in terms of perceived colors and ΔE between the most angular resilient structures. Left: *text-flat* configuration with hemispherical grooves; Right: *text-text* configuration with hemispherical grooves on both sides forming a concave lens structure.

rather significant color shift, with ΔE that almost touch the value of 45 in the worst case of a green filter.

On the other hand, it can be observed that with the *concave lens* structure very good angular stability is achieved, with ΔE values below 10 until 40° and and never exceeding 20 also for very high AOI. The drawback of this configuration is that all colors generally became darker. For instance, it can be noticed that the layers combination SiO_2 = 90 nm - SiN_x = 110 nm that so far has provided an orange color, now generated a brown hue. The reduction in brightness is clearly supported by the reflectance curves shown in figure 4.21, which for the *concave lens* are found to be always lower than 30%. Therefore, it should be kept in mind that with this filter structure a very good angular resilience can be obtained at the expenses of a more limited range of available colors.

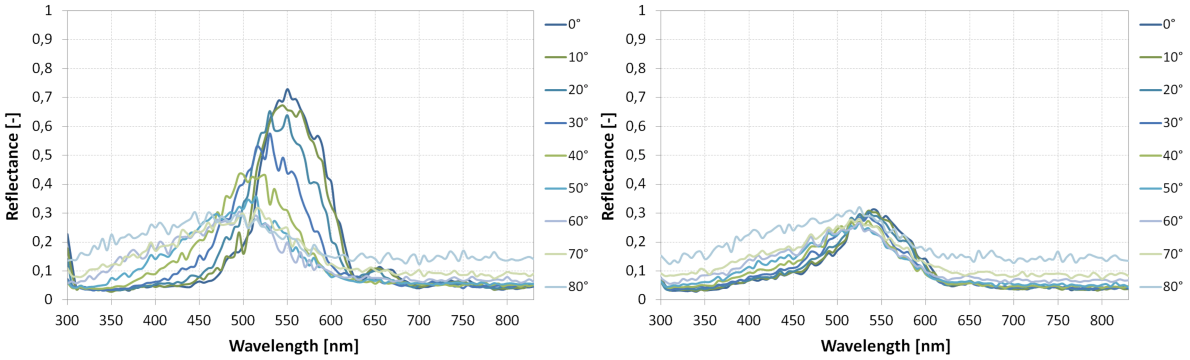

Figure 4.21: MODULE case: effect of angle of incidence on the reflectance curves of *text-flat* **(a)** and *concave lens* **(b)** filter structures.

4.3. Conclusions

The color of an interference filter is highly dependent on the angle of incidence of the light source. This phenomenon, known as *blue-shift*, is caused by the fact that the light rays have to traverse a longer path within the filter layers, therefore changing the wavelength at which the reflected rays interfere constructively. The change in color perception when changing the AOI, and consequently the angle of observation, is considered a relevant drawback for designers and architects involved in BIPV projects. For this reason, the first part of this thesis work was dedicated to improving the angular resilience of IF, and the goal of this chapter was to present the main results of this study.

In the first section, the optical model used to simulated the color of IF has been described. To obtain the reflectance spectrum of these multilayer structures the ray-tracing software GenPro4 was used, while a mathematical algorithm based on the CIE color perception was employed to translate the optical information into color coordinates. To fully understand the model, some basic knowledge on human color perception have been provided as well. Since the perception of colors is a human sensory sensation, it was necessary to introduce a mathematical figure of merit that allowed us to describe the color difference in quantitative term: the ΔE_{2000} color-difference formula.

In the second section, the main results of the study have been presented. It was found that the geometry of the interfaces between the various materials plays a significant role in the color appearance. While with flat surfaces the reflection is specular, i.e. highly directional, a textured surface generates diffuse reflection. Therefore, the study turned into a surface optimization problem aimed at finding the best texturing profile, so that the angular distribution of the reflected light would be as much as possible independent of the illuminating angle. It emerged that the hemispherical shape is the most promising, that periodic structure worked better than random ones and that 1D configurations present better results than 2D structures. Therefore, a profile with inverted hemispherical grooves was found to be the best configuration. This geometry was applied first only on the external side of the glass (*text-flat*) and then also on the filter side (*text-text* or *concave lens*). Although more complex, texturing both sides of the glass helps in increasing even further the angular resilience.

For simulations regarding only glass, without any other layer, results showed very good angular resilience for both configurations. Compared to a flat glass with ΔE value up until 60, it was now possible to achieve ΔE between 25-35 for the *text-flat* case and below 15 for the *concave lens*. When the full PV module structure was simulated, only the *concave lens* configuration seemed to produce highly resilient colors, with ΔE less than 20 up until 80°. This means that color difference can be hardly perceived when changing angle of incidence. However, with this *concave lens* configuration, the significant improvement in terms of angular resilience comes at the expenses of a more limited range of available colors.

5

Colored mini-modules fabrication and optical characterization

The optical model described in the previous section showed that by depositing an interference filter on the encapsulating glass of a solar module it is possible to change its color appearance, hence increasing the aesthetic flexibility of the PV technology. Furthermore, it was shown that by conveniently texturing the surface of the glass, on one or both sides, the color would be highly consistent when illuminated or looked from different angles. To prove the validity of the model and verify the feasibility of this technology, experimental demonstrations are needed. This leads us to the second research question of this work:

Is it possible to fabricate colored mini-modules based on interference filters? If so, does the optical behaviour of the colored demonstrators validate the optical model?

In this chapter, the results of the fabrication process will be presented and the optical performance of the fabricated colored mini-modules will be analyzed. In the first section, the mini-module design will be described, as well as the the required steps needed for the fabrication. Secondly, the experimental setups for both fabrication and optical characterization are presented. In the third section, the five colored mini-modules that have been fabricated will be shown. The chapter will end with the optical characterization of the colored modules, meant to validate the optical model.

5.1. Mini-module design and fabrication workflow

The mini-module has been designed keeping into account several practical aspects, in particular the limiting size of the encapsulating glass, set to a maximum of 10 x 10 cm^2. Indeed, this is the maximum area over which it was possible to obtain a spatially homogeneous deposition of the multilayer filter with the PECVD machines present at the TU Delft laboratories. For this reason, cut solar cells with very small size had to be used.

The chosen mini-module design is made of 6 cut solar cells with dimension 4,5 x 2,95 cm^2 connected in series along two rows, as shown in figure 5.1a. The layers forming the whole module stack are visible in figure 5.1b. A glass-glass configuration has been adopted, meaning that both front and rear surface of the module will be made of glass. In order to manufacture colored mini-modules, the front glass shown in figure 5.1b will be then substituted with the colored filter (glass + multilayer stack). As encapsulant material, EVA (ethyl vinyl acetate) has been used, in order to provide adhesion between the cells, the top and the rear layers of the PV module.

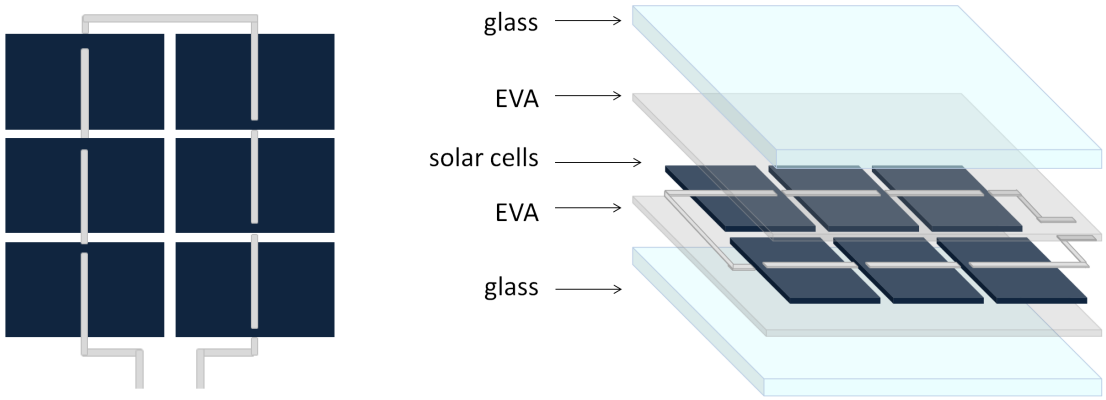

(a) **(b)**

Figure 5.1: (a) Module configuration: 6 series-interconnected solar cells. **(b)** Schematic of the module stack: interconnected cells sandwiched on both sides by EVA and glass layers.

In order to fabricate such mini-module, three main steps have to be performed:

- **Cutting**: in order to reduce the cell size and fit the desired number of cells within a 10 x 10 cm^2 glass;
- **Soldering**: to provide electrical interconnection between the solar cells;
- **Lamination**: to allow the polymerization of the EVA and bond all the PV module layers together.

In addition to the above mentioned steps, it must be considered the additional process required to build the interference filter:

- **PECVD filter deposition**: in order to provide color to the external glass of the PV module.

A more in-depth explanation of the processes will be given in the following section, together with the description of the setups and materials used for the fabrication.

5.2. Fabrication and characterization tools

A fiber laser cutter, an analog soldering station and a laminator were used to manufacture the mini-modules, while a PECVD machine was utilized to deposited the multilayer filter on the glass. To perform the optical assessment of the colored mini-modules a spectrophotomer was used. Each of the following subsection will be dedicated to the description of the above mentioned experimental setups.

5.2.1. Fiber Laser Cutter

To cut the solar cells, the 30W fiber laser cutter by Lasergraaf shown in figure 5.2a has been used [48]. A fiber laser is a device in which the active gain medium is an optical fiber doped with a rare-earth element, in this case ytterbium. This machine is able to mark and eventually cut solar cells and other materials thanks to the high energy density collected in the focus point of the the laser beam, which causes the material to melt and evaporate. As shown in figure 5.2b, the laser beam is steered by controllable mirrors through a θ-lens, which is a particular type of lens able to maintain its focus throughout a plane, rather than focusing on just one spot [49]. The monochromatic beam can be focused anywhere on the material to be cut within the plane defined by the θ-lens; hence, cuts of any different shape can be made.The machine guarantees high flexibility for optimizing the

cutting process, due to the fact that many parameters can be adjusted and controlled, e.g. laser power, scanning speed, frequency, pulse width and number of scans.

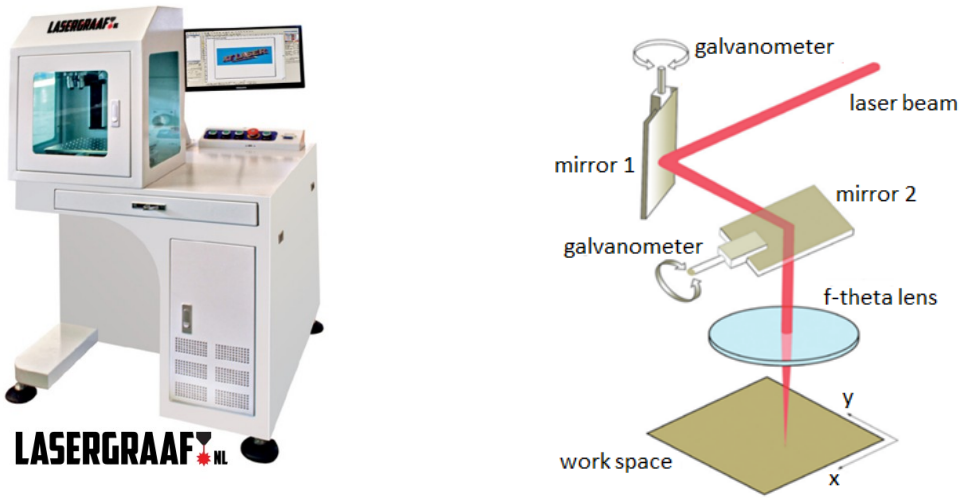

(a) **(b)**

Figure 5.2: **(a)** Lasergraaf fiber laser cutter and working station. Adapted from [48]. **(b)** Schematic of laser cutter working principle. Adapted from [50].

The solar cells used for the mini-modules manufacture are mono-crystalline Al-BSF cells of size 15,675 x 15,675 cm^2 produced by ExcelTon [51]. The cells have 3 front silver bus bars, each one with 4 soldering pads on the rear side. This configuration allowed to perform the laser cutting in order to obtain 12 mini solar cells out of each cell. As already mentioned, the size of the cut mini-cells is 4,5 x 2,95 cm^2. The full and cut cells are shown in the schematic of figure 5.3.

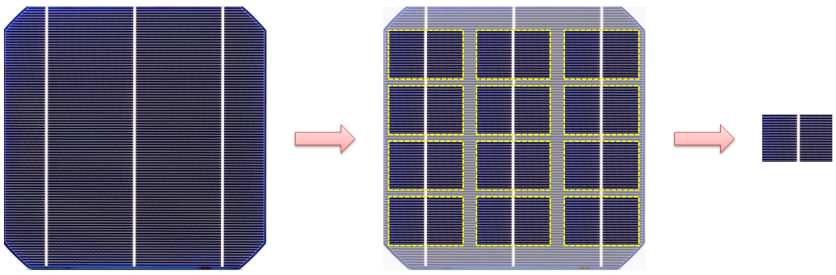

Figure 5.3: Laser cutting process allowing to obtain 12 mini-cell out of each full-size cell.

To effectively cut these solar cells, the laser parameters summarized in table 5.1 were used.

Table 5.1: Laser cutter parameters used for cutting mono Al-BSF solar cells.

Laser Parameter	Unit	Value
Mark loops	[-]	50
Speed	[mm/s]	250
Power	[%]	100
Frequency	[kHz]	400
Pulse Width	[ns]	5

5.2.2. Soldering station

To provide electrical contacts and interconnect the solar cells an analog soldering station has been used. Soldering is the process in which two metals are joined together by heating up and melting a filler metal, called solderer, into the joint. When the solderer is not present and one of the two work pieces is directly melted, the process is called welding. To interconnect the solar cells we used flat copper tabbing wires coated on both sides with tin-based solderer. Hence, the tabbing wires were applied directly on the bus bars or on the rear pads and bond together without adding extra filler material.

The soldering process starts with the heating up the iron tip. We used an 80W Waller analog soldering station which allowed to control the temperature in the range 150-450°C [52]. Before passing the tips on the metals and let the actual soldering take place, an important step is required: the application of an acid flux. The acid flux acts as a cleaning agent by removing the oxidation from the surfaces of the two metals which forms due to the contact with the air [53]. By applying a layer of flux above the silver metallization of the cells, the soldering process is strongly facilitated. For this purpose we used a rosin flux dispensing pen. After applying the flux, tabbing wires wide 1,3 mm were positioned on top of the cell contacts, possibly using an holding tool to hold the tab wires in place. Moving the soldering iron from top to bottom, the wires have been melted and soldered on the cell. To cause the melting, a temperature of around 230°C was needed. As soon as the materials cooled down, the bonding took place. After having prepared all the needed cells with the tab wires on the front side, they could be interconnected. To make a series connection, the front side of each cell must be connected to the bottom side of the next cell. In this way, 6 cells have been interconnected with a 3 x 2 configuration, as shown 5.4. For the external wires coming out from the two lines of cells, wider tabs of 5 mm have been used. A space of around 1 mm has been left in-between the cells to avoid their mutual contact.

Figure 5.4: Soldering and solar cells interconnection steps.

It must be pointed out that the cells interconnection process is considered as the most critical process with respect to module production yield [53]. If it is not carefully controlled, cracks within the cells may arise and grow, eventually leading to cell breakage and severely impacting the module electrical performance. Being a brittle material, the silicon wafer needs careful attention in order to limit the stress levels caused by thermomechanical loads. This stress mainly originates from two factors related to the soldering process: the mismatch in the coefficients of thermal expansion (CTE) between copper ($16{,}5 \cdot 10^{-6}$ /°C) and silicon ($2{,}6 \cdot 10^{-6}$ /°C) and the elevated process temperatures for the metal joint formation [53]. The first is particularly delicate because during the cooling from solder melting temperature to room temperature, the copper ribbons contract much more than the silicon wafer, causing the tensile stress in the silicon that eventually leads it to crack.

5.2.3. Laminator

The last step of the module manufacture process, i.e. the bonding between the various layers, is performed by a laminator machine. An Experia lab laminator, owned by the PVMD group of TU Delft university, has been used for the project [54]. The machine, shown in figure 5.5, consists of two chambers separated by a flexible diaphragm and it is equipped with computerized control system.

Figure 5.5: Experia Laminator LAM600. Adapted from [54].

As shown in figure 5.1b, the PV module layers have been overlaid with the following sequence: back glass sheet - EVA layer - interconnected solar cells - EVA layer - front glass sheet. The loose module layup is introduced on top of the preheated bottom plate of the laminator.

The main steps of a lamination process are the following. At first, an evacuating phase takes place during which the air is removed and residual pressure is brought below 1 mbar. In the meanwhile, the bottom plate is heating up. During these steps, a lifting pin system holds the panel away from the heated lower plate; without pins the module would heat up too quickly risking damaging [53]. Once the base plate reaches the final process temperature of around 150 °C, the pins are lowered and the module homogeneously heats up until the EVA cross-linking is performed. At this point, air is introduced in the upper chamber and a compressing step takes place. The membrane presses on the laminate because of the pressure difference between the chambers, thus enhancing the distribution of the EVA and ensuring good adhesion between the layers [53]. The curing of the EVA needs a few minutes to effectively take place. Final steps are then venting and release of the chambers.

The machine allows to input personalized lamination recipes by varying the number of steps, time, temperature and pressure of the chambers. The recipe used for the mini-modules is reported in table 5.2.

Table 5.2: Lamination recipe used for the mini-modules fabrication.

Process	**Time [s]**	**p_{up} [mbar]**	**p_{down} [mbar]**	**T_{set} [°C]**	**Pins** [-]
Evacuating	120	0	0	80	up
Heating up	500	0	0	140	up
Compressing	60	150*	0	140	down
Curing	500	900	0	145	down
Venting	30	0	1000	145	down
Release	30	0	1000	145	up

* This value has been varied and optimized. Starting with a value of 900 mbar, typical of normal PV glasses, it was brought down to 50 mbar to avoid cracking of the used 700 μm glass. A good compromise between glass resilience and complete EVA curing was found to be at around 150 mbar.

5.2.4. Plasma Enhanced Chemical Vapour Deposition (PECVD)

The multistack interference filters have been deposited by an RF plasma enhanced chemical vapour deposition (PECVD) process. With this technique, thin films growth takes place through the adsorption on the substrate of the reactants generated in the plasma [29]. Depending on which precursor gases are used and their ratios, different compounds can be obtained. The precursor gases used in this work are silane (SiH_4), ammonia (NH_3) and carbon dioxide (CO_2); the first two have been used to form SiN_x layers, while silane and carbon dioxide have been used to make SiO_2 films. PECVD deposition is a well-established and commonly used technique, since it allows high quality film deposition and low operational temperature. To start the process, a plasma is created between two electrodes in an ultrahigh vacuum reaction chamber. One of the electrodes is connected to an RF power supply, while the other one is grounded. The precursor gases are introduced in the deposition chamber through a perforated metal electrode, called showerhead electrode. The reactant gases will get ionized creating a plasma; there, chemical reactions will take place resulting in the deposition of the reaction products on the substrate, which is grounded and kept heated typically at around 200-300°C [29]. Both deposition rate and optical properties of the layers, e.g. refractive index and absorptivity, can be controlled by acting on several parameters, such as RF power, substrate temperature, background pressure and gas flows [29]. A schematic of the PECVD process chamber is shown in figure 5.6.

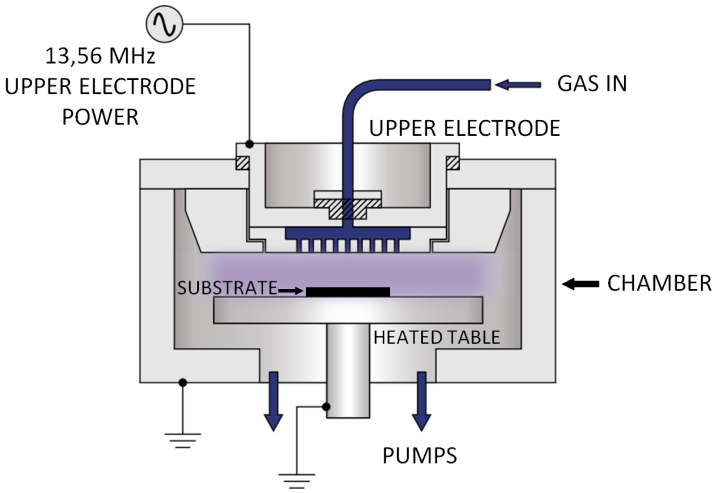

Figure 5.6: Schematic overview of the PECVD deposition chamber. Adapted from [55].

For the deposition of the colored interference layers, the PECVD machine PlasmaLab 80 Plus, by Oxford Instruments, located in the Kavli laboratory at TU Delft University has been used [56]. The reason why this PECVD tool has been chosen over the one present at the EKL cleanroom (so-called AMIGO tool, by Electrorava) is the bigger size of the electrode. With an electrode diameter of 24 cm, the PlasmaLab machine allowed us to achieve very high deposition homogeneity on the used 10 x 10 cm^2 Corning glasses (Eagle XG), contrarily to what obtained with the EKL machine.

The various filers have been fabricated by running automatic recipes, in which the total number of layers was specified and the time of the layers deposition was chosen depending on the desired thickness (i.e. the desired color).

5.2.5. Spectrophotometer

The optical characterization of the interference filters and the full colored mini-modules was performed with a spectrophotomer, a tool that allows to measure transmittance and reflectance of the samples as a function of the light wavelength. In a spectrophotometer, the light emitted by a specific light source is directed through a series of mirrors and optical filters towards a diffraction grating. The rotation of the grating allows to select the desired portion of the spectrum and reflect it onto an exit slit, which restrict the spectrum to a near-monochromatic beam [57]. The beam is then directed towards the sample and light reflected or transmitted by the sample is captured by an optical detector. The resulting measured spectra are compared, at each wavelength, to reference reflectance or transmittance spectra, and the final information is given terms of percentages [29].

In this work, a Lambda 950 spectrophotometer by Perkin Elmer was used [58]. The machine is equipped with two light sources, a deuterium arc lamp (for ultraviolet light) and a tungsten-halogen lamp (for near infrared and visible light), that are able to cover a wavelength spectrum between 175 and 3300 nm [29]. As shown in figure 5.7, two distinct accessories can be mounted on the spectrophotometer: an Integrating Sphere (IS) by Perkin Elmer and an Absolute directional Reflectance/Transmittance Accessory (ARTA) by OMT Solutions B.V. [59]. Both instruments are equipped with two detectors: a lead sulfide (PbS) detector (for NIR) and a photomultiplier tube (for UV/Vis) [29], [57]. The switch between the detectors takes place at 860,60 nm, which is also the weakest point of both detectors [29].

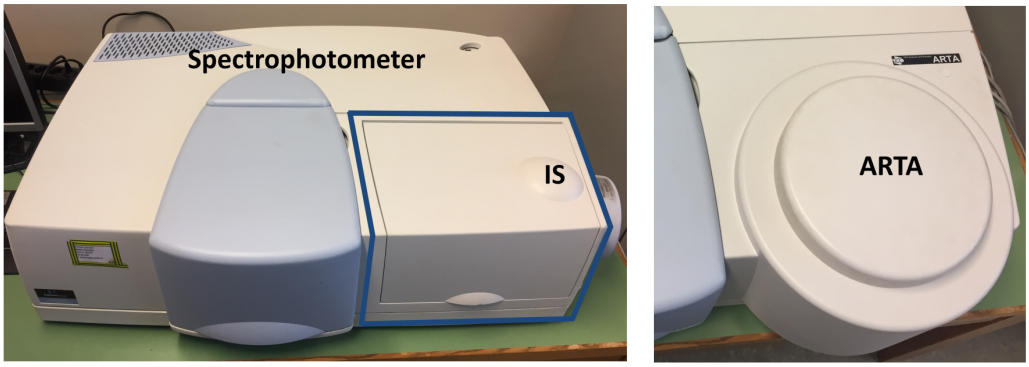

(a) **(b)**

Figure 5.7: Spectrophotometer Perkin Elmer Lambda 950 combined with IS **(a)** and ARTA **(b)** accessories. Photos courtesy of Thomas Loef [60].

Integrating Sphere (IS)

The integrating sphere has a 150 mm diameter and its internal wall is entirely covered with a highly reflective material, called Spectralon. This material has a Lambertian behaviour, meaning that it is able to scatter light in all directions obeying the cosine law (i.e. light intensity is proportional to the cosine of the scattering angle). The conceptual functioning of the integrating sphere is schematically shown in figure 5.8a. Depending on the measurement needed, the sample can be placed at the transmittance or reflectance port. When the sample is at the transmittance port, total transmittance measurements can be taken by closing the the reflectance port is with a small Spectralon disk. In this way, all the light that passes through the sample is continuously reflected and homogeneously diffused, and total transmittance T_T can be detected. If one is interested only in diffuse transmittance T_D, the Spectralon disk can be removed from the reflectance port, making the specular component leave the sphere.

Similarly, measurements of total and diffuse reflectance (R_T and R_D, respectively) can be performed by placing the sample at the reflectance port. As visible from the sketch, the sample at

the reflectance port is mounted with a tilt of 8°. In this way, the specular component can be excluded when the corresponding removable part of the sphere is taken out. Once total reflectance and transmittance are known, the absorptance of the sample can be simply calculated as $A_{sample} = 1 - R_T - T_T$.

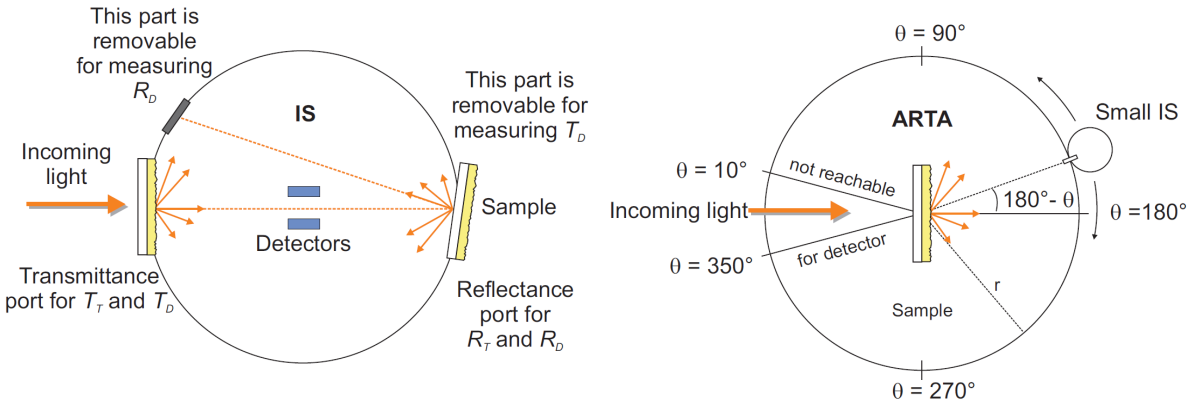

Figure 5.8: Sketched working principle of IS **(a)** and ARTA **(b)** accessories for the Perkin Elmer Lambda 950 spectophotometer. Adapted from [29].

Absolute directional Reflectance/Transmittance Accessory (ARTA)

ARTA is a fully automated spectral goniometer tool that uses a small integrating sphere (60 mm) as detector to measure directional (specular) reflectance and transmittance [59]. The goniometer in the middle can rotate the sample with respect to the light beam (varying angle of incidence) and independently rotate the integrating sphere detector with respect to the sample (varying angle of observation). Angles of incidence can vary between 0° (normal) and 85° (parallel) in transmittance and between 10° and 85° in reflectance [59]. Specular reflectance at normal incidence (0°) cannot be measured since the detector cannot physically get closer than 10° to the light source. For any incidence/observation angle pair, light spectra in the wavelength range 250-2500 nm can be collected [61]. The internal walls of the ARTA drum are black to avoid stray-light. A schematic of the ARTA setup can be seen in figure 5.8b. The rotation of the detector and sample holder can be controlled with the UV Winlab software so that the user can specify a run table that will be automatically executed. The ARTA tool is meant to provide indication on the intensity of the scattered light, known as angular intensity distribution AID, but the measurement results are given in terms of absorptance A. The measured A, function of wavelength and scattering angle, is related to AID via:

$$AID(\lambda,\theta) = 10^{-A(\lambda,\theta)}. \tag{5.1}$$

5.3. Colored mini-module demonstrators

Following the fabrication steps described throughout the chapter, one reference mini-module and five colored mini-modules have been manufactured. In the reference module, shown in figure 5.9, a normal glass without IF has been used as front cover. This will be taken as the reference to compare and evaluate the performance of the colored modules, especially in terms of electrical output.

Figure 5.9: Reference mini-module (no IF).

According to the availability of the the glass substrates and the fabrication machines, it was possible to deposit 5 interference filters, which have been used to laminate the 5 colored mini-modules shown in figure 5.10. For the sake of clarity, from now on the modules will be referred to using the labels shown in the figure 5.10 and described below:

- **Flat Orange**: flat glass - IF on flat side - orange color;
- **Random Text Purple**: randomly textured glass - IF on textured side - purple color;
- **Grooves Flat Green**: hemispherical grooved glass - IF on flat side - green color;
- **Grooves Text Green**: hemispherical grooved glass - IF on textured side - green color;
- **Grooves Flat Gold**: hemispherical grooved glass - IF on textured side - gold color.

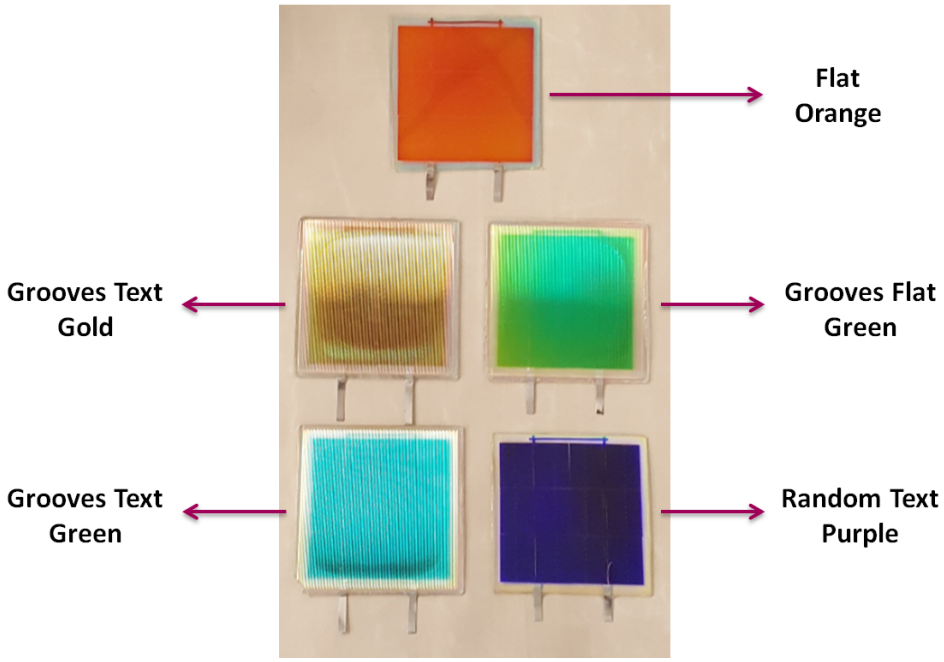

Figure 5.10: Fabricated colored mini-modules.

As can be seen from the picture, the fabrication was successfully performed and the interference filters conferred bright colors to the mini-modules. It can be noticed that the demonstrators differ from one another not only for the color (due to different layers thicknesses and number of pairs) but also for the type of glass used. In fact, according to the findings presented in the previous chapter about the impact of the surface morphology on the optical behaviour of the filters, different types of glass surfaces have been investigated. In particular, the three glass types shown in figure 5.11 were employed: *flat*, *randomly textured* and *hemispherical grooved*.

The first one is an untreated Corning glass of 700 μm, flat on both sides. The second one is a 700 μm thick Corning glass in which one side has been kept flat and the other one has been randomly textured via wet-etching[1]; the size of the craters are in the order of 1 to 5 μm [60]. The third type is a 2 mm thick glass which has a flat side and a grooved side, where the macroscopic grooves have hemispherical shape with a radius of around 500 μm.

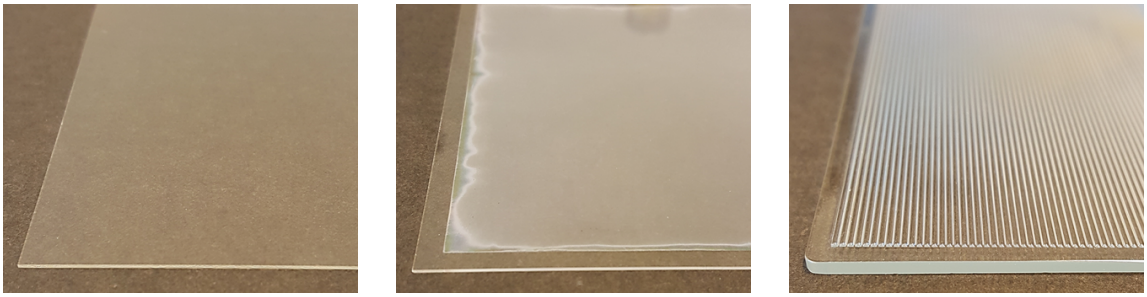

(a) Flat glass. **(b)** Randomly textured glass. **(c)** Hemispherical grooved glass.

Figure 5.11: Three types of glasses used for the colored mini-modules fabrication.

5.4. Optical characterization

In this section, each colored mini-module will be described and optically analyzed. The optical characterization, which has been performed via spectrophotometry, will be compared to the expected simulated filters behaviour, with the goal of validating the optical model. In the first part, the case of normal incident light will be analyzed; secondly, we will characterize the filters under different angles of incidence and/or observation.

5.4.1. Normal incidence

Here, the colored-mini modules will be singularly analyzed assuming light coming from the normal direction. The results will be provided in terms of *normal hemispherical reflectance*, where the term *normal* is referred to the direction of the incoming light, while *hemispherical* is referred to the reflected light, meaning that the total reflection (light in all directions) is considered. For simplicity, we will also refer to it as *total reflectance*. It is reminded that the IS sphere allows to measure at an angle of 8°, which we can approximate to 0° without losing accuracy.

Flat Orange

The structure of the filter used for the *Flat Orange* mini-module is illustrated in figure 5.12. The other layers forming the module, i.e. EVA, solar cell and back glass, have been omitted for simplicity since they are the same for all the five mini-modules. For the full module structure, the reader can refer to figures 4.19 and 5.1b.

[1] The randomly textured glass has been fabricated in the EKL laboratory by T. Loef, a former MSc student. More information on the features and realization steps can be found in [60].

The filter is deposited on a flat glass and it is made of 20 layers of alternating SiO_2 and SiN_x with thicknesses 100 nm and 90 nm, respectively. The color corresponding to this thicknesses combination is the orange shown in the figure.

The measured and simulated total reflectance at normal incidence are plotted as function of wavelength in figure 5.13. As shown, there is a good match between the simulated and measured curves, proving the validity of the optical model for flat configurations. The high number of layers used for this flat configuration resulted in a very high reflectance peak of more than 95%, occurring at λ=655 nm, which is translated in a very bright orange color. It can be observed that also the width of high reflectance, which is mainly affected by the difference between the refractive indices of the dielectric materials, is rather large.

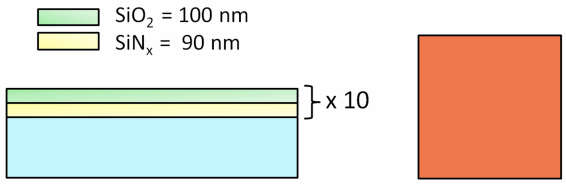

Figure 5.12: Filter structure and corresponding color of *Flat Orange* mini-module.

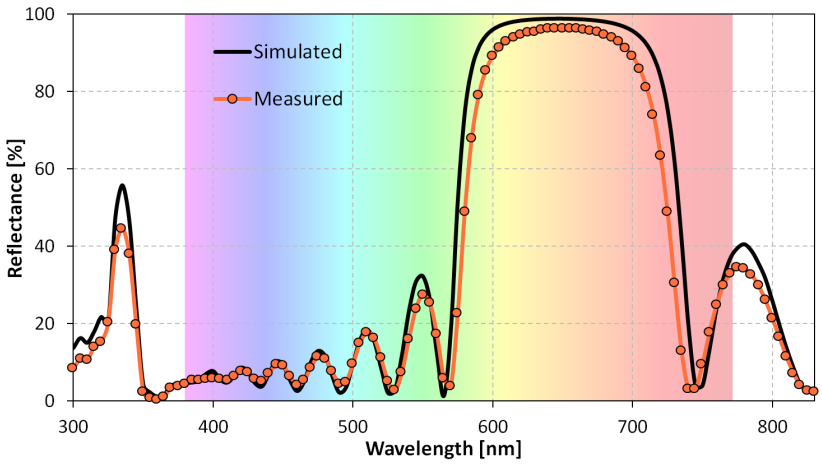

Figure 5.13: Measured and simulated total reflectance of *Flat Orange* mini-module.

Random Text Purple

For this mini-module, a 20-layer filter has been deposited on top of the randomly textured glass presented in the previous section, resulting in a purple color, as shown in figure 5.14.
In the recipe fed into the PECVD machine for the filter deposition, the thicknesses of SiO_2 and SiN_x were set at 84 and 168 nm, respectively. However, with this thickness combination, the simulated reflectance curve was found to be shifted with respect to the measured one. Therefore, by changing thicknesses combination in the optical model, the measured curve was fit (dashed line). The better agreement given by the fitted curve corresponds to smaller thicknesses, precisely SiO_2=76 nm and SiN_x=156 nm.

The disagreement is due to the non-flatness of the surface and can be possibly explained by two main reasons. First of all, with non-flat surfaces, the thicknesses of the individual layers in the preferential growth direction (Y-direction, see figure 5.16) is different from the thickness in the direction orthogonal to the facet of the texture feature (X-direction) [62]. Since in the used ray-racing software the filter is considered as a coating and thus is conformal to the texture shape, with

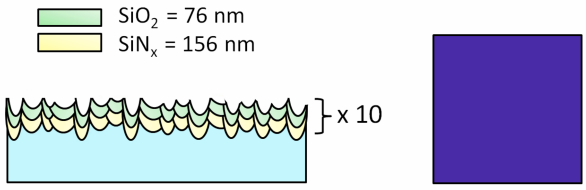

Figure 5.14: Filter structure and corresponding color of *Random Text Purple* mini-module.

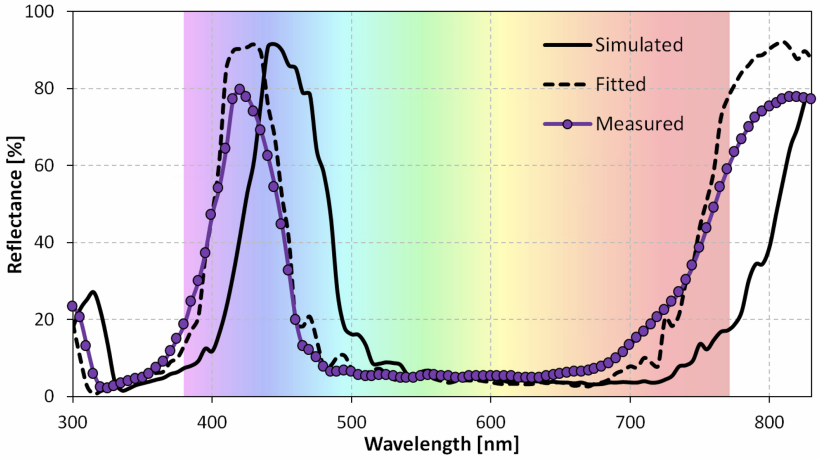

Figure 5.15: Measured, simulated and fitted total reflectance of *Random Text Purple* mini-module.

the PECVD deposition we need to obtain the designed thickness in the orthogonal direction (X). Therefore, the deposition time should be corrected with a scaling factor. For linear shapes, such as the pyramids obtained with cell alkaline texturing, this factor can be approximated to sin(90-θ) where θ is the etching angle [62].

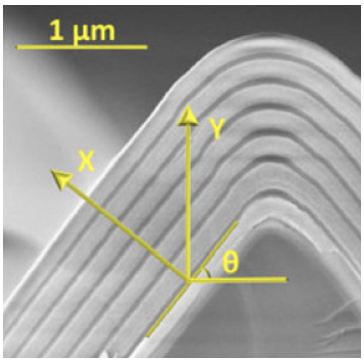

Figure 5.16: Cross-sectional SEM of a multilayer filter deposited via PECVD. X- and Y-axis indicate the directions orthogonal to the pyramid facet and parallel to the deposition growth, respectively. Adapted from [62].

The complication arises when, as in our case, the texture features have rounded shapes and different aspect ratios. In this case, it would be difficult to determine a correction factor for the deposition time, because the tangent angle θ would be different at any point of the curved shape. Additionally, it might happen that the thickness of the deposited layers is not constant along the feature shape, leading to high non-uniformity. If this is the case, it would be hardly possible to model the real structure with the optical ray tracing model.

Grooves Flat Green

The *Grooves Flat Green* mini-module has been obtained by using the hemispherical grooved glass, but the filter deposition was performed on the flat side of the glass. The filter structure and the corresponding color are shown in figure 5.17. In this case, only 6 pairs, i.e. 12 total layers, of alternating SiO_2 and SiN_x were used, with thicknesses of 60 and 90 nm, respectively.

The measured and simulated total reflectance at normal incidence are shown in figure 5.13. As for the case of the orange flat filter, there is a good match between the simulated and measured curves. In this case, however, we can noticed a reduced reflectance peak. The lower reflection is attributed to both the smaller number of layers used and, mostly, to the texturing on the external side of the glass.

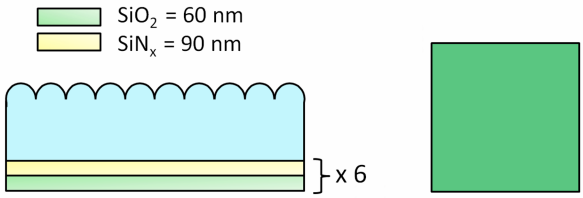

Figure 5.17: Filter structure and corresponding color of *Grooves Flat Green* mini-module.

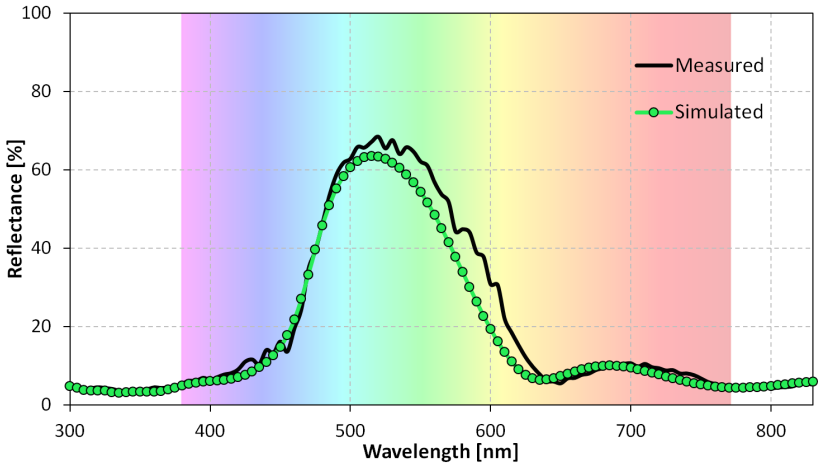

Figure 5.18: Measured and simulated total reflectance of *Grooves Flat Green* mini-module.

Grooves Text Green

The *Grooves Text Green* filter has a similar structure as the previously described *Grooves Flat Green*, but this time the 12-layer filter has been deposited on the textured side of the grooved textured glass. The thicknesses of SiO_2 and SiN_x layers were kept again at 100 nm and 90 nm, respectively. Filter structure and corresponding color can be seen in figure 5.19, while the reflectance curves are shown in figure 5.20.

It can be observed that the measured reflectance differs quite significantly form simulation carried out with the above mentioned filter configuration. Therefore, we tried to fit the measured curve by varying the thicknesses and number of layers in our optical model. It was found that the best fit is obtained with 6 layers (3 pairs) of SiO_2=48 nm and SiN_x=72 nm. The fact that the real obtained thicknesses may differ from the desired ones has already been discussed and it could be understandable due to the non-flatness of the surface we are considering. However, the reduced number of layers (half of the actual number of layers deposited) of the fitting configuration is debatable. This led us

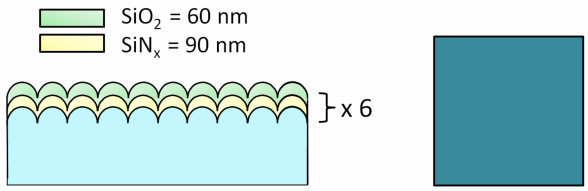

Figure 5.19: Filter structure and corresponding color of *Grooves Text Green* mini-module.

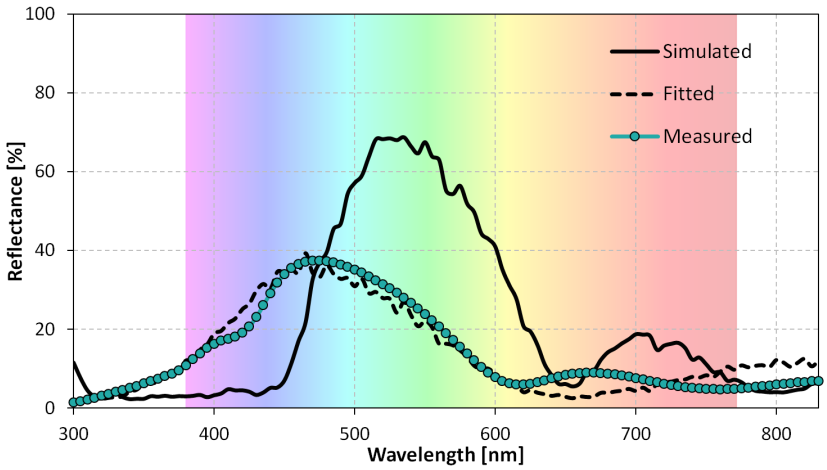

Figure 5.20: Measured, simulated and fitted total reflectance of *Grooves Text Green* mini-module.

to believe that for this kind of glass, where the texture feature size is in the order of 500-1000 μm, the uniformity of the deposited layers is completely compromised. What might have happened is shown in the schematic of figure 5.21: a non-uniform layer growth resulting in a thickness gradient (image on the left). This is due to the fact that the surface of a convex hemisphere that is normal to the deposition flux receives a higher amount of material than the edges [63]. In the figure, the ideal case of uniform deposition (on the right) is also shown for comparison. This problem can be linked to the macroscopic feature size of our glass and/or the deposition process used (PECVD). It was found in literature that other deposition techniques, such as ALD (atomic layer deposition), can provide better thickness uniformity [63] [64].

Since the required film thickness might not be met over the entire surface of the convex hemispheres, the resulting reflectance spectra could be distorted. In this situation, the simulated fitting curve found to match the measured reflectance cannot be fully and precisely representative of the real filter configuration and it should be taken just as a reference.

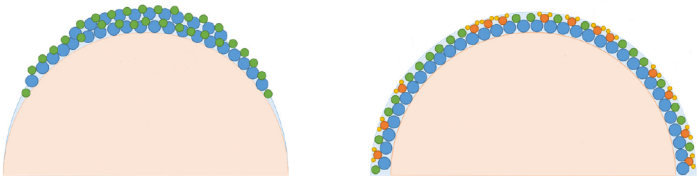

Figure 5.21: Thickness gradient formation on hemispherical shapes due to non-uniform film growth (left) vs. ideal uniform layer deposition (right). Adapted from [63].

Grooves Text Gold

Similarly to the previous case, the *Grooves Text Gold* mini-module has been fabricated using the hemispherical grooved glass. The filter is made of 20 layers of 90 nm SiO_2 and 100 nm SiN_x, deposited on the textured side of the glass. As shown in figure 5.22, the color corresponding to this filter configuration is a gold.

According to the previous case, the reflectance curve of the measured mini-module and the simulation result differ significantly from each other: the measured reflectance peak is around half the simulated one and it is shifted towards lower wavelengths. The situation is analogue to the previous case, and so are the reasons behind this inaccuracy. The fitted curve visible in the plot of figure 5.22 is obtain for a 6-layer filter of thicknesses SiO_2=72 nm and SiN_x=82 nm. As already emphasized, this configuration is anyway far from the real filter structure characterized by layer thickness non-uniformity along the texture features.

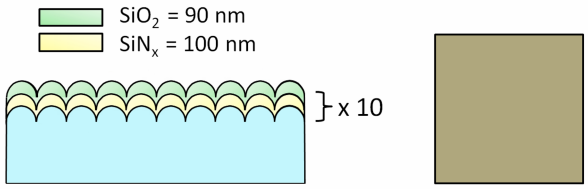

Figure 5.22: Filter structure and corresponding color of *Grooves Text Gold* mini-module.

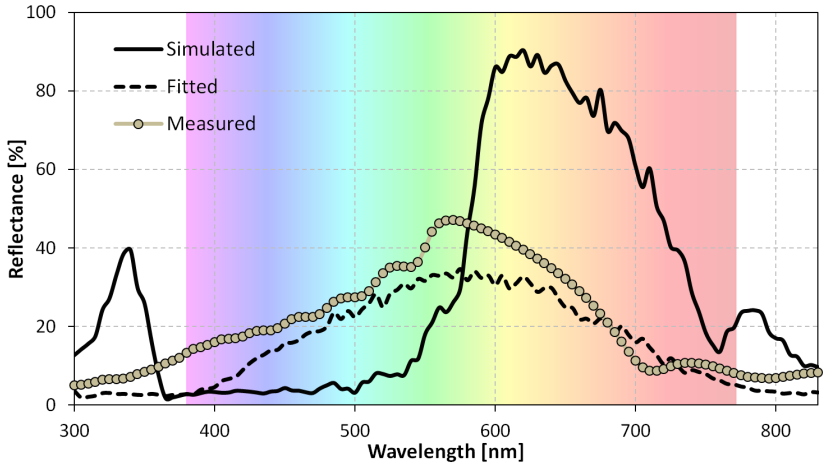

Figure 5.23: Measured, simulated and fitted total reflectance of *Grooves Text Gold* mini-module.

5.4.2. Angular behaviour

In order to have a better understanding of the angular behaviour of the mini-modules, the optical properties of the three types of glass have been analyzed; the analysis was done before depositing the filter, in order to focus only on the effect of the surface texturing.

Total and diffuse reflectance and transmittance were measured for each sample. The average total reflection in the wavelength range of interest was found to be between 6% and 8% for all the cases. More interesting is to check how this total reflectance is shared among the direct and diffuse component, i.e. how well the surface scatters the reflected light. This information can be obtained by calculating the haze H_R of the samples according to the following formula:

$$H_R(\lambda) = \frac{R_D(\lambda)}{R_T(\lambda)} \tag{5.2}$$

where R_D and R_T represent diffuse and total reflectance, respectively. The result is shown in figure 5.24. As clear from the plot, both the randomly etched glass and the hemispherical grooved glass are able to effectively scatter almost all the light they receive. As expected, reflection from the flat glass is entirely directional.

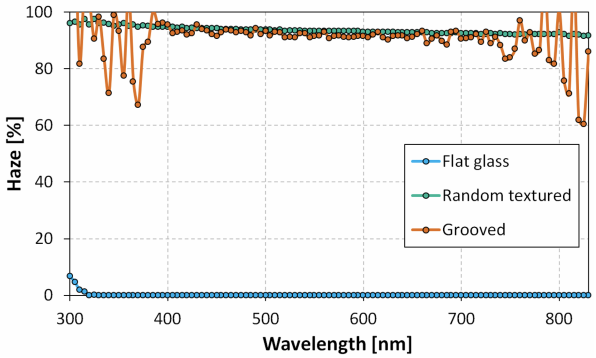

Figure 5.24: Haze of the three types of glass used: flat, randomly textured and grooved.

First, the five mini-module structures have been recreated in our optical model, and the angular performance of each sample has been simulated. The following figures show the color perception as function on varying angle of incidence and the reflectance spectra at 0°, 20°, 40°, 60° and 80°.

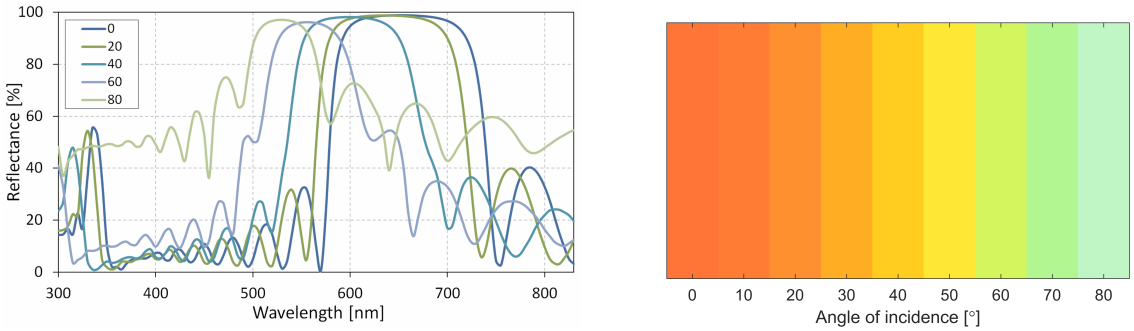

(a) **(b)**

Figure 5.25: *Flat Orange* module: simulated reflectance spectra **(a)** and color perception **(b)** for different angles of incidence.

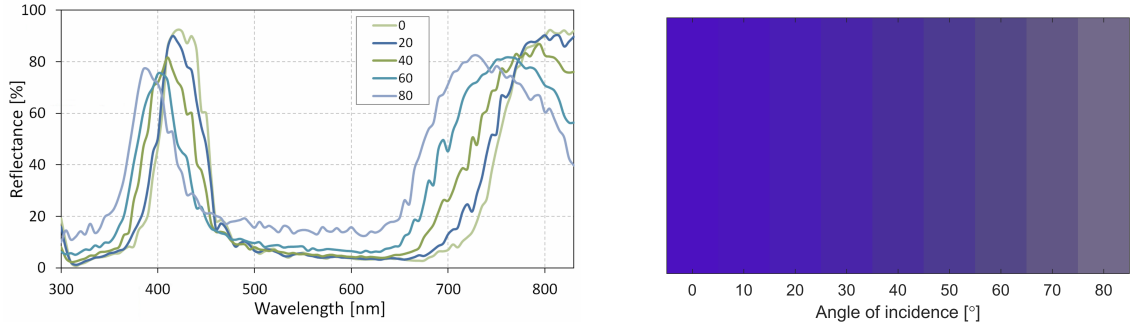

(a) **(b)**

Figure 5.26: *Random Text Purple* module: simulated reflectance spectra **(a)** and color perception **(b)** for different angles of incidence.

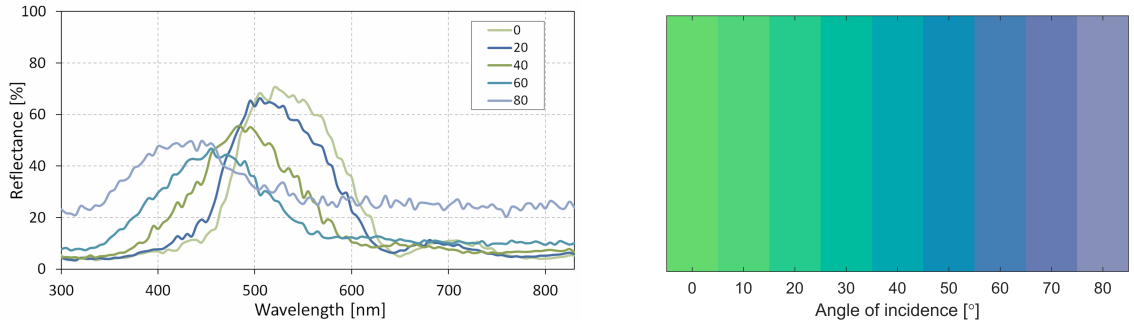

(a) **(b)**

Figure 5.27: *Grooves Flat Green* module: simulated reflectance spectra **(a)** and color perception **(b)** for different angles of incidence.

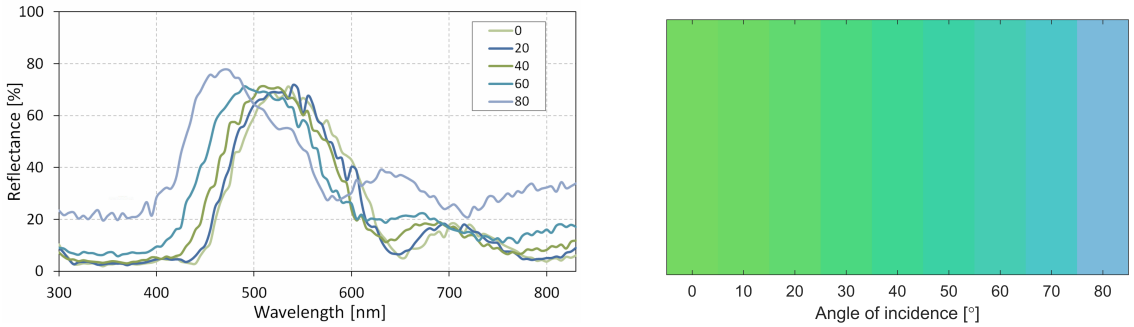

(a) **(b)**

Figure 5.28: *Grooves Text Green* module: simulated reflectance spectra **(a)** and color perception **(b)** for different angles of incidence.

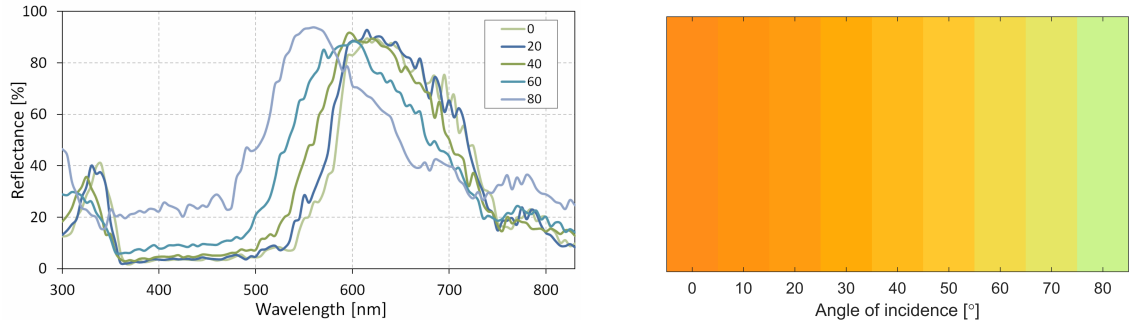

(a) **(b)**

Figure 5.29: *Grooves Gold Green* module: simulated reflectance spectra **(a)** and color perception **(b)** for different angles of incidence.

The simulation results show that when the filter is deposited on a flat surface (e.g. *Flat Orange* and *Grooves Flat Green*) the blue-shift of the reflectance spectra is quite significant, resulting in an evident change of color. On the other hand, when the filter is placed on the textured side of the glass higher color resilience can be obtained, result that is consistent with the findings of the previous chapter. In particular, it seems that the purple randomly textured mini-module is the sample that presents the best angular consistency. It must be observed that the hemispherical grooved glass

mini-modules have been simulated assuming the layer thicknesses of the original design (see figures 5.19 and 5.22) and not the fitted ones; although the color might appear different, the optical behaviour is similar.

The angular optical characterization of the realized mini-modules has been performed with the ARTA accessory of the spectrophotometer. By moving the sample and the detector position it was possible to control independently both the illuminating angle (AOI) and the observation angle. However, this characterization tool does not provide the results in terms of reflectance, but in terms of *angular intensity distribution* (AID). Because of this, it was not possible to make a proper comparison between simulated and measured values in absolute terms, but only compare the trends of the curves and the intensity peaks.

For the *Flat Orange* filter case, the angular measurements showed that only specular reflection is achieved. Fixing the illumination angle at 10° and changing the observation angle from 0° to 80°, the plot of figure 5.30 was obtained. It can be noticed that only the curve corresponding to $\theta_{obs} = 10°$ (equal and specular to $\theta_{ill} = 10°$) is detected, while for any other angle the spectophotometer registered only noise, meaning no reflection. The same result is achieved in the opposite condition: fixed observation and varying illumination angle. In fact, for flat and mirror-like surfaces, the appearance does not change when light source and viewing directions are swapped; this is also known as Helmholtz reciprocity principle [65].

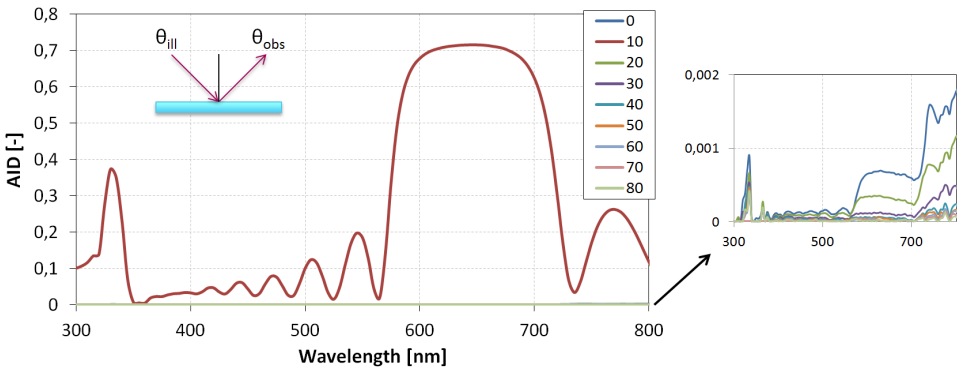

Figure 5.30: *Flat Orange* mini-module: AID for fixed illumination angle (10°) and varying observation angles (and viceversa) show only specular reflection.

When plotting the AID curves for each combination of specular angle of incidence and observation, the graph of figure 5.31a is obtained, clearly showing the expected blue-shift when the angle is increased. It is also shown that, when the angle of incidence/observation is increased, the amount of reflected light significantly reduces. However, it must be noticed that the AID is an adimensional quantity expressing the light intensity, and it should not be directly compared to the reflectance.

In order to make a more direct comparison and validate the optical model for non-normal angles of incidence, both measured AID and simulated reflectance have been normalized with respect to their maximum value. Figure 5.31b shows the result for three selected angles (10°, 30° and 50°). As visible, the simulated curves have in general slightly wider reflectance zones, but the trend and the shapes are clearly consistent with each other, thus proving the validity of the model. The reasons behind the small inaccuracy can be several. First of all, GenPro4 simulates the total hemispherical reflection (contributions of all directions), while the AID measurement is directional (detector placed in one specific point). Secondly, the exact thicknesses of the deposited filter layers may slightly differ from the ones input in the model, as well as the optical properties of the two materials (n and k values of SiO_2 and SiN_x). It was already proved in the optical analysis at normal incidence that, within a small error margin, the simulated curve slightly overestimated the measured one. The

ARTA analysis, therefore, seems to be in accordance with this result.

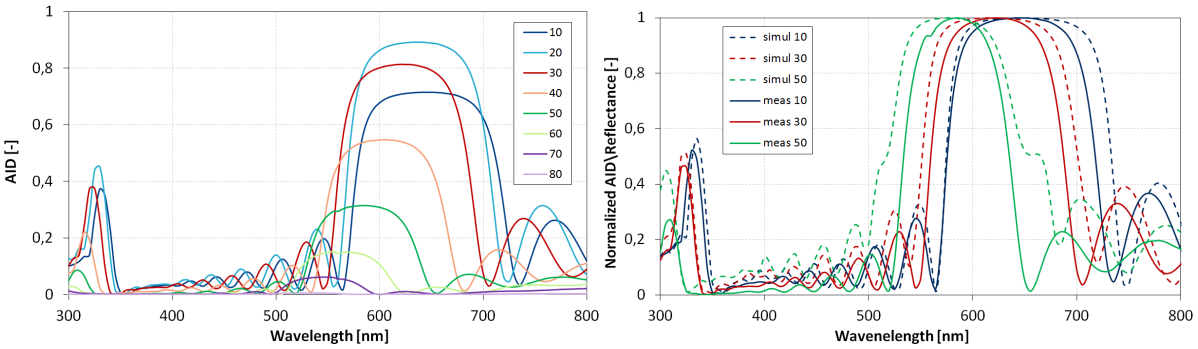

(a) **(b)**

Figure 5.31: *Flat Orange* mini-module: **(a)** AID for each combination of specular angle of incidence and observation; **(b)** Comparison between normalized measured AOI and simulated reflectance for different illumination angles (10°, 30° and 50°).

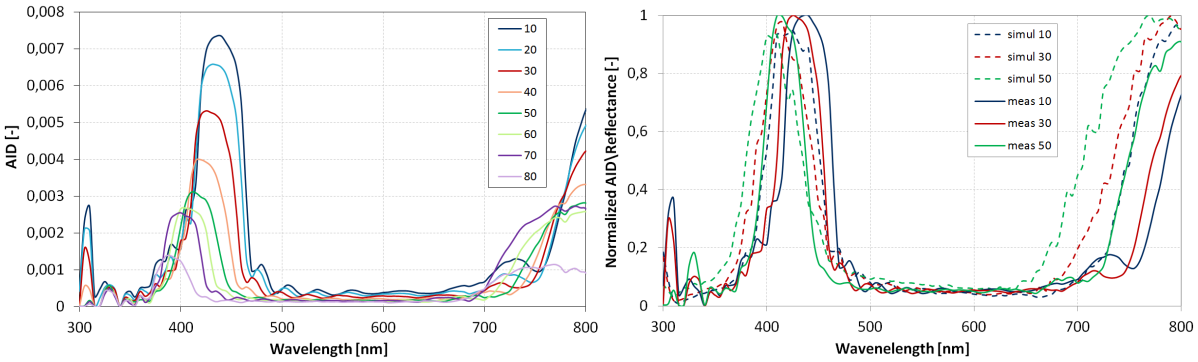

(a) **(b)**

Figure 5.32: *Random Text Purple* mini-module: **(a)** AID for fixed observation angle (0°) and varying illumination angles; **(b)** Comparison between normalized measured AOI and simulated reflectance for different illumination angles (10°, 30° and 50°).

The results for the *Random Text purple* mini-module are presented in figure 5.32. In this case we expect a different behaviour since the reflection coming out this type of glass was proven to be almost entirely diffusive (haze $H_R \approx 95\%$). Figure 5.32a shows the AID for a fixed observation angle of 0° and varying illumination angles. Differently from the flat case, where only the specular component was detected, here we can perceive reflected light from every angle, proving the diffusive nature of the textured surface. It can be noticed that the shift towards lower wavelengths is much more moderate and, as expected, as the angle increases the intensity decreases.

Again, by normalizing the simulated reflectance and the measured AID and comparing their trends, it is possible to validate the optical model. As shown in figure 5.32, the dashed lines indicating the simulated reflectance are very close to the corresponding measured AID curve for the three reference angles of 10°, 30° and 50°. The possible reasons for the inaccuracy are the same we discussed above, even tough, in this case, the uncertainty about the real thicknesses obtained via PECVD deposition has probably the strongest impact.

With regard to the remaining three mini-modules made with the hemispherical grooved glass, the angular reflectance analysis has been more problematic because of the peculiar feature of the

glass. In this case, a comparison between the measured AID and the simulated reflectance curves becomes meaningless since it was not possible to match the optical model with the real filter structure even at normal incidence. Therefore, for this surface structure, the optical model on the angular behaviour still requires validation. Nonetheless, it is possible to analyze the ARTA measurements in order to characterize the optical behaviour of this type of surface. We will consider only the *Grooves Text Gold* mini-module, as the others have a similar behaviour.

When the AID of the *Grooves Text Gold* sample is analyzed as function of the angle of incidence (moving illumination source and keeping fixed the observation angle), we see only the specular reflection. This is true for every angle at which the detector is placed. On the other hand, when the AID is analyzed as function of the observation angle (moving the detector and keeping fixed the illumination angle), we observe that for some specific directions (e.g. 10°, 30°, 50°, 70°) no light is detected. This might be due to the periodicity of the structure (grating-like profile) or related to the relatively large size (≈ 1 mm of diameter) of the hemispherical cylinders that characterize the grooved glass; in fact, the point where the light beam arrives might be seen as a locally flat surface.

This trend can be observed in the contour plot at the right-hand side of figure 5.33. The three graphs represent the specular light intensity, i.e. the AID values at combination of $\theta_{ill}/\theta_{obs}$ equal to 10°/10°, 20°/20°, 30°/30° and so on. The first (left), second (middle) and third (right) plots represent, respectively, the *Flat Orange*, *Random Text Purple* and *Grooves Text Gold* mini-modules. It is clear that the three glass structures present rather different behaviour. For the flat case, we can observe a more marked shift towards lower wavelengths than for the randomly textured glass. Indeed, the latter shows quite a consistent spectral behaviour in correspondence with the peak wavelength which is responsible for the color appearance (indicated by the dashed black line). As for the grooved glass, it can be seen that it exhibits the directional behaviour discussed above, for which no reflection is obtained for specific wavelengths. Finally, it can be observed that, for the flat case, the interference effect created by the filter almost disappears in the visible range for high angle of incidence/observation (above around 50°), while for the two textured glasses it is maintained up to almost 80°.

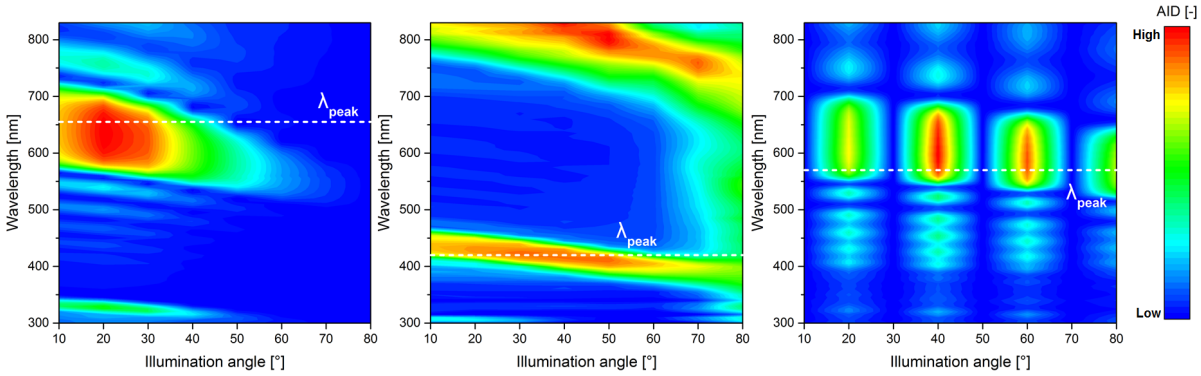

Figure 5.33: Contour plots of specular AID for *Flat Orange* (left), *Random Text Purple* (middle) and *Grooves Text Gold* (right) mini-modules. Each plot has been generated with its own color scale, but this has been omitted because the absolute values are irrelevant. Color bar on the right is only a legend to indicate low and high intensity values.

5.5. Conclusion

The present chapter focused on the fabrication and optical characterization of colored mini-modules. The workflow needed for the modules manufacturing process was explained and it was shown how the realized demonstrators could validate the optical model.

The designed mini-modules were made of 6 small cut solar cells connected in series and encap-

sulated in 10 x 10 cm^2 glasses on both front and rear side, with EVA as encapsulating material. To obtain such module design, three main fabricating steps have been followed: (1) cutting, (2) soldering and (3) lamination. Additionally, a PECVD process was performed on glass substrates in order to provide color to the external glass of the PV module. The fabrication steps and the experimental setups have been thoroughly described in the second section of the chapter.

Following the fabrication workflow it was possible to successfully build 5 colored mini-modules, identified as: *Flat Orange*, *Random Text Purple*, *Grooves Flat Green*, *Grooves Text Green* and *Grooves Text Gold*. The five demonstrators differ from one another not only for the color, due to different layers' number and thicknesses, but also for the type of glass used. Three different types of glass were investigated: a flat, a randomly textured and a hemispherical grooved glass.

The last section of the chapter dealt with the optical characterization of the mini-modules, which was performed via spectrophotometry. At first, the samples were analyzed at normal incident. Measured and simulated total reflectance curves were compared, with the aim of validating the optical model. It was found that when the filters are deposited on the flat glass or on the flat side of the grooved glass, a good agreement between measurements and simulations is obtained. On the other hand, when the filter is deposited on textured surfaces, especially on the large features of the grooved glass, the model is not able to simulate the real fabricated structure. One of the reasons might be that the ray-tracing software does not reproduce periodic structures in an optimal way. Another explanation is given by the probable non-uniformity of the PECVD layer growth on the feature of the highly textured glass, which has likely generated a thickness gradient along the feature shape.

With respect to the angular optical behaviour, first the simulation results were presented and then the measurements of the demonstrators were analyzed. According to the simulation results, the randomly textured glass presented the best angular resilience, but good color consistency was obtained also for the grooved glass. The actual angular characterization of the mini-module was performed with the ARTA accessory of the spectrophotometer, which provides results in terms of AID (angular intensity distribution). The analysis showed that the flat glass is only able to reflect light specularly, thus confirming its strong angular dependence. On the other hand, it was proven that for the randomly textured glass the blue-shift phenomenon is significantly reduced thanks to the diffusive nature of the reflection associated with the texturing. For the grooved glass the optical behaviour seemed to resemble that of a flat surface, since it presents directional reflectance, and only at specific angles. This might be due to the extremely large size of the hemispherical grooves and the periodicity of the structure. For this type of surface it was not possible to validate the optical model and provide a full explanation of the optical behaviour, which is indeed left as recommendation for future work. However, it is recalled that the most angular resilient structures discussed in chapter 4 were designed with hemispherical shaped grooves with diameter of around 3 μm, which is much smaller than the 1 mm -diameter grooves of the glass we used.

All in all, it can be concluded that colored mini-module could be successfully fabricated and that the optical model for flat configurations and small-feature texturing surfaces (in the order of few microns) has been validated with acceptable error margins.

6

Electrical performance assessment

So far, it was shown how colored mini-modules made with interference filters (IF) can be successfully fabricated and which is their optical behaviour. The optical simulations also proved that the angular dependence of the filter's color can be significantly reduced using optimal surface geometries. All in all, it was demonstrated that interference filters are effectively able to provide colors to PV modules, thus expanding the aesthetic flexibility of this technology. But, to what extent the improved aesthetics affects the energetic performance of a PV device? It must not be forgotten that our intent is trying to provide aesthetical appeal to an energy technology that has the primary goal of generating sustainable electricity. Therefore, the assessment of the colored modules in terms of electrical output is extremely important and required for a final and complete evaluation. This aspect will be the focus of the present chapter, which aims to answer the third and last research question of the this work:

What is the electrical performance of the colored mini-modules made with interference filters?

The first section will deal with the description of the used characterization tools: solar simulators for current-voltage (I-V) measurements and an electroluminescence setup for the detection of potential fabrication problems. Then, the results of the electrical assessment of the five colored mini-modules will be presented, both in terms of measured I-V curves and modelled EQE (External Quantum Efficiency) and J_{ph} (photogenerated current). The chapter will end with the analysis of cell-to-module (CTM) losses related to our in-house PV modules fabrication process.

6.1. Characterization tools

6.1.1. Solar simulators: LASS and WACOM

A Large Area Solar Simulator (LASS) produced by Eternal Sun [66] was used to measure the I-V curves of the mini-modules under Standard Test Conditions (STC)[1]. The machine, shown in figure 6.1 is able to produce continuous artificial light, by using halogen and gas lamps, that approximates the solar spectrum AM1,5 with very good precision. The used LASS is classified as an AAA-class solar simulator, meaning that it has the highest rating on the three following aspects: (1) spectral match with respect to the solar spectrum; (2) irradiance spatial uniformity; (3) light intensity stability over time [66].

The module to be tested can be placed on the so-called *module table*, that allows to quickly move the module underneath the LASS and remove it after the measurement. On the *module table* there is also a mono-crystalline silicon reference cell used for calibrating the irradiance value before the

[1] STC: irradiance of 1000 W/m^2, temperature of 25°C and solar spectrum AM1,5.

measurements. The simulator is equipped with an electronic load (from B&K Precision) and a digital multi-meter (from Agilent Technologies). The load allows to sweep the I-V curve, while the multi-meter is necessary for recording both output current and voltage. These devices are connected to a computer screen, which is used to control the load and read the measurements through the software *ReRa Tracer 3*.

Figure 6.1: Large Area Solar Simulator (LASS). Adapted from [66].

The measured I-V curves allow to determine the main electrical performance parameters of the PV modules: open circuit voltage (V_{oc}), short circuit current (I_{sc}), fill factor (FF), maximum power (P_{mpp}), voltage at the maximum power point (V_{mpp}), current at the maximum power point (I_{mpp}) and conversion efficiency (η).

To calculate the cell-to-module losses, the continuous solar simulator Wacom WXS-156S, class AAA, was used [67]. Differently from the LASS, this solar simulators allows to measure the I-V characteristic of single solar cells, also before interconnecting and laminating them. It consists of a xenon lamp and a halogen lamp that closely reproduce the spectrum and the intensity of actual sunlight, with an illumination area of 156 x 156 mm^2. I-V measurements are taken at STC temperature, since the chuck can also be thermally controlled.

6.1.2. Electroluminescence (EL) setup

With the goal of detecting possible cell defects or module manufacturing problems, electroluminescence (EL) photos have been taken. Electroluminescence is an opto-electrical phenomenon which consists in applying a direct current to the module and measuring the photoemission by using an infrared camera. The emission of light takes place because of the radiative recombination of holes and electrons when they undergo a forward bias [68]. The wavelength of the emitted light corresponds to the bandgap of the semiconductor material; silicon solar cells emit infrared light with wavelengths around 1000 to 1200 nm [69]. Therefore, to detect this light, an infrared-sensitive camera is needed.

The intensity of the photoemission is correlated to the open circuit voltage, the series resistance, the minority carrier diffusion length, as well as the ideality factor and quantum efficiency of the cell [68]. This means that EL is an effective technique to detect defects and assess the status of the solar cells forming a module. Moreover, it has the advantages of being non-destructive and relatively fast [69].

In the EL setup of the TU Delft PV Lab, a Maisheng DC power supply is used to feed current into the module. The infrared camera is placed in front of the module and, at the moment of the photo shoot, they have to be in a completely dark environment. Attention should be paid when using the power supply: exceeding the rated power output of the module will damage it.

6.2. Electrical performance of fabricated colored mini-modules

6.2.1. Measured I-V curves

The electrical performances of the reference mini-module (without filter) and the five colored ones have been measured using the LASS. The obtained I-V curves are shown in figure 6.2, where in each plot a colored module is compared to the reference.

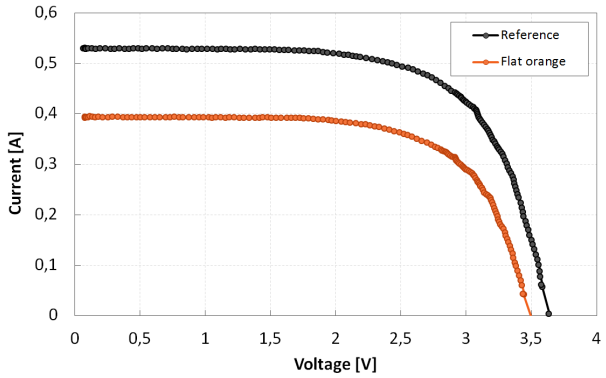

(a) Flat Orange.

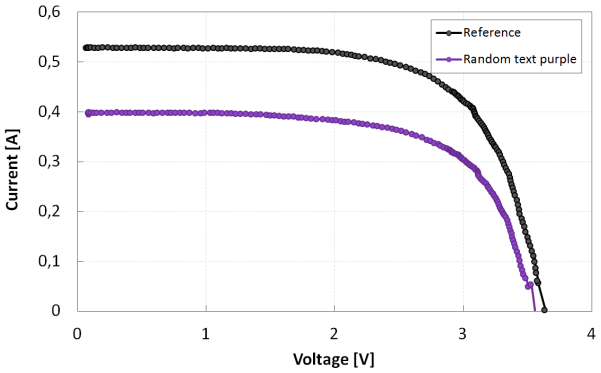

(b) Random Text Purple.

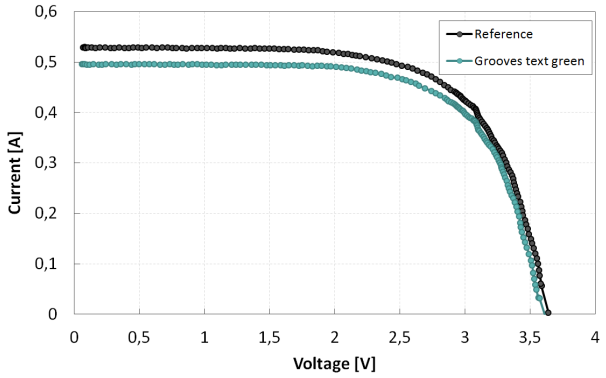

(c) Grooves Text Green.

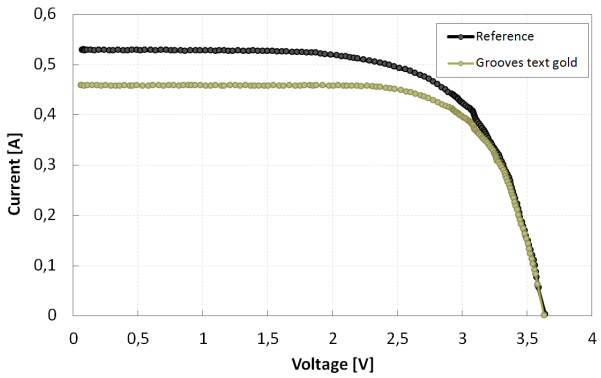

(d) Grooves Text Gold.

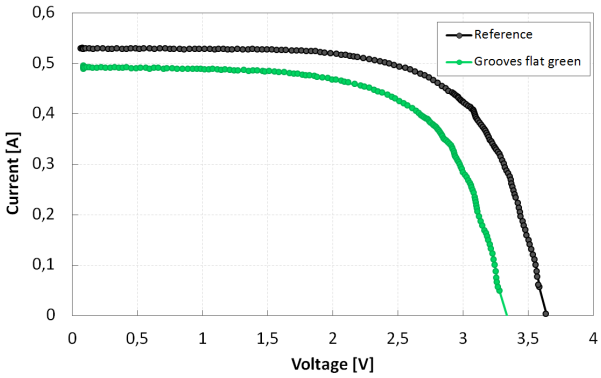

(e) Grooves Flat Green.

Figure 6.2: Measured I-V curves of the five colored mini-modules compared to the reference one (without filter).

From the I-V curves, the relevant module parameters have been extracted and are summarized in table 6.1. The conversion efficiencies of the mini-modules are also shown in the barplot of figure 6.3. They have been calculated considering only the effective area covered by the solar cells (i.e. excluding borders and space in-between the cells).

Table 6.1: Mini-modules electrical parameters.

	$\mathbf{I_{sc}}$ [A]	$\mathbf{V_{oc}}$ [V]	$\mathbf{P_{mpp}}$ [W]	**FF** [%]	η [%]
Reference	0,53	3,64	1,29	67,24	16,23
Flat Orange	0,39	3,50	0,92	67,10	11,59
Random Text Purple	0,40	3,56	0,94	66,32	11,80
Grooves Text Green	0,50	3,61	1,22	68,06	15,28
Grooves Text Gold	0,46	3,63	1,20	72,25	15,09
Grooves Flat Green	0,49	3,34	1,07	65,68	13,45

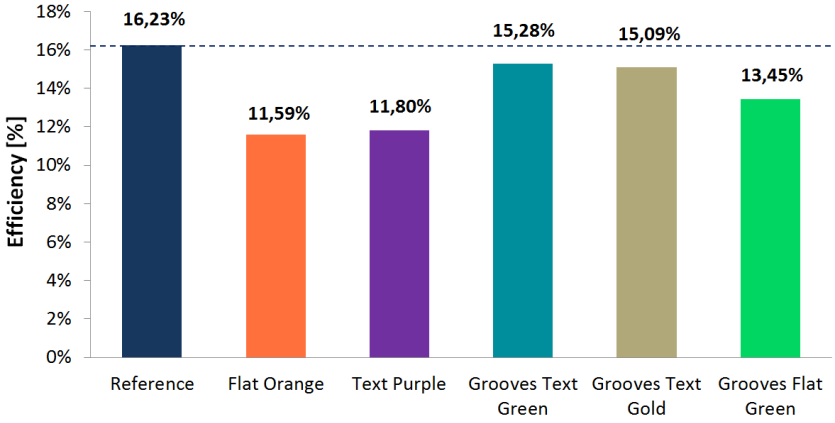

Figure 6.3: Conversion efficiencies of the fabricated mini-modules.

It can be observed that the interference filter affects the module performance mainly in terms of J_{sc} reduction. The worst performing module is the *Flat Orange* one, which reports an efficiency of 11,59%, indicating a reduction of 4,64% absolute (and around 28% relative) with respect to the reference module. In this filter, the strong reduction in the J_{sc} value must be attributed to the very wide reflectance peak that characterizes this filter. In fact, the peak of reflectance caused by the interference effect reduces the amount of light transmitted to the cell, hence reducing the photo-generated current and the J_{sc}. In general, the higher and wider the reflectance peak, the higher the losses. Additionally, the surface flatness of the glass does not provide any anti-reflective effect, thus not enhancing the light in-coupling.

In this respect, it would be expected that the randomly textured glass (*Random Text Purple*) would show a better performance. However, also in this case, the efficiency dropped of more than 4% absolute. To understand the reason behind this, several aspects should be considered. For example, it is important to take into account at which wavelength the IF high reflectance peak occurs in relation to the the spectral response of the silicon cell and the AM1,5 solar spectrum intensity. The module reflectance spectrum measured for the whole interested wavelength range (300-1200 nm) is illustrated in figure 6.4a; it can be seen that apart from the known peak at violet-blue wavelength, the filter peaks also at around 850 nm. As visible in figure 6.4b, this second IF peak is close to the point where the spectral response of the silicon cell is higher (around 1000 nm), meaning that we are reflecting back almost 80% of the light that should be converted into current in the most effective way. On the other hand, the first reflectance peak that occurs at around 420 nm is close to the wavelengths for which the solar spectral irradiance has its stronger intensity (around 500 nm, as shown in figure 6.4c).

The above mentioned aspects explain only partially the relatively low current of the purple textured module. Another reason can be found when analyzing the state of the module through electroluminescence imaging. The EL photos of each mini-module are shown in figure 6.5. Looking at

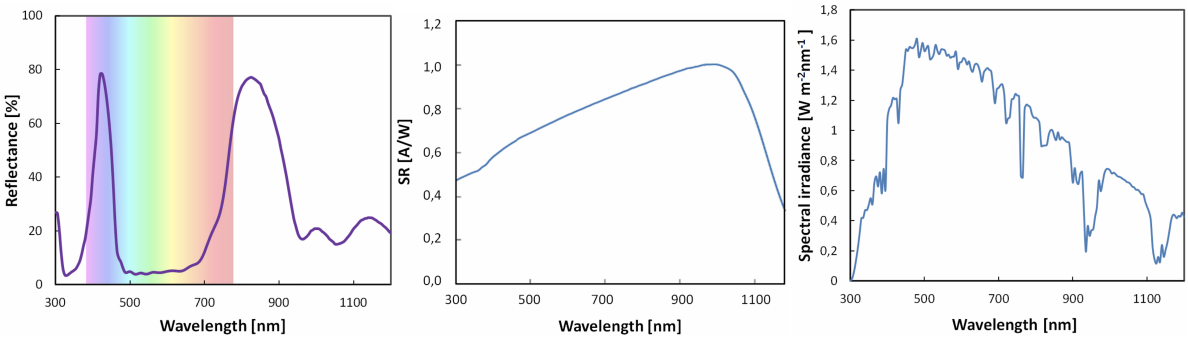

Figure 6.4: **(a)** *Text Purple* reflectance spectrum. **(b)** Spectral response (SR) of the used silicon cell. Adapted from [51]. **(c)** AM1,5 solar spectrum. Adapted from [70].

the *Randomly Text Purple* module in figure 6.5c it is clear that during the fabrication process one of the cells has been damaged. Producing a lower current, the broken cell will be thus limiting the whole module current output.

When it comes to the grooved textured glasses, the loss in terms of efficiency and generated power is much less severer than for the previous cases. With this type of glass, efficiencies of more than 15% are obtained. Among the three grooved mini-modules, the *Grooves Text Green* reports the best performance, with an efficiency drop of just 0,95% absolute with respect to the reference module. The main reason why it is the best performing module is the fact that its reflectance peak is quite low, due to both the smaller number of filter's layers (12 instead of 20) and the texturing of the glass which adds antireflective properties.

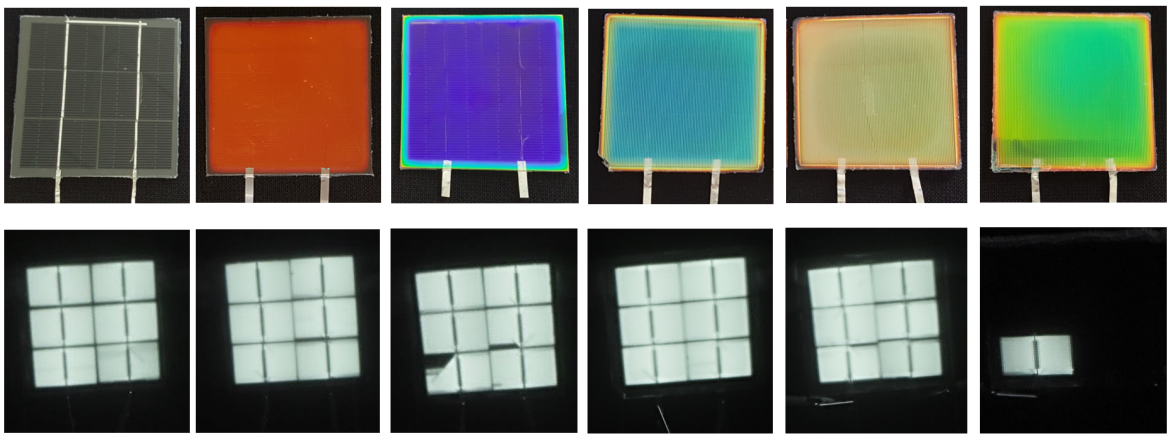

Figure 6.5: Electroluminescence photos (bottom row) corresponding to each colored mini-module (top row). In the order **(a)**-**(f)**: *Reference, Flat Orange, Random Text Purple, Grooves Text Green, Grooves Text Gold, Grooves Flat Green.*

The module with the filter on the flat side, *Grooves Flat Green*, has a slightly worst performance with respect to the other grooved glasses. As said before, the interference filter should only cause optical losses which result in lower current, but from its I-V curve in figure 6.2 it can be observed that this module presents also a voltage drop. The possible explanation for this is related to what we see in the EL image of 6.5f. When the EL photo was taken, only one of the six cells was contributing to the current generation. Likely, this is due to the fact that the first and last series-connected cells touched

each other overlapping (also visible at naked eye), thus making a preferential path for the current, which bypassed the remaining cells. The reason why we only see one of the two cells working is that probably the other one was shunted.

The overlapping between the cells happened because they were soldered too tight, and the thermal expansion, or simply a movement when placing the module in the laminator, caused the cells to touch each other. When this was found out, it was tried to mechanically separate them by pulling the external wires apart. To facilitate this process, the module was heated up to a temperature of around 60°C (thanks to the heat of the solar simulator) in order to make the EVA less solid and resistant. The attempt was successful and once the cells were not anymore in contact with each other, the I-V curve showed in the picture was taken. It can be seen that at that moment all the six cells were working and contributing to the current and voltage generation, but the damages caused by the above-mentioned reasons and the high temperature of the cell at the moment of the measurement might explain the voltage drop. The module showed an efficiency of 13.45%, but it is believed that in normal condition and without the mentioned complications, the module would have produced an I-V curve similar to those of the other grooved glasses, with efficiency higher than 15%.

6.2.2. Simulated EQE and J_{ph}

To have a more clear idea of how the optical losses generated by the interference filters affect the photogenerated current, the EQE (External Quantum Efficiency) can be analyzed. Unfortunately, it was not possible to measure the EQE of the fabricated mini-modules, hence only simulation results can be presented. The EQE is defined as the fraction of the photons incident on the solar cell that create electron-hole pairs which are successfully collected [23]. If no electrical losses are taken into account, the EQE(λ) of the device can be considered equal to the absorptance $A(\lambda)$ of the c-Si layer. Figure 6.6 shows the results of the simulations. In each plot three EQE curves are shown: the one of the mini-module (colored curve), the one of the reference module (black curve) and one obtained inputting in the model the real measured reflectance spectra of each respective mini-module. It must be stressed that the gray curve does not represent the real measured EQE, but a simulated curve that is surely closer to reality than the modelled colored curves (which are obtained using the original filter designs).

It can be observed how, in each plot, the EQE curves peak down in correspondence with the interference filter reflection. Additionally, it can be noticed that at wavelengths lower than 350 nm almost no electron-hole pairs are collected due to the absorption in the EVA layer between the top glass and the solar cell. Therefore, the fact that the SiN_x used for the filter fabrication is slightly absorbing in that range (up to 350 nm), as shown in figure 3.13, is not adding extra losses and is not detrimental for the module performance.

Even though a comparison between measured and simulated EQE could not be made, due to the impossibility of performing EQE measurements, the optical model could be validated by comparing the implied photogenerated current (GenPro4 output) to the measured short-circuit current. It should be noticed that this is an approximation, since the two quantities are equal only in the ideal case, e.g. no electrical losses due to recombination or uniform generation.

GenPro4 calculates the photocurrent based on how the filter and the module structure are designed. However, by now it is known that the original filter designs provide reflectance/EQE spectra which differ quite significantly (especially for the grooved glasses) from the measured ones. To take into account the error between these simulated and real curves, the J_{ph} simulations were corrected with a scaling factor $k = \frac{EQE_{meas}}{EQE_{sim}}$, where EQE_{sim} and EQE_{meas} are respectively the areas under the colored and grey curves of the plots of figure 6.6.

Figure 6.7 shows the measured, simulated and corrected values of J_{ph} for each mini-module. It can be noticed that when simulating the solar module without filter (*Reference*), the value of current (≈39,8 mA/cm^2) coincides with the measured one, although we would expect an overestimation

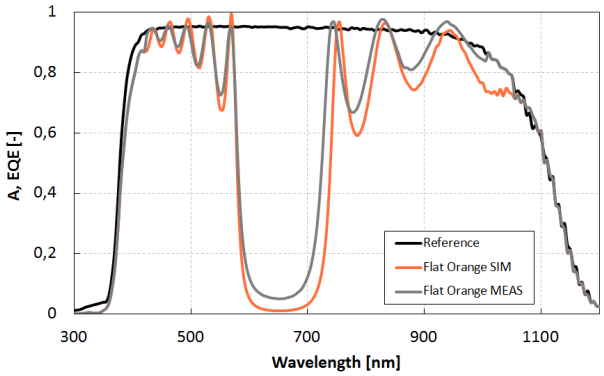

(a) Flat Orange.

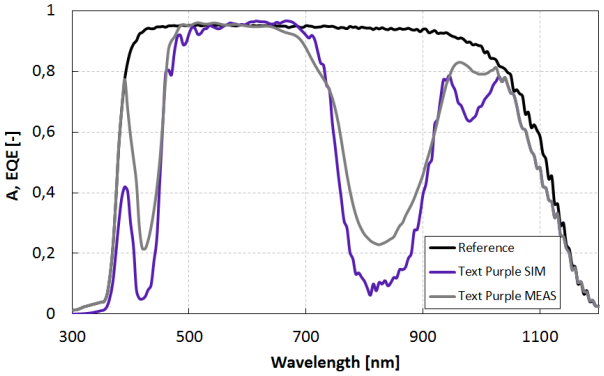

(b) Random Text Purple.

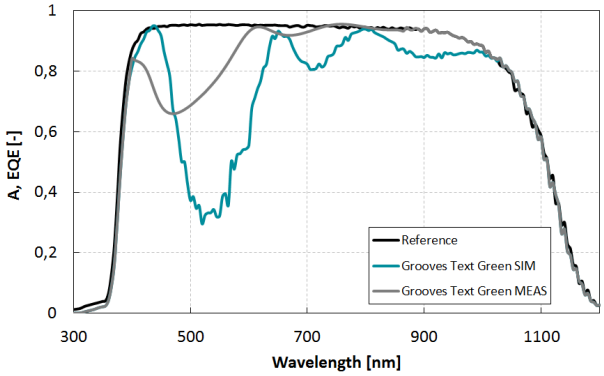

(c) Grooves Text Green.

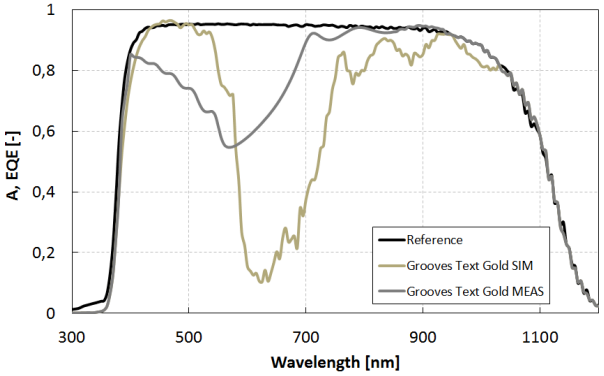

(d) Grooves Text Gold.

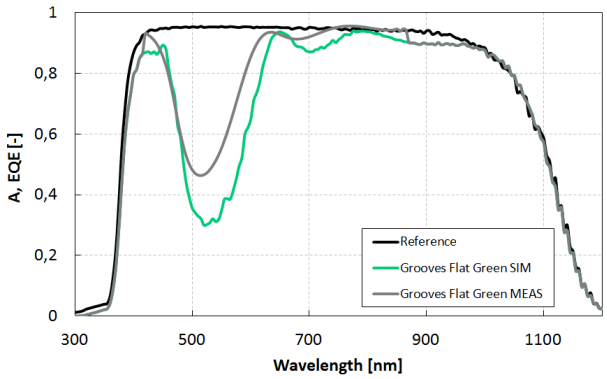

(e) Grooves Flat Green.

Figure 6.6: Simulated EQE of the five mini-modules (colored curves) compared to the reference one (black curves). The gray curves are obtained using in the model the real measured reflectance spectra.

due to the fact that electrical losses are not considered in the model. When the colored filters are considered, the model further underestimates the generated current (apart from the *Text Purple* module, which has a lower measured current due to the cell breakage). It can be noticed that the corrected simulations provide current values that are significantly closer to the measured ones, but an underestimation ranging from 0,5 to 1,1 mA/cm^2 (1,4% to 3,4%) is still present.

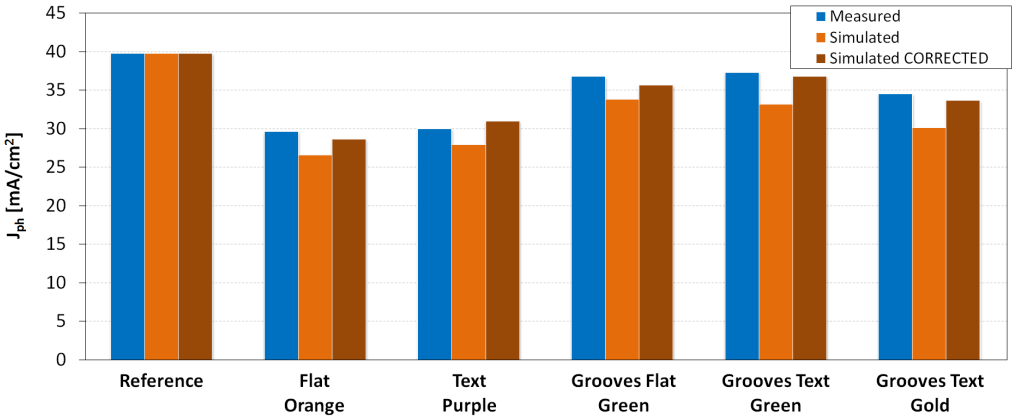

Figure 6.7: Comparison between measured and simulated photogenerated current ($J_{ph} \approx J_{sc}$). Simulation results are shown both with and without correcting for the reflectance spectra.

6.3. Cell-to-module (CTM) losses

The processing of solar cells into modules leads to several different physical power loss and gain mechanisms. The losses can be generically categorized as optical, electrical and geometrical. Optical losses mainly result from reflection and absorption in the glass and encapsulant, electrical losses are Ohmic losses due to the interconnections or related to cell mismatch, while geometrical losses are linked to the inactive areas between cells and at the margins. On the other hand, gains can be obtained through light in-coupling due to reflection coming from cell metallization, tabs, back cover, or from the reduced reflection at the cell/encapsulant interface (refractive index matching) [71],[72]. These losses are schematically shown and summarized in figure 6.8.

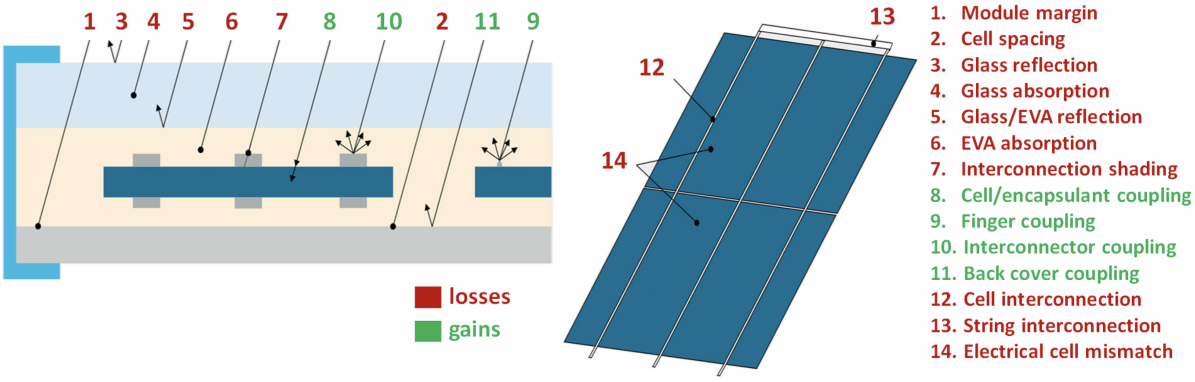

Figure 6.8: Schematic representation of loss and gain mechanisms in the module stack. Adapted from [71].

Some of these mechanisms are easy to identify and quantify, such as the losses due to the inactive areas of the module, but most of them are not directly measurable and can be only modelled. The approach used in this work to calculate the CTM losses is mainly experimental: the cell and module characteristics have been measured at each phase of the fabrication process, allowing to quantify the performance loss related to each step (cutting, soldering and lamination). The PV module manufacturing steps are summarized in figure 6.9; cell's electrical parameters have been measured before and after cutting, while module's parameters have been recorded after soldering and after lamination. Unfortunately, both solar simulators were unsuitable for measuring the full size Al-BSF solar cell at its initial state (before cutting): the area illuminated by Wacom is smaller than the size of the cell (15,675 x 15,675 cm^2), and the LASS cannot register too low current values.

Therefore, the initial cell's parameters have been retrieved from the datasheet. At any other stage, I-V curves and electrical features have been measured with Wacom.

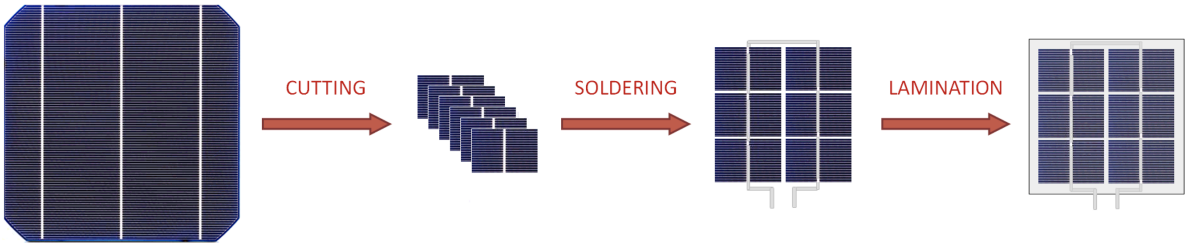

Figure 6.9: PV module fabrication steps at which CTM losses are associated.

For this CTM analysis, the reference module without filter has been used, in order to take into account only the losses caused by the conventional fabrication processes. The extra optical losses caused by the colored filters have been quantified in the previous section and can simply be added to this analysis.

Figure 6.10 shows the I-V curves traced at every stage of the module manufacture process: before cutting, after cutting, after soldering and after lamination. The theoretical ideal I-V curve of the 6-cell mini-module (no losses) has been also modelled and plotted in the graph (dotted line) as a term of comparison. The curve corresponding to the initial state, i.e. before cutting, is not the result of a measurement, but it has been reconstructed from the cell datasheet. In can be observed that, due to the significant area reduction, the I_{sc} drops from around 9,6 A before cutting to approximately 0,5 A after cutting. Therefore, the vertical axes has been cut in order to adjust the scale and make the plots more clearly visible.

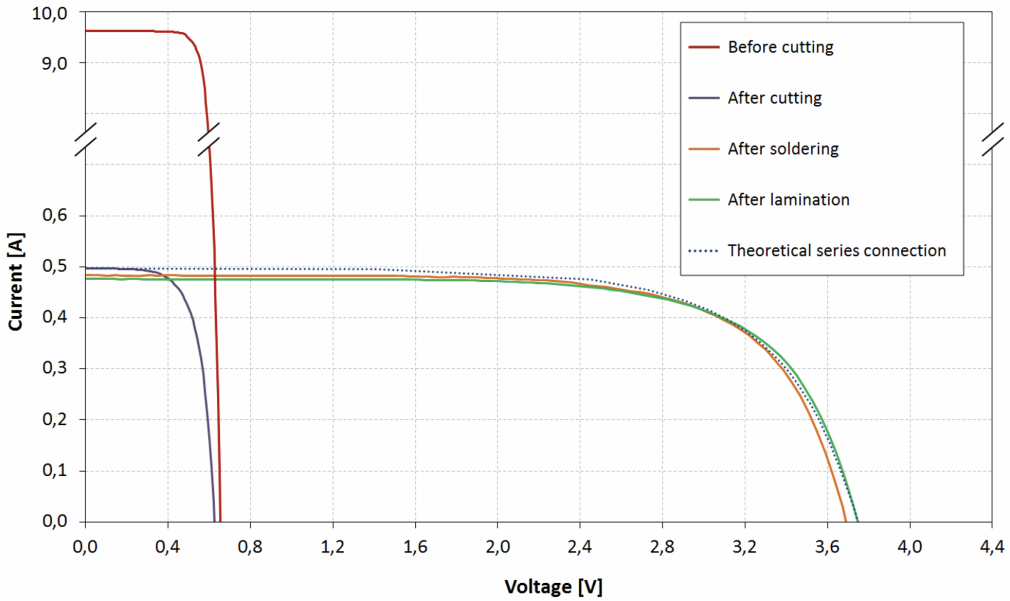

Figure 6.10: Comparison between I-V curves at every stage of the cell-to-module fabrication process.

The results of the measurements in terms of V_{oc}, I_{sc}, P_{mpp}, FF and η are reported in table 6.2. When in a solar module the cells are connected in series, as in our case, the voltage is given by the sum of the single cell's voltage, while the current is limited by the cell producing the lowest value [23]. Therefore, to make a fair analysis between before- and after-soldering steps, we compared the

module's parameters respectively to the sum of V_{oc} and P_{mpp} of the single cells, the minimum I_{sc} and the average FF and η.

Table 6.2: CTM losses: electrical parameters at every stage of the fabrication process.

Cell's parameter	**Cell (before cutting)**	**Cell (after cutting)**	Module's parameter	**Module (after soldering)**	**Module (after lamination)**
ΣV_{oc} [V]	3,930	3,750	V_{oc} [V]	3,692	3,746
Min.I_{sc} [A]	9,620	0,497	I_{sc} [A]	0,483	0,476
ΣP_{mpp} [W]	29,880	1,260	P_{mpp} [W]	1,245	1,244
Ave.FF [%]	78,88	67,61	FF [%]	69,76	69,75
Ave.η [%]	20,50	15,82	η [%]	15,63	15,62

Abbreviations used: Σ - sum of the six cells; Min - minimum value between the six cells; Ave - average value between the six cells.

The CTM losses associated to each production step can be also visualized in the waterfall charts of figure 6.11, in terms of both efficiency and fill factor. Some general conclusions can be drawn from the analysis. First of all, it can be seen that the major loss is obtained during the cutting process, with an efficiency and fill factor drop of almost 4,7% and around 11,3% absolute, respectively. On the other hand, the soldering and lamination processes do not affect strongly the results. After soldering, a FF increase or around 2% is reported. Eventually, the laminated module presents an efficiency of 15,62% and a fill factor of 69,75%, with respect to the initial values of 20,50% and 78,88%, respectively. In relative terms, the obtained efficiency loss is around 24%, which, compared to the typical CMT losses obtained in the market of around 12-15% relative [73], is a rather high value.

However, it should be remarked that there might be several uncertainties in these results, such as the determination of the exact area of the cut cells or the fact that the full-size cell could not be measured and we had to rely only on the datasheet specifications. Additionally, we are dealing with such small quantities that the losses values obtained sometimes fall within the error precision of the measurement machines. Bigger module configurations would be needed for more reliable CTM analysis.

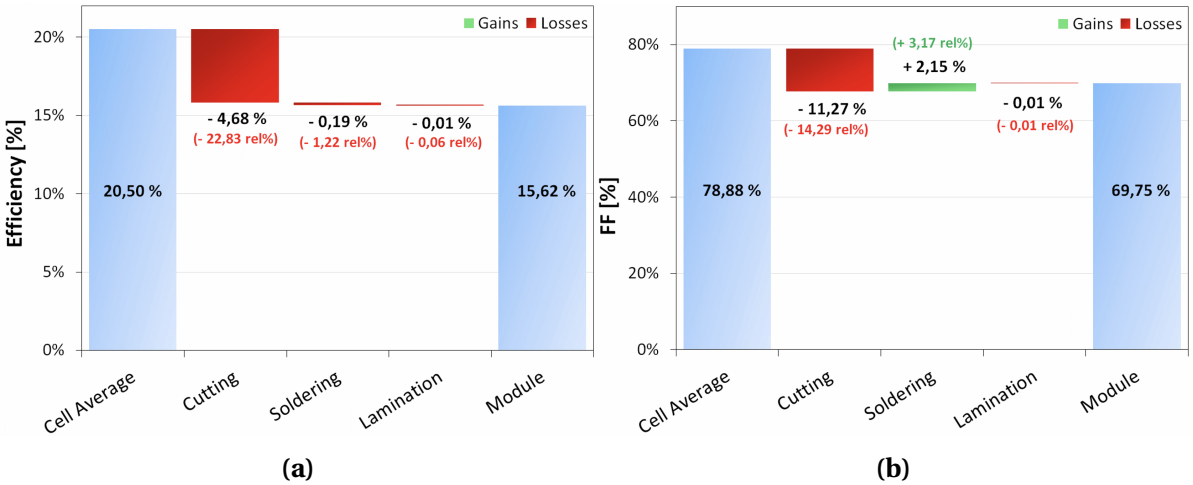

Figure 6.11: Waterfall charts expressing the CTM losses in terms of efficiency **(a)** and fill factor **(b)**.

Cutting process

Since the cutting process has proven to have the strongest negative impact on the CTM losses, it is worth to investigate which could be the reason. During a laser cutting process, electrical losses can occur. These are attributed to two main factors: additional shunts due to a reduction in the parallel resistance and increased carrier surface recombination due to the new cut edges [74]. Recombination losses are reflected as a change in the second saturation current density (J_{02}), which is the contribution of the recombination in the two-diode model [23]. On the other hand, shunt losses are caused by an increase in the leakage currents and can be detected in a qualitative way by comparing the slope of the J-V curves of the cell before and after cutting. Figure 6.12a shows that a reduced R_p (parallel/shunt resistance) causes the J-V curve to bend towards the origin, thus strongly affecting the fill factor. Comparing the measured J-V characteristic of one the six cut cells with the J-V curve of the original full-size cell (taken from the datasheet), shown in figure 6.12b, the slope deviation can be clearly detected. The curve, however, seems to be deviated also near the V_{oc} point, indicating that an high series resistance might be also present. Additionally, the graph shows a strong decrease in both V_{oc} and J_{sc} values, which contributes even further to reduce the overall module efficiency.

The reasons contributing to these high losses might be several. In literature, it has been proven that aspects such as choosing the right laser pulse length or the side at which the cut is performed (top or rear side of the cell), can significantly affect the performance of the cut and the related losses [75]. To fully understand the losses linked to the cutting step and eventually reduce them, further experimental analysis should be conducted and the laser cutting process should be optimized. This was out of the scope of the present thesis, but it is recommended for future work.

Apart from increasing the chances of having inherent defects and risking of damaging the cells, using cut solar cells can also have several advantages. If the cutting process is assumed to be optimized, using cut (e.g. smaller) cells might actually reduce the CTM losses because of the reduced amount of current flowing through the cell. In fact, the current strongly influences the electrical power losses, which are proportional to $R \cdot I^2$ (where R is the resistance and I the current); for instance, using half-cells would reduce the power losses by a factor of four.

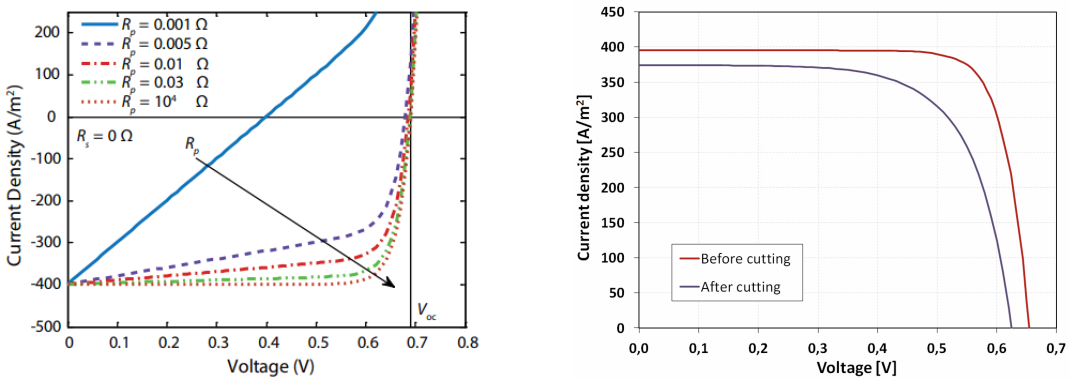

(a) **(b)**

Figure 6.12: **(a)** Effect of shunt resistance R_p on the J-V characteristic of a solar cell. Adapted from [23]. **(b)** J-V curves before (datasheet) and after cutting (measured).

6.4. Conclusion

The focus of this chapter has been the electrical performance assessment of the colored PV modules. At first, the experimental tools were described, namely the solar simulators for tracing the I-V characteristics of the modules and the electroluminescence setup used for detecting potential defects and fabrication problems. Secondly, the electrical performance of the colored mini-modules

was evaluated. The analysis was differentiated between measurement and simulation results. Both experimental and modelling results showed that the losses associated to the colored interference filter are almost exclusively optical. The measured I-V curve of each colored module has been compared with respect to the reference one. Efficiency losses ranging from just 0,95% to around 4,6% were obtained. The best performing module was found to be the *Grooved Text Green*, with an efficiency of 15,28%, while the worst one was the *Flat Orange* one, with an efficiency of 11,59%. The EL images showed that the electrical output of the modules was also affected by the status of the solar cells. Some issues arose during the fabrication process and some modules were found to be slightly damaged. In general, it can be concluded that texturing the external surface of the glass is helpful not only for increasing the color angular stability, but also for better electrical performance.

The EQE and J_{ph} simulations confirmed that the reduced generated current of the colored module with respect to the reference one is proportional to the peak of reflection generated by the interference filter. To validate the optical model, the measured J_{sc} was compared to the simulated J_{ph}. Although we were expecting the model to overestimate the generated current (since electrical losses are not reconsidered in GenPro4), we found the opposite behaviour: the simulations overestimated the current values, but with acceptable errors ranging from 1,4 to 3,4%.

Lastly, the cell-to-module losses were evaluated. During the processing of solar cells into modules several loss and gain mechanisms can take place. The CTM losses analysis performed on the reference module (without colored filter) showed an efficiency loss of around 24%rel (corresponding to almost 5%abs). The parameter that was most strongly affected was the fill factor, which dropped of around 11%rel net throughout the whole fabrication process. While the impact of soldering and lamination steps in the CTM losses was barely noticeable, it was found that laser cutting strongly affected the module fabrication process, producing the highest loss. The losses associated to cutting are mainly due to additional shunts and increased carrier surface recombination due to the new cut edges. It is extremely important to optimize the laser cutting process in order to significantly reduce these electrical losses, hence improving the performance of CTM process. However, it must be pointed out that our CTM analysis results might be affected by several uncertainties, for example due to the fact that we are dealing with so small quantities that the losses obtained sometimes fall within the error precision of the measurement machines. Absolute values should be considered with care, but the drawn general conclusions remain valid.

7

Conclusions and Recommendations

The lack of aesthetic flexibility, especially in terms of color options, is one of the main factors that hinder the implementation of BIPV systems in urban areas. In view of this, the objective of this thesis was to investigate the use of interference filters as color coatings for crystalline silicon PV modules. The investigation has been performed by modelling, fabricating and assessing the opto-electrical performance of colored mini-module demonstrators.

The work has been addressed following three main research topics, which have been identified by the three research questions introduced in chapter 1 and discussed throughout the report. The following sections present a summary of the most important results, divided by topic, and final recommendations for future work.

7.1. Angular resilience

The first research question that has been tackled states as follow:

How can the angular resilience of interference filters be improved?

Interference filters are optical devices that, thanks to selective reflection of light, are able to provide a structural coloration. However, their color is strongly dependent on the angle of incidence (AOI) of the light source. For flat surfaces, the so-called *blue-shift* takes place: with increasing AOI the reflection peak shifts towards lower wavelength values, thus changing the color perception of the filter. This phenomenon is due to the longer distance that light beams have to travel, which causes a change in the wavelength at which the reflected rays interfere constructively.

This issue was addressed from a modelling perspective, by using a ray-tracing software and a color perception algorithm, that allowed to simulate different filter structures at different illuminating conditions. The first important result revealed that the surface morphology of the filter (and its substrate) strongly influences its color appearance. Therefore, the study turned into a surface optimization problem with the goal of finding the best texturing profile. The ideal surface should be able to scatter light and generate an angular distribution profile of the reflected light as much as possible independent of the illuminating angle.

It emerged that the hemispherical shape is the best texturing profile, as long as the size of the texture features is sufficiently above the wavelength of light (in order to avoid interference). Additionally, it was proven that periodic 1D structures outperformed random and/or 2D configurations. Therefore, a profile with inverted hemispherical grooves (with height of around 3 μm) was found to be the best option. This geometry was applied first only on the external side of the glass (*text-flat* configuration) and then also on the filter side (to form a *concave lens*-like structure). Although more complex, texturing both sides of the glass helped in increasing even further the angular resilience.

By using the CIE ΔE_{2000} color-difference formula, it was possible to quantify the difference in

color when increasing the angle of incidence. The ΔE metric ranges from 0 to 100, where values below 10 are barely distinguishable by the human eye. For a flat glass, ΔE values up to 60 are obtained, while with the optimized hemispherical grooved glass this value is effectively reduced.

However, when simulating a full PV module stack with the *text-flat* filter configuration (filter on the internal flat side of the glass), the angular resilience did not improve significantly, and the ΔE almost reached 45 in the worst case of a green color. This was due to the fact that at high AOI the filter became transparent and the blue color of the solar cell placed underneath become visible, contrasting with the desired filter color. On the other hand, when simulating the *concave lens* configuration, the ΔE was significantly reduced to 10 until 40° and to around 20 at 80°.
These simulation results prove that a glass textured on both sides with hemispherical grooves can be used to produce colored PV modules with very high angular resilience. However, with this glass morphology, the good angular stability comes at the expenses of reduced brightness and more limited range of available colors.

7.2. Fabrication and optical characterization

In the second part of the work, the following research questions were addressed:

Is it possible to fabricate colored mini-modules based on interference filters? If so, does the optical behaviour of the colored demonstrators validate the optical model?

In chapter 5, it was shown that the answer to the first of these questions is positive: colored PV modules made with interference filters can be successfully manufactured. The fabricated mini-modules were made of 6 small cut Al-BSF solar cells connected in series and encapsulated in 10 x 10 cm^2 glasses on both front and rear side, with EVA as encapsulating material. The fabrication line consisted of three main steps: cutting, soldering and lamination. Additionally, a PECVD process was performed on glass substrates to deposit the colored filters. The designed filters were made of 20 or 12 layers of alternating SiN_X and SiO_2. In total, 5 colored mini-modules were fabricated. They differ from one another not only for the color, related to the different thicknesses and number of layers, but also for the type of glass used. In fact, three different types of glass were investigated: a flat, a randomly textured and a hemispherical grooved glass (with feature height of 500 μm). The 5 mini-modules have been identified as: *Flat Orange*, *Random Text Purple*, *Grooves Flat Green*, *Grooves Text Green* and *Grooves Text Gold*.

The optical characterization was performed via spectrophotometry. At first, the samples were analyzed at normal incidence in order to validate the optical model. It was found that when the filters were deposited on the flat glass or on the flat side of the grooved glass, a good agreement between measurements and simulations was obtained. On the other hand, when the filter was deposited on textured surfaces, especially on the large features of the grooved glass, the model was not able to simulate the real fabricated structure. One of the reasons might be that GenPro4, the ray-tracing software used, cannot reproduce textured periodic structures in an optimal way. Another explanation is given by the probable non-uniformity of the PECVD layer growth on the features of the highly textured glass. Likely, SiN_X and SiO_2 layers developed a thickness gradient along the feature shape, making it hard, if not impossible, to reproduce such structure with GenPro4. The optical model, therefore, could not be validated in this case.

When the angular optical behaviour was analyzed, it was found that the most angular resilient glass was the randomly textured one. Good color consistency was achieved also with the grooved glass. As expected, the flat glass module showed very strong angular dependence, due to the fact that its surface reflects only specularly. On the other hand, it was proven that for the randomly textured glass the blue-shift phenomenon is significantly reduced thanks to the diffusive nature of its textured surface. For the grooved glass the optical behaviour seemed to resemble that of a flat surface, since it presented directional reflectance, but only at specific angles. This peculiar behaviour might be due to the extremely large size of the hemispherical grooves and the periodicity of the

structure. Again, for this type of surface it was not possible to validate the optical model and provide a full explanation of the optical behaviour. It must be observed that the grooved glass used for the module fabrication cannot be directly compared to the ideal grooved glass presented in the angular resilience study, due to the extremely bigger size of the hemispherical features (500 μm vs. 3 μm).

All in all, it can be concluded that colored mini-modules could be successfully fabricated and that the optical model has been validated with acceptable error margins only for flat configurations and small-feature texturing surfaces (in the order of few microns).

7.3. Electrical performance

Improving the PV module aesthetics by using colored interference filters comes at the expenses of a reduced power output. To understand the amount of the electrical loss, the third research question was faced:

What is the electrical performance of the colored mini-modules made with interference filters?

The first important result that the electrical performance analysis showed is that the losses associated to the colored filter are almost exclusively optical, i.e. they are mainly reflected in a short-circuit current decrease. The five colored mini-modules presented efficiency losses ranging from just 0,95% to around 4,6%. The best performing module was found to be the *Grooved Text Green*, with an efficiency of 15,28%, while the worst one was the *Flat Orange* one, with an efficiency of 11,59%. Electroluminescence images showed that the electrical output of the modules was also affected by the status of the solar cells. Some issues arose during the fabrication process and some modules were found to be slightly damaged. However, it can be generally concluded that texturing the external surface of the glass is helpful not only for increasing the color angular stability, but also for better electrical performance. In fact, the anti-reflective nature of the textured surface lowers the peak of reflection generated by the filter, thus transmitting more light to the cell.

The short-circuit current density of the mini-modules was also simulated with GenPro4. When the results were corrected using the real measured reflectance spectra, it was found that the model overestimated the measurement results, but with acceptable errors ranging from 1,4% to 3,4%.

Lastly, the cell-to-module (CTM) losses related to our in-house PV modules manufacture process were evaluated. During the processing of solar cells into modules several loss and gain mechanisms can take place. The CTM analysis performed on the reference module (without colored filter) showed an efficiency loss of around 24% relative, corresponding to a drop of almost 5% absolute. The parameter that was most strongly affected was the fill factor, which dropped of around 11% relative net throughout the fabrication process. While the impact of both soldering and lamination steps was barely noticeable, it was found that laser cutting strongly affected the module fabrication process, contributing to a great extent to the overall loss.

7.4. Recommendations

In this work, interference filters have proven to be a promising solution to increase the color flexibility of PV modules with low impact on performance. However, to fully understand their advantages and limitations more research should be conducted.

The optical model showed that the angular resilience problem can be tackled by depositing the filter on a textured glass. In particular, the hemispherical shape was found to be the optimal geometry for the texture features. Unfortunately, due to time limitation, it was not possible to manufacture the modelled hemispherical grooved glass. The glass sample that was used in this work was similar to the ideal one with respect to the shape (hemispherical grooves), but different in size (hemispheres height around 100 times higher). The optical measurements showed that most likely the filter deposition resulted in highly non-homogeneous layers, with thickness gradient along the texture fea-

tures. Because of this, it was not possible to make a fair comparison between our optical model (that simulates consistent and uniform layers) and the real filter. In view of this, it would be recommended to manufacture the modelled hemispherical grooved glass, with the goal of validating the model. It is believed that with features of few μm, also the PECVD deposition would result in more uniform layers. It is also advised to further investigate the suitability of GenPro4 as ray-tracing software for modelling textured periodical surfaces. Additionally, the angular optical characterization of the colored textured mini-modules could be improved. The ARTA machine provided results in terms of angular intensity distribution (AID), which could not be directly compared the reflectance values, output of the optical model.

An aspect that was only touched, but needs further investigation, is the differentiation between *angle of incidence* of the light source and *angle of observation*. In the optical model we assumed the angle of incidence to change, since in reality the sun position will change during the day and the seasons. But, of course, the perceived color of an object depends also from the observer. For instance, it would be interesting to understand how the color of a potential PV facade made with IF would change when we walk on the street, i.e. when we change our observation point. If the filter is deposited on flat surfaces, specular reflection is achieved and light source and observer can be interchanged without changing the perception of the color. But textured surfaces scatter light depending on the geometry and the size of feature, therefore, their optical behaviour should be further investigated.

Moreover, in reality a PV panel will receive light from all directions due to the diffuse and albedo components of the total irradiance. In this respect, it would be interesting to build a setup that reproduces conditions of diffuse light, in order to test the IF filter under different illuminating conditions.

Regarding the production line of the mini-modules, it would be recommended to further optimize the cutting and lamination process. In particular, it is believed that the high losses due to the cutting step, emerged in the CTM study, can be significantly reduced if the laser cutter parameters are optimized for the specific cell type used. Regardless, it is advised to perform new CTM losses analysis with bigger cells and module configurations, in order to obtain more reliable measurement, with current and power outputs sufficiently above the errors of the measurement tools.

Bibliography

[1] SUPSI-SEAC. Building integrated photovoltaics: Product overview for solar building skins, status report 2017. http://www.bipv.ch/images/Report%202017_SUPSI_SEAC_BIPV.pdf, 2017.

[2] A Jäger-Waldau. Pv status report. 2017, 2017.

[3] Floor JW Osseweijer, Linda BP Van Den Hurk, Erik JHM Teunissen, and Wilfried GJHM van Sark. A comparative review of building integrated photovoltaics ecosystems in selected european countries. *Renewable and Sustainable Energy Reviews*, **90**:1027–1040, 2018.

[4] Thomas Herzog, A Goetzberger, and J Luther. *European Charter for Solar Energy in Architecture and Urban Planning*. Prestel, USA, 2008.

[5] Werner Weiß. Solar combisystems for a sustainable energy future, 2001.

[6] Ali Nik Eteghad and Ezequiel Uson Guardiola. Energy efficiency in Thomas Herzog's architecture: From interdisciplinary research to performance form. *3rd Annual International Conference on Architecture and Civil Engineering*, , 2015.

[7] Metal Architecture. Improving photovoltaics' aesthetics. https://www.metalarchitecture.com/articles/improving-photovoltaics-aesthetics, 2013. Accessed: 5-11-2018.

[8] TMD STUDIO LTD. The perception of color in architecture. https://medium.com/studiotmd/the-perception-of-color-in-architecture-cf360676776c, 2017. Accessed: 5-11-2018.

[9] H Angus Macleod and H Angus Macleod. *Thin-film optical filters*. CRC press, 2010.

[10] Cameron Stanley, Ahmad Mojiri, and Gary Rosengarten. Spectral light management for solar energy conversion systems. *Nanophotonics*, **5**(1):161–179, 2016.

[11] Minghua Li, Libin Zeng, Yifeng Chen, Lin Zhuang, Xuemeng Wang, and Hui Shen. Realization of colored multicrystalline silicon solar cells with sio2/sinx: H double layer antireflection coatings. *International Journal of Photoenergy*, **2013**, 2013.

[12] Yifeng Chen, Yang Yang, Zhiqiang Feng, Pietro P Altermatt, and Hui Shen. Color modulation of c-si solar cells without significant current-loss by means of a double-layer anti-reflective coating. 27th EUPVSEC, 2012.

[13] I. Tobias, A. El Moussaoni, and A. Luque. Colored solar cells with minimal current mismatch. *IEEE Transactions on Electron Devices*, **46**(9):1858–1865, 1999.

[14] G Peharz, B Grosschädl, C Prietl, W Waldhauser, and FP Wenzl. Tuning the colors of c-si solar cells by exploiting plasmonic effects. In *Next Generation Technologies for Solar Energy Conversion VII*, volume 9937, 99370P. International Society for Optics and Photonics, 2016.

[15] Kamaleon Solar. Colorblast brochure. https://kameleonsolar.com, 2018. Accessed: 14-06-2018.

[16] Benedikt Bläsi, Thomas Kroyer, Oliver Höhn, Martin Wiese, Claudio Ferrara, Ulrich Eitner, and Tilmann E Kuhn. Morpho butterfly inspired coloured bipv modules. In *33rd European PV Solar Energy Conference and Exhibition*, 2017.

[17] Rebecca E Coath. Investigating the use of replica morpho butterfly scales for colour displays. *Dimensions*, **5**(7), 2007.

[18] Kromatix™ by swissinso. `https://www.swissinso.com`. Accessed: 24-06-2018.

[19] Nicolas Jolissaint, Rafic Hanbali, Jean-Christophe Hadorn, and Andreas Schüler. Colored solar façades for buildings. *Energy Procedia*, **122**:175–180, 2017.

[20] J. Williams and K. Hagen. Ensuring place-responsive design for solar photovoltaics on buildings - a good practice guide for designers, manufacturers, and installers. Technical report, BRE and CPRE, 2016.

[21] Lof solar corporation. `http://www.lofsolar.com/`. Accessed: 25-06-2018.

[22] Issol, architecture - bipv. `http://www.issol.eu/solsmaragden-union-brygge-drammen/`. Accessed: 27-06-2018.

[23] A. H. M. Smets, K. Jäger, O. Isabella, R. A. C. M. M. Van Swaaij, and M. Zeman. *Solar energy: The physics and engineering of photovoltaic conversion, technologies and systems*. UIT, Cambridge, UK, 2016. ISBN 9781906860325.

[24] Igcse aid - dispersion of light. `https://igcseaid.wordpress.com/notes/coordinated-science-0654/p8-4-dispersion-of-light/`. Accessed: 10-07-2018.

[25] Arthur Schuster. *An introduction to the theory of optics*. E. Arnold, 1904.

[26] Edmund optics - introduction to polarization. `https://www.edmundoptics.com/resources/application-notes/optics/introduction-to-polarization/`. Accessed: 16-07-2018.

[27] Eugene Hecht. Optics, 4th. *International edition, Addison-Wesley, San Francisco*, **3**:2, 2002.

[28] Abrisa technologies - wavelength selection filters. `http://abrisatechnologies.com/products-services/coating-solutions/coatings-capabilities/wavelength-selection-filters/`. Accessed: 20-07-2018.

[29] Olindo Isabella. *Light management in thin-film silicon solar cells*. PhD thesis, Delft University of Technology, 2013.

[30] Juan Camilo Ortiz Lizcano. *Optic Filters for Built-integrated Photovoltaic (BIPV) applications*. Master's thesis, Delft University of Technology, 2014.

[31] B Karunagaran, SJ Chung, S Velumani, and E-K Suh. Effect of rapid thermal annealing on the properties of pecvd sinx thin films. *Materials Chemistry and Physics*, **106**(1):130–133, 2007.

[32] Rudi Santbergen. *Manual for solar cell optical simulation software: GENPRO4*, 2017.

[33] Rudi Santbergen, Tomomi Meguro, Takashi Suezaki, Gensuke Koizumi, Kenji Yamamoto, and Miro Zeman. Genpro4 optical model for solar cell simulation and its application to multijunction solar cells. *IEEE Journal of Photovoltaics*, **7**(3):919–926, 2017.

[34] Florida State University. Molecular expressions: Optical microscopy primer, physics of light and color. http://micro.magnet.fsu.edu/primer/lightandcolor/humanvisionintro.html, . [Online] Accessed: 15-08-2018.

[35] University College of London. Color vision research and laboratory. http://www.cvrl.org/, 2006. [Online] Accessed: 16-08-2018.

[36] Wikipedia. Luminous efficacy. https://en.wikipedia.org/wiki/Luminous_efficacy, . [Online] Accessed: 17-08-2018.

[37] Wikipedia. Color. https://en.wikipedia.org/wiki/Color, . [Online] Accessed: 15-08-2018.

[38] Justin Henrie, Spencer Kellis, Stephen M Schultz, and Aaron Hawkins. Electronic color charts for dielectric films on silicon. *Optics express*, **12**(7):1464–1469, 2004.

[39] Wikipedia. sggb. https://en.wikipedia.org/wiki/SRGB, . [Online] Accessed: 20-08-2018.

[40] Mohamed Amara, Fabien Mandorlo, Romain Couderc, Félix Gerenton, and Mustapha Lemiti. Temperature and color management of silicon solar cells for building integrated photovoltaic. *EPJ Photovoltaics*, **9**:1, 2018.

[41] Matthew P Lumb, Woojun Yoon, Christopher G Bailey, David Scheiman, Joseph G Tischler, and Robert J Walters. Modeling and analysis of high-performance, multicolored anti-reflection coatings for solar cells. *Optics Express*, **21**(104):A585–A594, 2013.

[42] Bruce Lindbloom. Rgb/xyz matrices. http://www.brucelindbloom.com/index.html?Eqn_RGB_XYZ_Matrix.html. [Online] Accessed: 20-08-2018.

[43] Zachary Schuessler. Delta e 101. http://zschuessler.github.io/DeltaE/learn/. [Online] Accessed: 31-08-2018.

[44] Gaurav Sharma, Wencheng Wu, and Edul N Dalal. The ciede2000 color-difference formula: Implementation notes, supplementary test data, and mathematical observations. *Color Research & Application: Endorsed by Inter-Society Color Council, The Colour Group (Great Britain), Canadian Society for Color, Color Science Association of Japan, Dutch Society for the Study of Color, The Swedish Colour Centre Foundation, Colour Society of Australia, Centre Français de la Couleur*, **30**(1):21–30, 2005.

[45] Gaurav Sharma. Color fundamentals for digital imaging. *Digital color imaging handbook*, **20**, 2003.

[46] JA Dobrowolski. Chapter 42: Optical properties of films and coatings. *Handbook of Optics*, **1**: 42–3.

[47] Mark S Rea et al. *The IESNA lighting handbook: reference & application*. Illuminating Engineering Society of North America New York, 2000.

[48] Mopa fiberlaser 30 watt kleur graveren “emma”. https://lasergraaf.nl/product/mopa-fiber-laser-30w-kleur-graveren/. Accessed: 22-10-2018.

[49] Liang Dong and Bryce Samson. *Fiber Lasers: Basics, Technology, and Applications*. CRC Press, 2016.

[50] Bryce Furlong and Sherie Motakef. Scanning lenses and systems. *Photonik international*, **2**: 20–23, 2008.

[51] ExcelTon. Datasheet 6“ mono-crystalline, 3bb, solar cell. http://www.e-tonsolar.com/upload/ExcelTon%20III%206S3BB.pdf.

[52] Weller. Datasheet weller ws 81 analog soldering station. file:///C:/Users/TEMP.DASTUD.052/Downloads/Datasheet__2site__424_en__23-10-2018.pdf.

[53] Harry Wirth. Crystalline silicon pv module technology. In *Semiconductors and Semimetals*, volume 89, 135–197. Elsevier, 2013.

[54] Experia. Lab laminators - laminator lam600. http://www.experia.solar/laboratory-laminator/lam-600/. Accessed: 22-10-2018.

[55] Oxford Instruments. Plasma enhanced chemical vapour deposition (pecvd). https://plasma.oxinst.com/campaigns/technology/pecvd,. Accessed: 22-10-2018.

[56] Oxford Instruments. Brochure plasmapro 80 range. https://plasma.oxinst.com/assets/uploads/documents/PlasmaPro_80_Brochure.pdf,.

[57] Perkin Elmer. Lambda 650/850/950 - hardware guide. https://cmdis.rpi.edu/sites/default/files/UVVis-PerkinElmer-Lambda950-HardwareGuide.pdf,.

[58] Perkin Elmer. Lambda 950 uv/vis spectrophotometer. http://www.perkinelmer.com/product/lambda-950-uv-vis-nir-spectrophotometer-l950,. Accessed: 22-10-2018.

[59] OMT Solution BV. Absolute reflectance/transmittance analyzer (arta). http://www.omtsolutions.com/products/absolute-reflectance-transmittance-analyzer-arta/. Accessed: 24-10-2018.

[60] Thomas Loef. *Periodic-Random Modulated Surface Textures For Efficient Light Trapping in Thin-Film Silicon Solar Cells*. Master's thesis, Delft University of Technology, 2018.

[61] Zachary Holman Zhengshan Yu, Mark O'Neill and Christopher Lynch. Full-spectrum, angle-resolved reflectance and transmittance of optical coatings using the lambda 950/1050 uv/vis/nir spectrophotometer with the arta accessory. https://www.perkinelmer.com/lab-solutions/resources/docs/TCH_Full-Spectrum-Angle-Resolved-Reflectance-and-Transmittance-of-Optical-Coating-LAMBDA-with-ARTA-012188_01.pdf, 2015. Accessed: 25-10-2018.

[62] Andrea Ingenito, Stefan L Luxembourg, Pierpaolo Spinelli, Ji Liu, Juan C Ortiz Lizcano, Arthur W Weeber, Olindo Isabella, and Miro Zeman. Optimized metal-free back reflectors for high-efficiency open rear c-si solar cells. *IEEE Journal of Photovoltaics*, **6**(1):34–40, 2016.

[63] Kristin Pfeiffer, Ulrike Schulz, Andreas Tünnermann, and Adriana Szeghalmi. Antireflection coatings for strongly curved glass lenses by atomic layer deposition. *Coatings*, **7**(8):118, 2017.

[64] K Pfeiffer, U Schulz, A Tünnermann, and A Szeghalmi. Ta 2 o 5/al 2 o 3/sio 2-antireflective coating for non-planar optical surfaces by atomic layer deposition. In *Advanced Fabrication Technologies for Micro/Nano Optics and Photonics X*, volume 10115, 1011513. International Society for Optics and Photonics, 2017.

[65] Carnegie Mellon University. Basic principles of surface reflectance - lecture slides. https://www.cs.cmu.edu/afs/cs/academic/class/15462-f09/www/lec/lec8.pdf,. Accessed: 29-10-2018.

[66] Eternal Sun. Performance testing aaa-class solar simulator. http://www.eternalsun.com/products/solar-simulator/. Accessed: 30-10-2018.

[67] Wacom. Super solar simulator (continuous type, two lamp system). http://www.wacom-ele.co.jp/en/products/solar/super/. Accessed: 2-11-2018.

[68] A Mansouri, M Zettl, O Mayer, M Lynass, M Bucher, and O Stern. Defect detection in photovoltaic modules using electroluminescence imaging. In *27th European Photovoltaic Solar Energy Conference and Exhibition*, 3374–3378, 2012.

[69] Takashi Fuyuki and Athapol Kitiyanan. Photographic diagnosis of crystalline silicon solar cells utilizing electroluminescence. *Applied Physics A*, **96**(1):189–196, 2009.

[70] PV Lighthouse. Spectrum library. https://www2.pvlighthouse.com.au/resources/optics/spectrum%20library/spectrum%20library.aspx. Accessed: 1-11-2018.

[71] Fraunhofer ISE. Smartcalc.ctm. https://www.cell-to-module.com/software/#features. Accessed: 2-11-2018.

[72] Hamed Hanifi, Charlotte Pfau, David Dassler, J Schneider, S Schindler, Marko Turek, and Joerg Bagdahn. Investigation of cell-to-module (ctm) ratios of pv modules by analysis of loss and gain mechanisms. *Photovoltaics Int*, **32**:89–99, 2016.

[73] Ingrid Haedrich, Martin Wiese, Benjamin Thaidigsman, Dirk Eberlein, Florian Clement, Ulrich Eitner, Ralf Preu, and Harry Wirth. Minimizing the optical cell-to-module losses for mwt-modules. *Energy Procedia*, **38**:355–361, 2013.

[74] Stefan Eiternick, Kai Kaufmann, Jens Schneider, and Marko Turek. Loss analysis for laser separated solar cells. *Energy Procedia*, **55**:326–330, 2014.

[75] Jens Müller, David Hinken, Susanne Blankemeyer, Heike Kohlenberg, Ulrike Sonntag, Karsten Bothe, Thorsten Dullweber, Marc Köntges, and Rolf Brendel. Resistive power loss analysis of pv modules made from halved 15.6× 15.6 cm 2 silicon perc solar cells with efficiencies up to 20.0%. *IEEE Journal of Photovoltaics*, **5**(1):189–194, 2015.